Project No. 09-832

Multiaxial Creep-Fatigue and Creep-Ratcheting Failures of Grade 91 and Haynes 230 Alloys Toward Addressing Design Issues of Gen IV Nuclear Power Plants

Reactor Concepts

Dr. Tasnim Hassan
North Carolina State University

In collaboration with:
Idaho National Laboratory
Pennsylvania State University

Sue Lesica, Federal POC
Richard Wright, Technical POC

NEUP Nuclear Energy University Programs
U.S. Department of Energy

NEUP Project ID#09-832: Year 5 – 4th Quarter & Final Report

Creep-Fatigue and Creep-Ratcheting Failures of Alloy 617: Experiments and Unified Constitutive Modeling towards Addressing the ASME Code Issues

Principal Investigators: Prof. T. Hassan, North Carolina State University
Prof. C.J. Lissenden, Penn State University
Dr. L. Carroll, Idaho National Lab

Students: Shahriar Quayyum (PhD), Nazrul Islam (PhD), Patrick Pritchard (MS), Matthew Fenton (MS) and Yu-Chin Chan (Undergrad), NC State University.
Mainak Sengupta (MS) and Gloria Choi (MS), Penn State University

Technical Point of Contact: Dr. R. Wright, Idaho National Lab
Federal Point of Contact: Dr. Susan Lesica, U.S. Department of Energy

Project Objectives:

The proposed research will develop systematic sets of uniaxial and multiaxial experimental data at a very high temperature (850-950^{o}C) for Alloy 617. The loading histories to be prescribed in the experiments will induce creep-fatigue and creep-ratcheting failure mechanisms. These experimental responses will be scrutinized in order to quantify the influences of temperature and creep on fatigue and ratcheting failures. A unified constitutive model (UCM) will be developed and validated against these experimental responses. The improved UCM will be incorporated into the widely used finite element commercial software packages ANSYS. The modified ANSYS will be validated so that it can be used for evaluating the very high temperature ASME-NH design-by-analysis methodology for Alloy 617 and thereby addressing the ASME-NH design code issues.

Year 5-4th Quarter and Final Report:

This report is stating the overall, as well as, the year 5-4th quarter accomplishments.

1. Experimental Task and Outcomes:

A total of 125 uniaxial and multiaxial fatigue, fatigue-creep, and ratcheting isothermal experiments for the temperature range 25-950 degree centigrade were conducted in this project. The acquired data were critically analyzed to understand the high temperature fatigue-creep-ratcheting responses of Alloy 617 and to develop an experimentally validated advanced unified constitutive model (UCM). Based on the Alloy 617 material experiment outcomes, three MS theses and seven conference papers have been published. Two journal paper manuscripts are developed (attached with this report) and will be submitted to archival journals for publications. Such a broad and systematically developed data set was not available in the past and hence will be extremely beneficial for developing ASME Design Code provisions for Alloy 617 and unified constitutive models. The data set will be extremely beneficial in designing very high temperature components, such as, intermediate heat exchanger components under thermo-mechanical fatigue loading.

2. Unified Constitutive Model Development Task and Outcomes:

A modified unified constitutive model (UCM) has been developed based on the Chaboche non-linear kinematic hardening model by incorporating advanced modeling features for simulating

uniaxial and multiaxial fatigue and ratcheting responses. Based on the knowledge learned from the experimental task, various advanced modeling features were included in the UCM. These modeling features included multiple strain range, static recovery, multiaxial ratcheting and nonpropotional cyclic hardening/softening for simulating Alloy 617 responses for a wide temperature range and loading rates. With the modified UCM it was possible to simulate the whole set of the uniaxial and multiaxial fatigue-ratcheting responses. Two PhD and one MS students dedicated their efforts in developing the robust UCM. In addition to several conference papers, one manuscript on improved UCM for uniaxial fatigue and fatigue-creep response simulations is already developed (attached with this report) for archival journal publications. The second manuscript on improved UCM for multiaxial fatigue and ratcheting response simulations is under development and will be completed by mid Nov of 2014. The recent ASME Pressure Vessels and Piping (PVP) Conference paper and results of the UCM multiaxial response simulation are presented below to demonstrate the progresses made over the last quarter. The robust UCM developed in this task was not available earlier and hence outcome of this task is a significant accomplishment of this project.

Simulation of multiaxial fatigue-ratcheting responses of Alloy 617 using the Advanced UCM:

It has been demonstrated earlier that the currently available UCM in the commercial finite element software packages cannot simulate multiaxial fatigue-ratcheting responses of Alloy 617 developed under the loading histories considered in this project (see Fig. 1). Hence, multiaxial ratcheting and nonproportional cyclic hardening-softening modeling features were incorporated into the UCM (see the recent ASME PVP conference attached with this report). With the modified UCM it was possible to simulate the whole set of the multiaxial fatigue-ratcheting responses as shown in Figs. 2-4, where it is observed that the stress-strain responses, cyclic hardening/softening of equivalent stress amplitude and axial strain ratcheting responses under different temperature levels, and shear strain amplitudes and rates are simulated with very good accuracy. The nonproportional cyclic hardening responses obtained under 90-degree out of phase (MOP) loading cycles and subsequent softening under axial strain cycle for different temperature levels, strain amplitudes and rates are also simulated well as shown in Fig. 5. Detailed of the modeling can be found in the recently published article in the ASME PVP conference proceeding (included with this report).

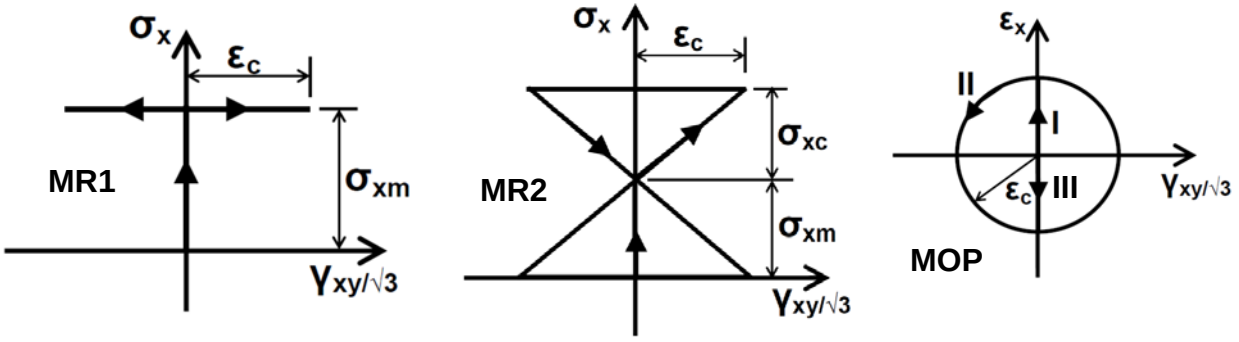

Fig. 1. Loading histories prescribed in the multiaxial experiments Alloy 617, (a) cyclic shear strain under steady tensile stress (MR1), (b) cyclic tensile stress and shear strain along a bow-tie path (MR2), and (c) axial and shear strain cycle along a circular path (MOP, Phase II), with uniaxial strain cycles before and after phase II (Phase I and III).

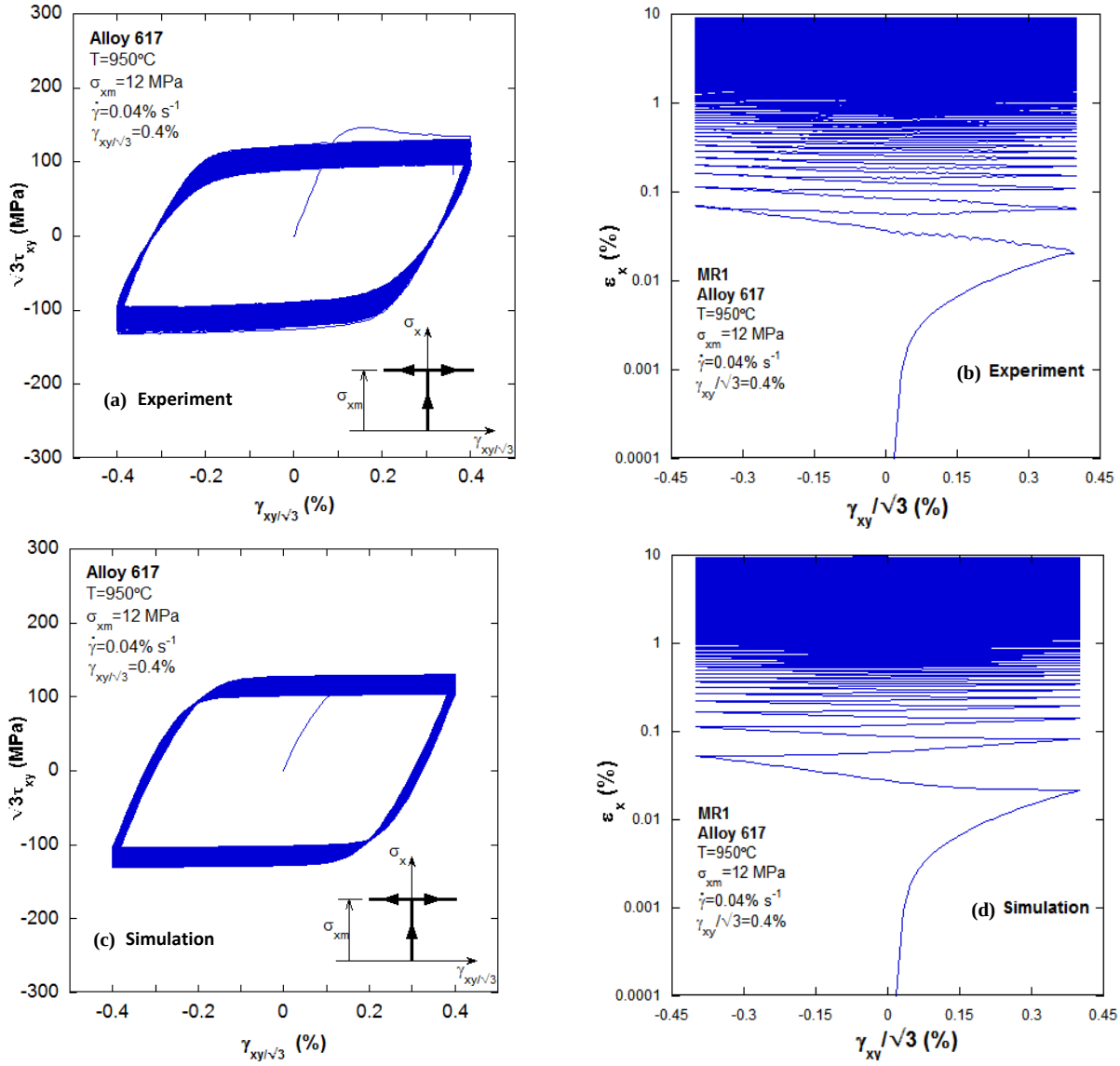

Fig. 2. Experimental and simulated stress-strain responses under MR1 multiaxial loading path at 950ºC, (a) shear stress-strain (equivalent) experimental response, (b) axial-shear strain (equivalent) experimental response, (c) shear stress-strain (equivalent) simulation response, (d) axial-shear strain (equivalent) simulation response.

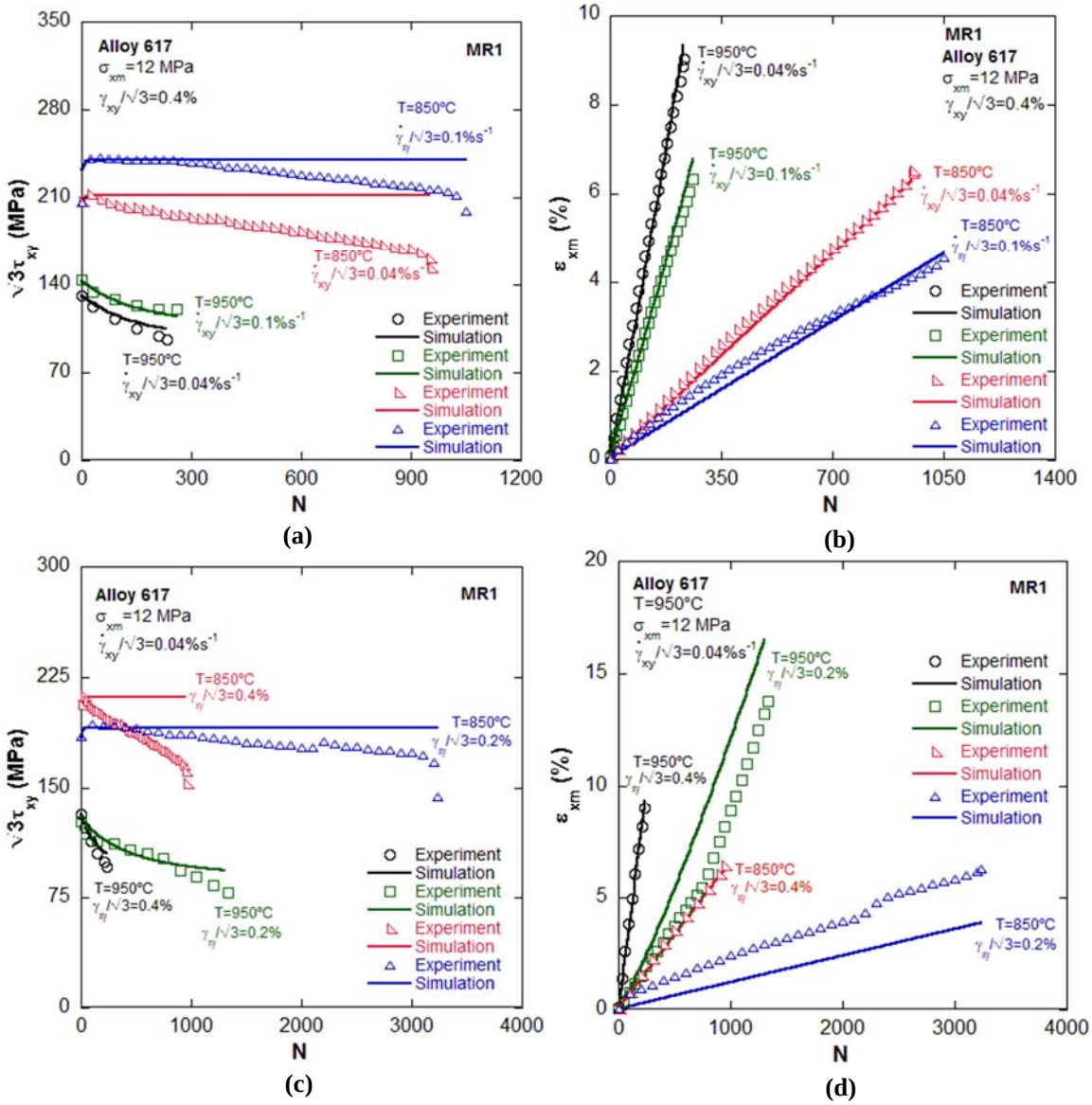

Fig. 3. Experimental and simulated responses for MR1 load path at different temperature and shear strain rate, (a) shear stress amplitude (equivalent), (b) axial strain ratcheting rate, (c) Shear stress amplitude (equivalent), (d) axial strain ratcheting rate.

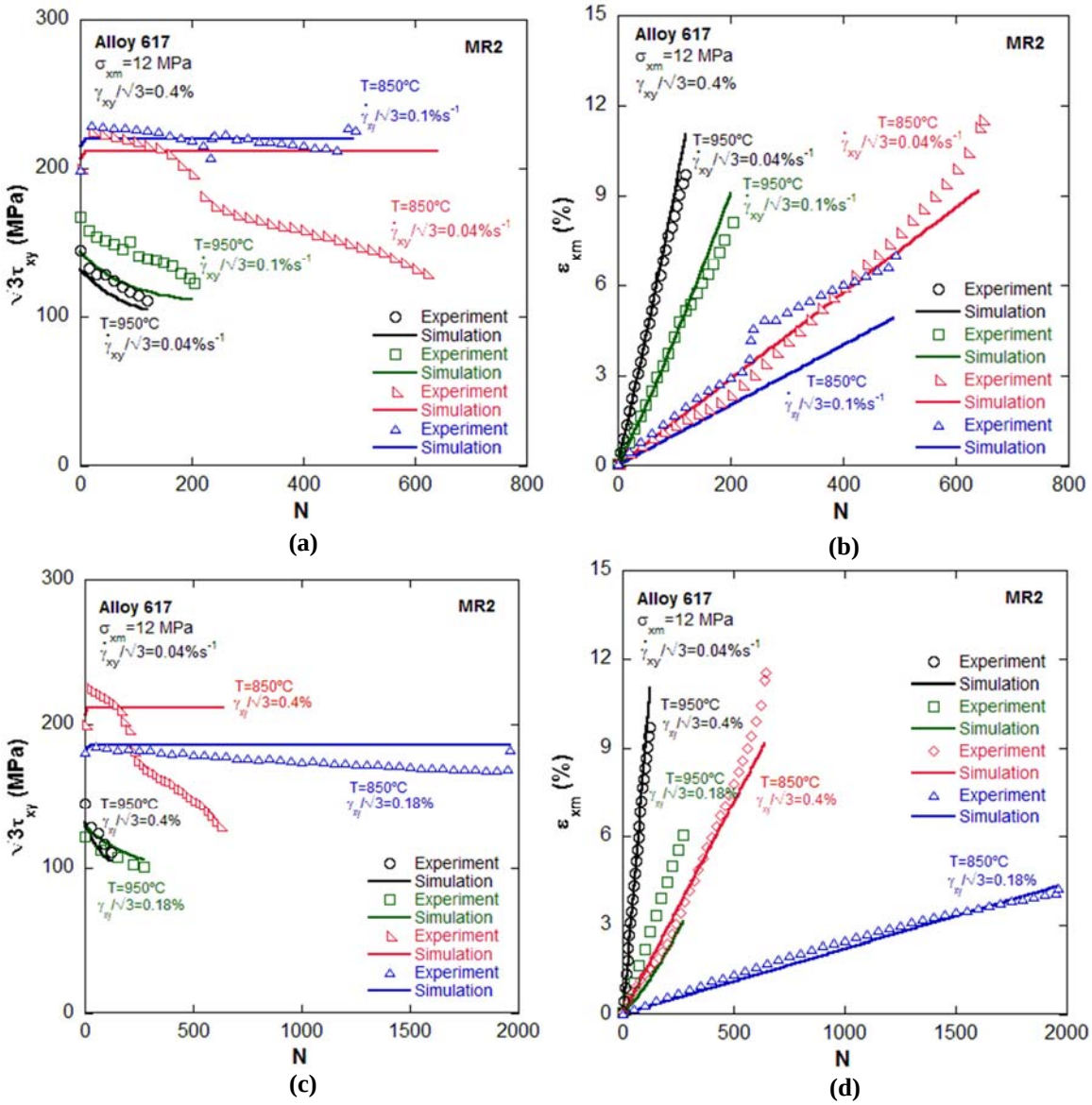

Fig. 4. Experimental and simulated responses for MR2 load path at different temperature and shear strain rate, (a) shear stress amplitude (equivalent), (b) axial strain ratcheting rate, (c) Shear stress amplitude (equivalent), (d) axial strain ratcheting rate.

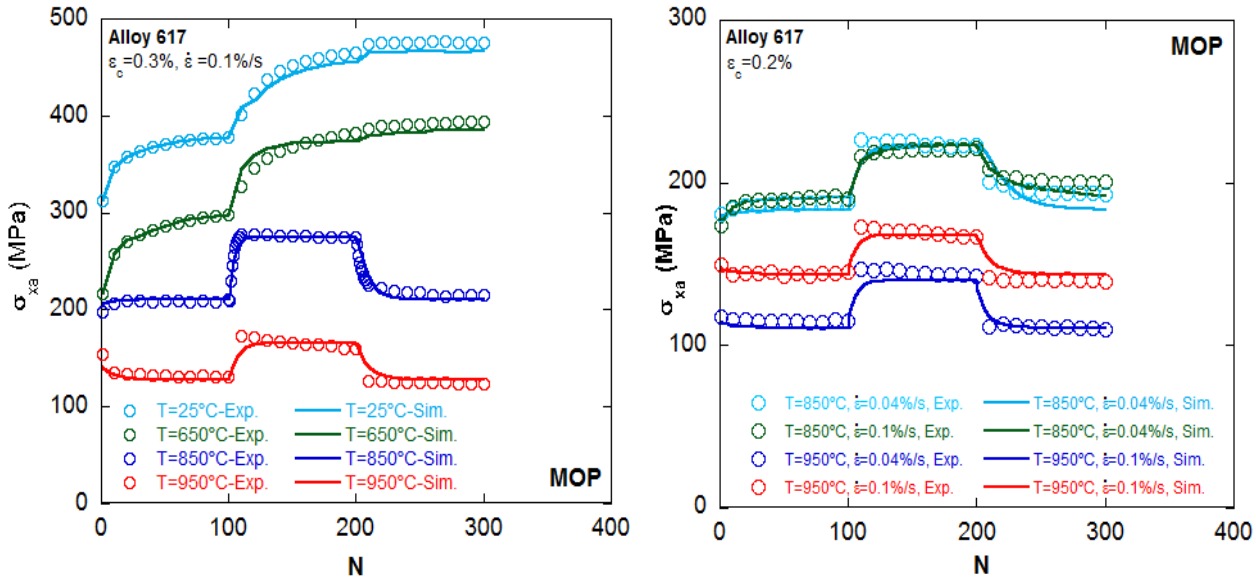

Fig. 5. Experimental (Exp) and simulated (Sim) axial stress amplitude responses, demonstrating cyclic hardening/softening under uniaxial and multiaxial loading for the three phases of the MOP multiaxial loading path under different temperature levels, and shear strain amplitudes and rates.

3. Task on Incorporation of the Modified UCM into Finite Element Software ANSYS

Development of USERMATs subroutine in order to implement the modified UCM into the finite element software ANSYS has been complete during the last quarter. Such a USERMAT with advanced UCM will allow address of ASME-NH Code issues relevant to very high temperature component design using Alloy 617. Subroutines are developed for both the solid (USERMAT3D) and shell (USERMATPS) elements in ANSYS. Radial return numerical scheme is incorporated for performing the local (integration point) computations. Thus large loading increment can be prescribed for response simulations with good accuracy and efficiency. After convergence of the UCM computation at the local level, the updated variables are transferred to ANSYS for computation and iterative equilibrium check at the component or structure level. To ensure the quadratic convergence of the global Newton iteration scheme, a tangent operator was calculated based on the converged values at the material level and transferred to ANSYS. The derivation of this consistent tangent operator for both solid and shell elements, and relevant numerical issues have presented in the last quarterly report. These USERMAT subroutines in ANSYS will allow design by inelastic analysis following the procedure in ASME-NH much more accurately than was possible before.

An Experimental Study on High Temperature Uniaxial Fatigue and Fatigue-Creep Responses of Alloy 617

P. Graham Pritchard[1], Tasnim Hassan[1,*], Laura Carroll[2]

[1]North Carolina State University, Raleigh, NC

[2]Idaho National Laboratory, Idaho Fall, ID

Abstract

Next Generation Nuclear Plants (NGNPs), in addition to generating electricity, aim to include an adjacent hydrogen production facility that will use heat generated by the reactor in the hydrogen production process. To accomplish this goal an Intermediate Heat Exchanger (IHX) will be required to transfer the heat. This IHX will be subjected to a wide variety of low-cycle fatigue loadings at high temperatures and thus alloy 617, a high temperature corrosion resistant nickel-chromium alloy, has been chosen as a potential material candidate. However, the current ASME Code does not include high temperature design provisions for alloy 617. Hence, towards the goal of incorporating alloy 617 into the ASME Code, a broad set of fatigue and fatigue-creep tests have been performed. This paper endeavors to present the wide range of material responses observed under a variety of uniaxial loading conditions to demonstrate the complexity of the high temperature low-cycle fatigue responses. In addition to ASME Code provision development, these responses will be used to develop an experimentally validated unified viscoplastic model which is presented in the next chapter.

* Corresponding author, thassan@ncsu.edu, 1-919-515-8123

1. Introduction

Next Generation Nuclear Plants (NGNP) will be used for the production of both electricity and hydrogen [1]. To increase the efficiency of electrical power generation and to allow for the efficient production of hydrogen an increase in the reactor outlet gas temperature from previous generations is required. The current design calls for the outlet gas temperature to be in the range of 850-950°C. In comparison, previous generations of nuclear power plants had an outlet gas temperature in the range of 300-550°C. Transferring heat to the hydrogen production plant will require an Intermediate Heat Exchanger (IHX). In this role, the IHX will be exposed to both high temperatures and an impure helium environment [2]. Due to reactor start-ups and shut-downs and power transients, the IHX will be subjected to low-cycle, thermomechanical fatigue loading in the temperature range 20^{o}-950^{o}C. To meet these extreme loading conditions, alloy 617, a high temperature corrosion resistant nickel-chromium alloy, has been chosen as the primary candidate material; however, the current ASME Code does not include high temperature design provisions for alloy 617.

The design of the IHX component will require a broad understanding of the failure responses of alloy 617 that occur at high temperatures, especially those involving creep and fatigue interactions which occur under low-cycle fatigue (LCF) loading. This in turn will require a large set of high temperature low-cycle fatigue data of alloy 617 which is not currently available. Furthermore, a unified constitutive model (UCM) validated against a broad set of experimental data will be needed for design by analysis following the ASME Code subsection NH methodologies. So far, very few experimental investigations of the LCF behavior of alloy 617 have been made [3]. The three main experimental investigations that have been completed previously are: The original Huntington investigation [4], High Temperature Gas Reactor (HTGR) and General Electric (GE) collaboration [5-6], and the German High Temperature Gas Reactor program. While low cycle fatigue and fatigue-creep data was generated from these programs, this data is not accessible to others for further investigation.

A large portion of the above investigations focused on the development of “typical” material parameters such as yield strength, ultimate tensile strength, elongation, fatigue life, etc. [5,7]. Particular attention was paid to developing fatigue life relationships for the alloy [8]. However, as stated earlier, the development of an experimentally validated UCM

following ASME Code provisions and methodologies will require a broader set of responses. The variation of the stress-strain hysteretic response as well as the variation of fatigue life as a function of strain or stress range, strain or stress rate, temperature, and hold time are important considerations. Furthermore, the influences of cyclic hardening/softening and strain ratcheting need to be understood clearly for safe and economic design of IHX.

Stemming from the German HTGR investigation, strain-controlled fatigue and fatigue-creep responses of alloy 617 at elevated temperatures with and without a simulated reactor environment were investigated [9-10]. Regarding fatigue, three important responses were discussed: first, at 850°C, the fatigue life decreases with decreasing applied strain-rate; second, the stress amplitude decreases with a reduction in applied strain-rate; third, the stress amplitude decreases with an increase in the applied temperature. It is also mentioned that dynamic strain aging (DSA) was observed at 750°C (for one test) and at 850°C for tests performed at higher strain-rates however a definition of what constituted a higher strain rate was not given.. The fatigue-creep portion of the investigation was performed at 950°C with three applied fatigue-creep waveforms: an applied tensile peak strain hold, a compressive peak strain hold, and a combined tensile and compressive peak strain hold. Here applied hold times varied from 5s to 120 min. Overall it was found that with an increase in the duration of the applied strain hold there was a continuous decrease in the observed fatigue life. Furthermore, it was reported that tensile holds were observed to be more damaging than either compressive or a combined tensile and compressive peak strain hold. At this point, it should be noted that this investigation has led some to assume that the applied tensile strain hold is always the most damaging case; i.e. it leads to the greatest reduction in fatigue life for alloy 617 in general. However, as will be discussed subsequently, this is not always the case.

Currently the NGNP program at the Idaho National Laboratory (INL) has been developing a large set of fatigue and fatigue-creep responses of alloy 617 for the temperature range of 25-1000°C [1-2, 10-13]. In terms of fatigue it has been found with increasing applied strain range there is a reduction in fatigue life [11]. At 850°C additional hardening was reported with increasing applied strain range while additional softening was observed at 950°C. In terms of fatigue-creep, it was found that the addition of a tensile strain hold always caused a reduction in the fatigue life. Furthermore, the fatigue life decreased with increasing hold time, up to a hold time of 10 min. In contrast with the result found in Rao et al, a further

increase in hold time did not show a further decrease in fatigue life [9-10]. The INL research effort also performed fatigue-creep tests with both compressive and tensile-compressive peak strain holds. Contrary to the observations in Rao et al. [9-10], the tension only hold was not the most damaging fatigue-creep waveform [13]. However, these tests were performed at a lower strain range (0.3% instead of 0.6%). Therefore, it is possible that the most damaging fatigue-creep loading history could depend on the applied strain range.

During plant start-ups and shut-downs, the IHX be subjected to in-phase or out-of-phase thermo-mechanical fatigue loading (TMF). During plant operation the IHX will be subjected to high temperature dwell periods between shut-downs for maintenance and refueling. Under such loading, the accumulated creep damage is significantly higher than the accumulated fatigue damage. The influence of such creep and fatigue interactions on the fatigue life of high-temperature components is not currently understood. This failure mechanism in which creep damage is more significant than the fatigue damage will be referred to as creep-fatigue in this study. On the other, fatigue damage that is more significant than creep damage will be referred to as fatigue-creep. This occurs when significant fatigue damage is developed over a large number of cycles whereas a lesser degree of creep damage is developed during short duration stress or strain holds. Tests with a full simulated creep-fatigue life are not feasible due to the long hold times and high costs associated with testing. Consequently, a rational experimental program with feasible test times is required. Additionally, it is likely that the IHX will experience multiaxial loads over the course of its operation; however, the effect of multiaxial loads on the fatigue response of alloy 617 has not been previously investigated. In addition, influence of strain ratcheting both under uniaxial and multiaxial cyclic loading on fatigue life of alloy 617 will be needed for design development of NGNP IHX.

As mentioned previously, the NGNP program at the INL has already produced a broad set of fatigue and fatigue-creep responses. However, a data set sufficient for ASME codification of alloy 617 and for the development of an experimentally validated unified constitutive model has not been available. The ASME design code subsection NH requires a constitutive model capable of accurate non-linear analysis for design by analysis. Thus an experimental program for developing a broad set of low-cycle fatigue and fatigue-creep responses under both uniaxial and multi-axial loading conditions has been undertaken. This program is a subset of the experiments required for the ASME codification of alloy 617 listed

in the INL report [1]. The data set created includes tests performed at temperatures ranging from 25-950°C, at two strain-rates, over multiple strain ranges, and with and without a one minute peak tensile hold. This data set will allow for UCM to be developed for the prediction of fatigue, fatigue-creep, and ratcheting responses over a wide variety of temperatures, strain or stress rates, strain or stress ranges, and with and without a peak tensile hold. This chapter will present and discuss only the uniaxial fatigue and fatigue-creep responses.

2. Experimental Study

2.1 Experimental Program

To broaden the understanding of alloy 617 fatigue and fatigue-creep responses, a set of isothermal uniaxial fatigue and fatigue-creep tests have been conducted. In Fig. 1 the three experimental waveforms used are shown. The first, UF1, is a strain-controlled LCF waveform. The second, UF1-MSR, is also a strain-controlled LCF waveform; however, four strain ranges are applied over the course of a test by incrementing the strain range every 50 cycles. The responses from this waveform were primarily used for UCM development. It is a compact test which allows for the development of strain range dependent modeling features. The final waveform, UF2, is a strain-controlled low cycle fatigue-creep waveform with a one minute strain hold applied at the peak tensile strain. In general, there exist three possible fatigue-creep loadings that can be prescribed: one with a tension hold, a compression hold, or with both a tension and a compression hold. As discussed previously, an earlier work had shown that, for alloy 617, and at high temperatures, a tension hold was the most damaging case, i.e. led to the shortest fatigue lives [9]. Therefore, in this investigation, tests under fatigue-creep loading have been restricted to tensile holds. However, a recent publication has shown that at the smaller strain range of 0.3% this is not case [13].

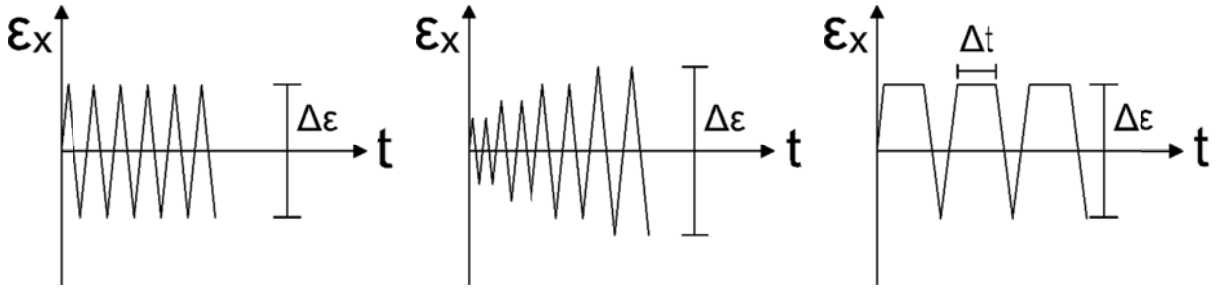

(a) Fatigue (UF1) (b) Multiple Strain-Range Fatigue (UF1-MSR) (c) Fatigue-Creep (UF2)

Fig. 1 – Loading histories prescribed in the experimental study

In order to capture a wide variety of material responses of alloy 617 a total of 26 fatigue and 8 fatigue-creep tests have been performed. In order to capture the temperature dependence of alloy 617, tests have been conducted at five temperatures ranging from 25°C – 950°C as shown in Table 1. Two different applied strain-rates were prescribed to study

strain-rate dependence. Lastly, as stated earlier, strain ranges of 0.3, 0.6, 0.8 and 1.0% were prescribed in multiple strain range tests for the development of strain-range dependent modeling features. The full list of test parameters is shown in Table 1.

Table 1 – Test Matrix

Test Type	No. of Specimens	Temp. (°C)	Strain-rate (%./s)	Strain Range (%)
UF1	16	25, 650, 750, 850, 950	0.04, 0.01	0.4, 0.6
UF1 - MSR	10	25, 650, 750, 850, 950	0.04, 0.01	0.3, 0.6, 0.8, 1.0
UF2	8	850, 950	0.04, 0.01	0.4, 0.6

2.2 Experimental Procedure

Cylindrical specimens with a diameter of 0.25 inches in the reduced section and a gage length of 0.75 in. were machined from an annealed plate of alloy 617 with the longitudinal axis parallel to the rolling direction. A detailed schematic of the specimen geometry is shown in Fig. 2 and the material composition in table 2. The stock material used in this investigation is the same as that used by Wright and Carroll. [2, 11, 13].

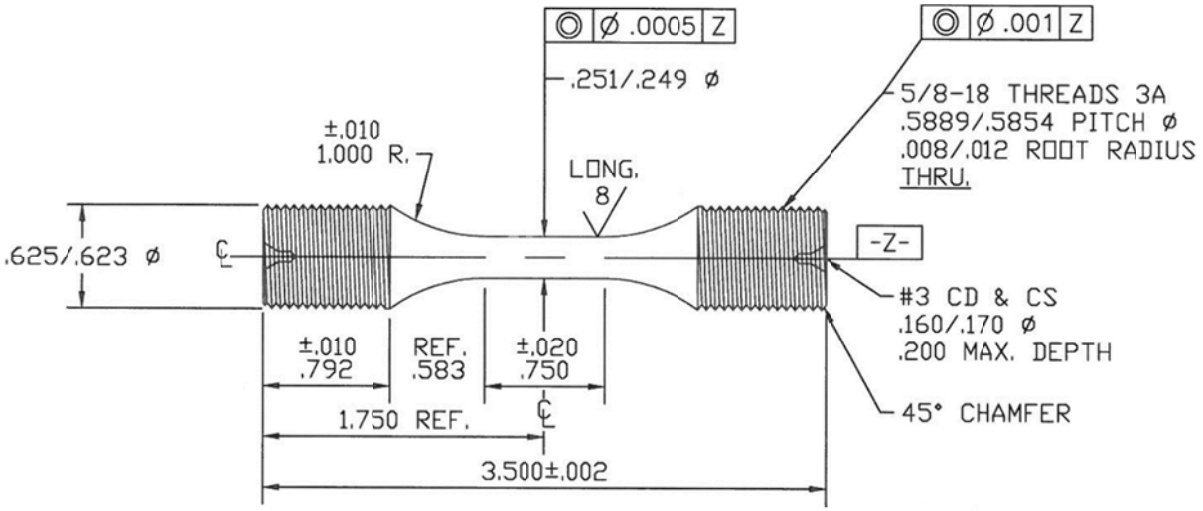

Fig. 2 – Specimen Schematic

Material testing was performed using a servo-hydraulic testing apparatus axial strain-control. Induction or furnace heating was used to bring the specimen up to the desired testing

temperature. All fatigue experiments were performed in accordance with ASTM E606-04 and fatigue-creep experiments with ASTM E2714-09.

Table 2 – Alloy 617 Composition in wt. %

Ni	C	Cr	Co	Mo	Fe	Al	Ti	Si	Cu	Mn
bal.	0.05	22.2	11.6	8.6	1.6	1.1	0.4	0.1	0.04	0.1

2.3 Parameters for Discussion of Fatigue and Fatigue-Creep Responses

In the following discussions references will be made to several different hysteretic responses of alloy 617. To facilitate discussion of the material responses it is convenient to define several useful parameters of hysteretic responses. Fig 3a presents a typical fatigue hysteresis loop performed at 950°C. Fig. 3b presents a typical fatigue-creep test also performed at 950°C with a one minute tensile strain hold. In these figures, three parameters of interest are: the maximum stress (σ_{max}), the minimum stress (σ_{min}), and the relaxed stress ($\Delta\sigma_r$). σ_{max} and σ_{min} are used to define the stress amplitude, σ_a, and the mean stress, σ_m, through equations 1 and 2. σ_a is used for displaying the degree of cyclic hardening/softening and σ_m the shift of the hysteresis loop or mean stress relaxation with cycles. The relaxed stress, $\Delta\sigma_r$, and the normalized relaxed stress, $\Delta\sigma_{r\text{-}n}$, are determined using Eqns. 3 and 4 and are used to illustrate the variation of the relaxation response with cycles.

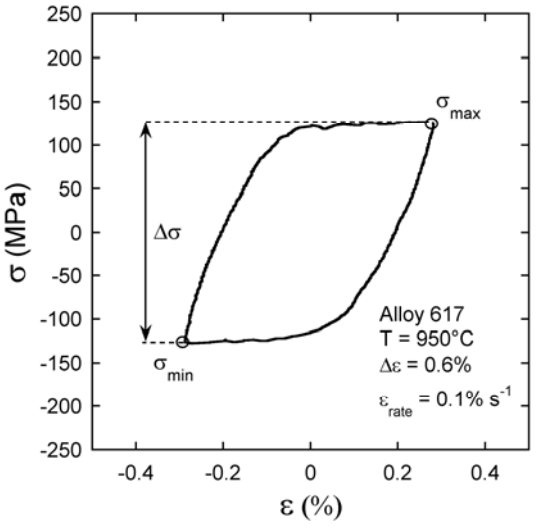

Fig. 3a: Typical fatigue stress-strain hysteresis loop

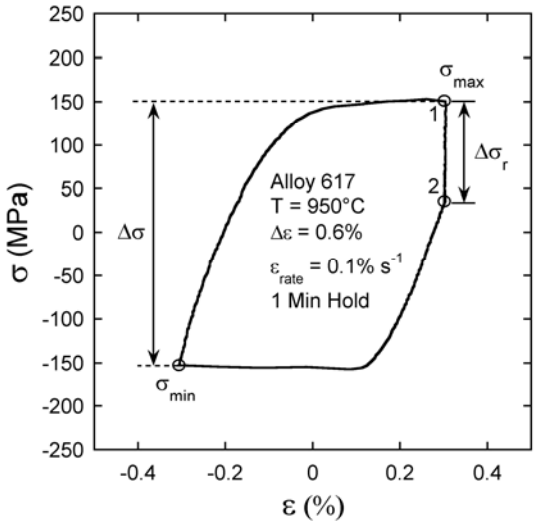

Fig. 3b: Typical fatigue-creep stress-strain hysteresis loop

$$\sigma_a = \frac{\sigma_{\max} - \sigma_{\min}}{2} \quad (1)$$

$$\sigma_m = \frac{\sigma_{\max} + \sigma_{\min}}{2} \quad (2)$$

$$\Delta\sigma_r = \sigma_1 - \sigma_2 \quad (3)$$

$$\Delta\sigma_{rn} = \frac{\Delta\sigma_r}{\sigma_1} \quad (4)$$

3. Results

3.1 Strain-Rate Dependence

Ten of the 16 UF1 tests outlined in Table 1 were performed at a strain range of 0.6%, at two strain-rates, 0.1% s^{-1} and 0.04% s^{-1}, and across five temperatures, 25, 650, 750, 850, and 950°C. For room temperature tests (25°C) a typical uniaxial stress-strain response is shown in Fig. 4a. σ_a and σ_m responses are plotted as a function of number of cycles, N, for the two strain rates investigated, 0.1% s^{-1} and 0.4% s^{-1}, in Fig. 4b. These figures demonstrate the rapid cyclic hardening observed over the initial 100 cycles followed by a shift to slow and almost steady rate of cyclic hardening. In Fig. 4b, the difference between the σ_a and σ_m responses are small to none, which indicates no effect of strain-rate on alloy 617's response for the two strain rates prescribed. Similar to above, for 650°C, a typical stress-strain response is shown in Fig. 5a and the σ_a and σ_m responses in Fig. 5b. Interestingly a large change in the cyclic response is seen with the increase in temperature. At 650°C three phases of hardening are observed: rapid initial hardening lasting about 100 cycles, medium rate hardening lasting approximately 1500 cycles, and slow steady softening seen for the rest of the test duration; A similar proportion of the hardening occurs in the first and second phases. Furthermore, while the initial σ_a at 650°C is about 100 MPa lower than the initial σ_a at 25°C, enough hardening occurs at 650°C so that the maximum σ_a seen just before failure is greater than the maximum σ_a at 25°C. Lastly it is noted that a slightly reduced σ_a was observed at the lower rate of 0.04% s^{-1} toward the end of the cycle life. For both these two temperatures the mean stress remained close to zero, which indicates symmetric hysteresis loops.

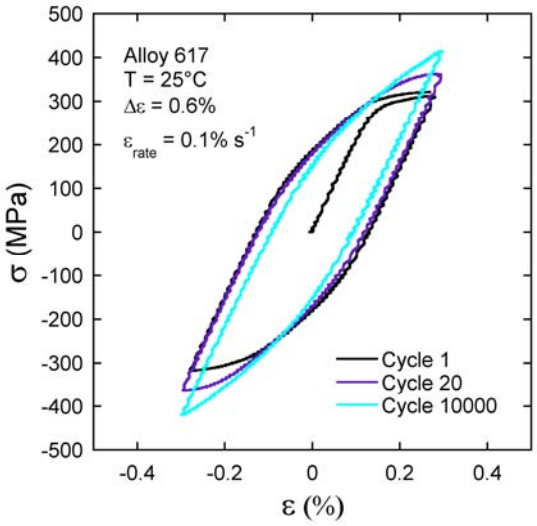

Fig. 4a: UF1 hysteresis response at 25°C

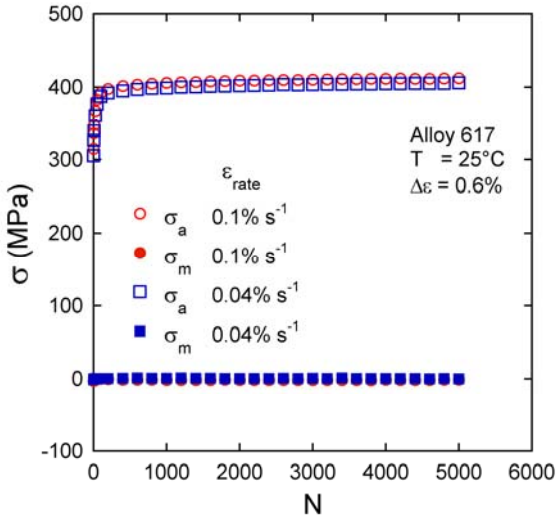

Fig. 4b: UF1 stress amplitude response at 25°C

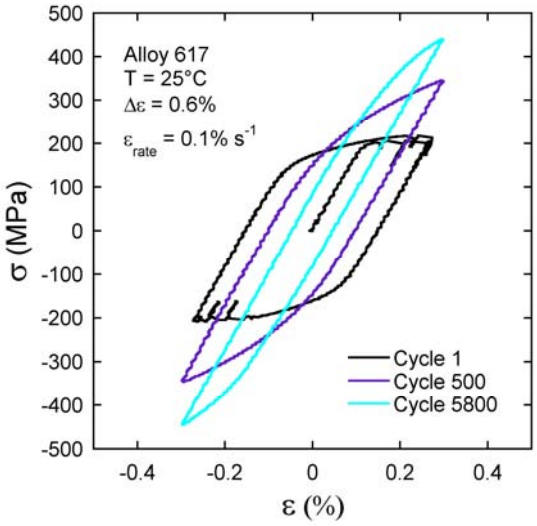

Fig. 5a: UF1 hysteresis response at 650°C

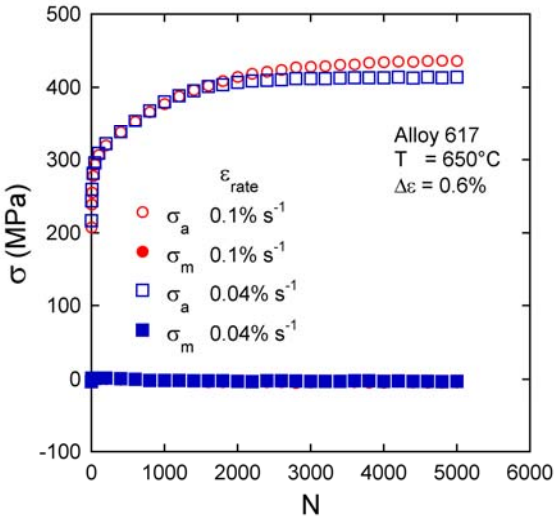

Fig. 5b: UF1 stress amplitude response at 650°C

In an investigation by Rao et al. [10] fatigue tests were performed at 750, 850, and 950°C at a strain range of 0.6% with lower strain-rates than those investigated in this study.

While the data developed in the present study alone suggests a small strain-rate effect for the temperatures of 750 and 850°C, when it is compared to the data developed from the Rao et al. [10], a broader picture of the material response is developed as shown in Figs. 6-8. Note that test performed at strain rates of 0.004% s^{-1} and 0.0004% s^{-1} have been digitized from [10]. In Fig. 6, upon reducing the strain-rate from 0.1% s^{-1} to 0.04% s^{-1} no significant difference in the responses up to about 100 cycles are observed, whereas a slight reduction in the strength is seen in the subsequent cycles accompanied by a reduction in fatigue life. Upon further reduction of the strain-rate to 0.004% s^{-1} a more prominent drop in strength is seen accompanied by an even greater decrease in fatigue life. This trend is continued at 850°C as shown in Fig. 7, where a small reduction in strength and fatigue life is seen between the two strain-rates of 0.1% s^{-1} and 0.04% s^{-1}. However, with reduced strain-rates to 0.004% s^{-1} and 0.0004% s^{-1}, a much more prominent reduction in strength, which indicates strain-rate effect, and reduction in fatigue life are observed. In addition, at 850°C, the cyclic hardening response seen at the two higher strain-rates switches to a cyclic softening response at the lower two rates. At 950°C, a strong strain-rate dependence is seen from the three rate tests plotted in Fig. 8. Interestingly, the fatigue life from the 0.04% s^{-1} test was higher than that from 0.1% s^{-1} test. It should be noted though no repetitions are available to confirm this trend. Upon further reduction in strain-rate however, the reduction in fatigue life follows the same trend seen at lower temperatures.

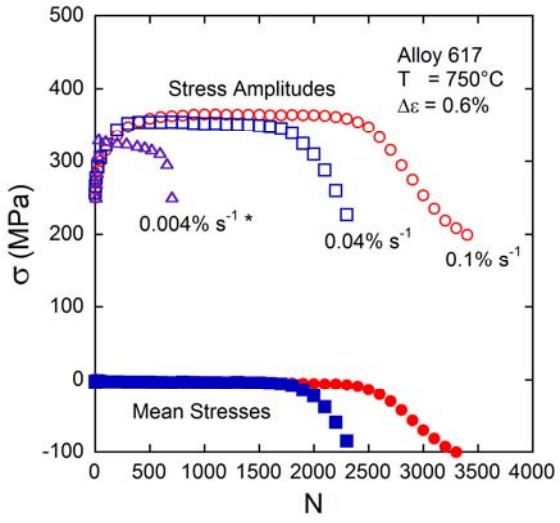

Fig. 6: Stress amplitude response at 750°C (0.004% s^{-1} data from [10])

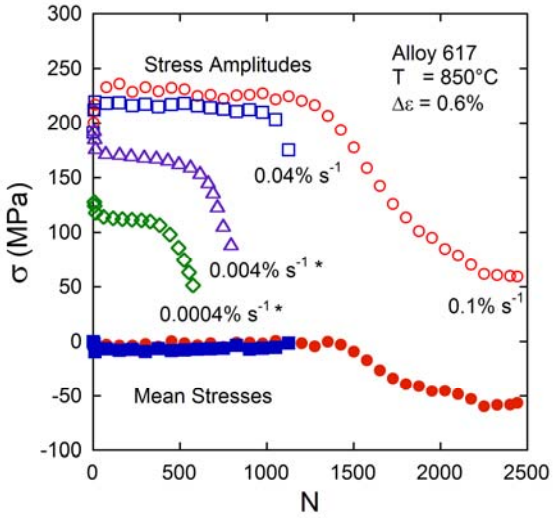

Fig. 7: Stress amplitude response at 850°C (0.004 and 0.0004% s^{-1} data from [10])

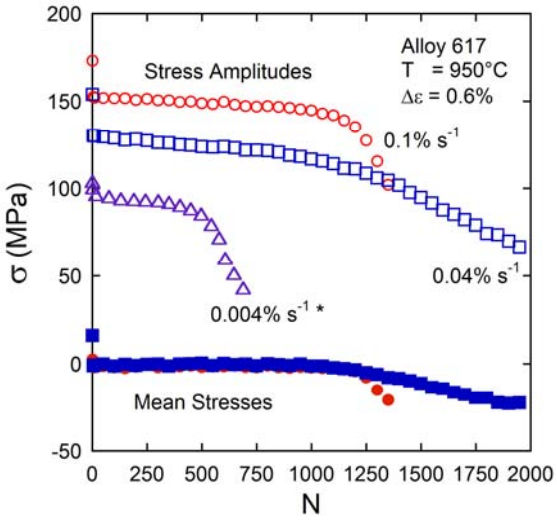

Fig. 8: Stress amplitude response at 950°C (0.004% s^{-1} data from [10])

Separate from the other temperatures tested, 850°C displays a different strain-rate dependent response as discussed in the following. At a strain-rate of 0.1% s^{-1}, there are a large amount of serrations observed in the hysteresis curves as shown in Fig. 9. However, these serrations are only present at the lower strain-rate of 0.04% s^{-1} during the first few initial cycles as shown in Fig. 10. In addition to the lack of serrations, the overall nature of the hysteresis loop changes with decreasing strain-rate as follows. For the test with the strain-rate of 0.1% s^{-1} the hysteresis loops show a well-defined elastic region upon loading and unloading. On the other hand, for the strain-rate of 0.04% s^{-1} after the initial few cycles, the well-defined elastic region disappears and afterwards no discernible elastic region is present. This similar response is more clearly demonstrated by the hysteresis loops obtained from the 950°C test as shown in Fig. 11. This feature of the hysteresis loop is important for developing and determining UCM parameters needed for simulating hysteresis loops as presented in the next chapter.

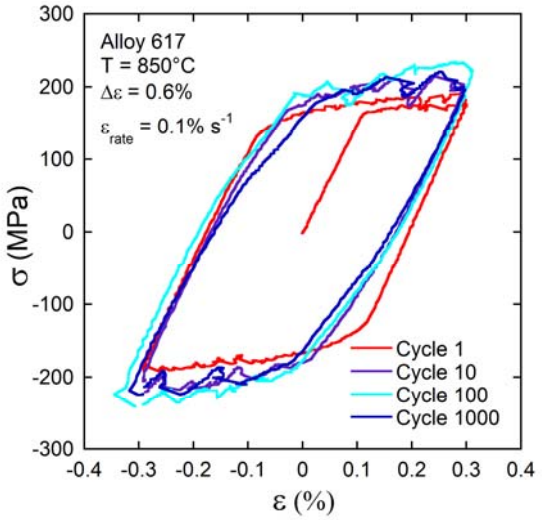

Fig. 9: Hysteresis loops at 850°C at a strain rate of 0.1% s^{-1}

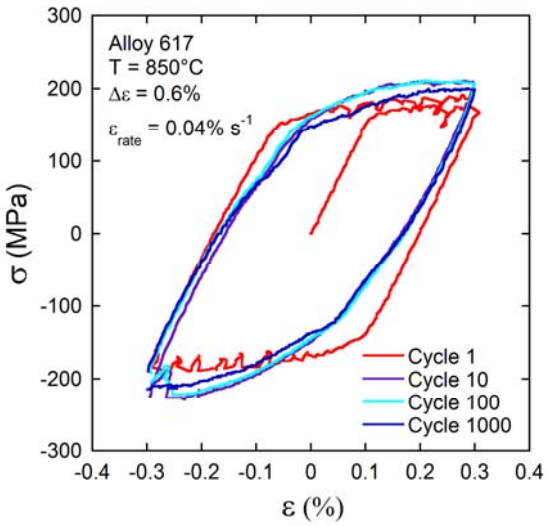

Fig. 10: Hysteresis loops at 850°C at a strain rate of 0.04% s^{-1}

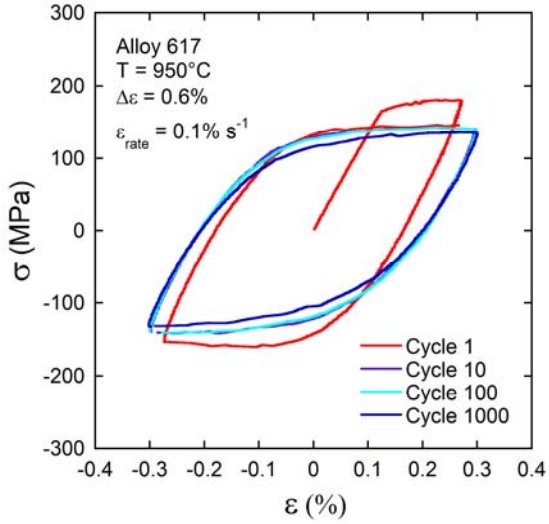

Fig. 11: Hysteresis loops at 950°C at a strain rate of 0.1% s^{-1}

3.2 Viscous Response at High Temperatures / Definition and Evolution of Overstress

With increasing temperature the material response of alloy 617 becomes progressively more viscous in nature. The viscous behavior manifests itself as stress relaxation under strain-controlled loading, while it manifests itself as creep deformation under stress-controlled loading. Currently no exact temperature has been defined which delineates between rate-independent and viscous, or rate-dependent responses for alloy 617.

In Sec. 3.1 it was demonstrated that the rate response is significant at temperatures equal to or exceeding 750°C. However the rate response manifests itself differently at different temperatures.

In general, the hysteresis curves show an initial linear elastic response followed by subsequent nonlinear plastic response. As the temperature increases above 850°C, the elastic response progressively diminishes until it becomes practically nonexistent. When this occurs the material can be considered viscous [14]. This phenomenon is depicted in Fig. 12 where three representative hysteresis loops (10^{th} cycle) from tests performed at 750°C, 850°C, and 950°C are compared. The loops are plotted in axial stress-plastic strain space; hence the elastic region is represented by a vertical linear segment upon load reversal. From this figure it is noted that at 750°C a clear linear elastic region exists. Upon increasing the temperature to 850°C, the linear region, though it exists, becomes more difficult to define. Moreover, the size of the elastic region becomes a function of the load reversal direction; the tensile direction linear region can be more easily defined than the compression direction linear region. Finally, upon reaching 950°C the linear region of the hysteresis loop in Fig. 12 disappears completely.

In addition to the lack of a linear region upon load reversal, the response at 950°C also presents another intriguing phenomenon, that is, upon load reversal there is a period during which the plastic strain increases while total strain and stress decreases (Fig. 12). This phenomenon is also present to a lesser degree at 850°C. This observation allows for a physical meaning to be attributed to the modeling variable of overstress. The overstress in viscoplastic theory represents the degree to which a stress state exists outside the yield surface. This quantity can be used as the basis for the determination of the creep strain-rate. In Fig. 13 the graphical process for determining overstress is presented. Here point **a** represents the stress at the peak tensile strain (not necessarily the peak stress) and point **b** the stress at the peak plastic strain; note that this figure is plotted in plastic strain space. The stress drop between points **a** and **b** can then be said to be a close approximation of the overstress, σ_v. This result is discussed further in the next chapter detailing the constitutive modeling of alloy 617.

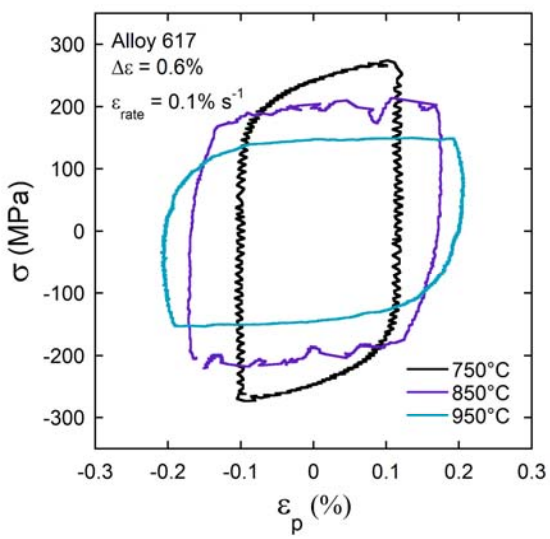

Fig. 12: Plastic hysteresis loop response at 750°C, 850°C, and 950°C

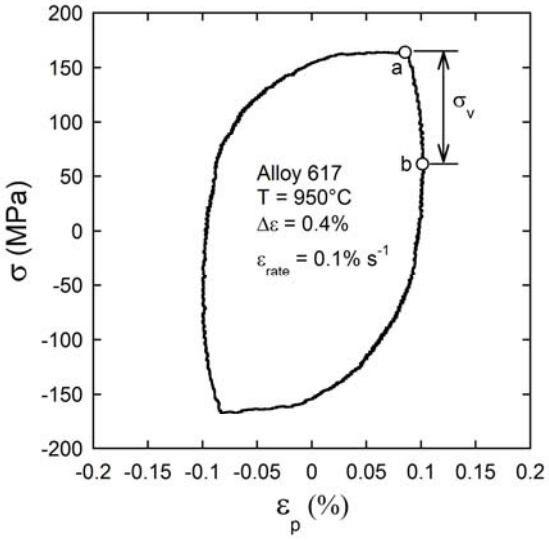

Fig. 13: Plastic hysteresis loop response at 950°C

3.3 Multiple-Strain Range Test Responses

It has long been known that the applied strain range affects the cyclic behavior of metals [15-19 and many others]. In Landgraf et al. [17], two loading protocols were suggested to investigate the strain-range dependent cyclic behavior of stress and strain: an increasing strain range test and an incremental step strain test. The former loading history has elucidated an interesting and complex behavior of metallic materials, namely the dependence of the cyclic hardening/softening behavior on the applied strain range. For example, Fig. 14 shows the hysteretic loops from such an increasing strain range test, UF1-MSR in Table 1, at 25^{o}C; the corresponding stress amplitude response is shown in Fig. 15. From these figures, two important observations can be made: first, with cycles at a given strain range there is a tendency for saturation of the stress amplitude response; second, with a further increase in the applied strain range, additional cyclic hardening is observed. A similar response was also demonstrated by many earlier studies [17-19 and many others]. From this it can be concluded both that an increase in the applied strain range can be accompanied by a change in the cyclic hardening/softening responses and that the saturation of the cyclic hardening/softening responses at a given strain range does not necessarily indicate a saturated response at all strain ranges.

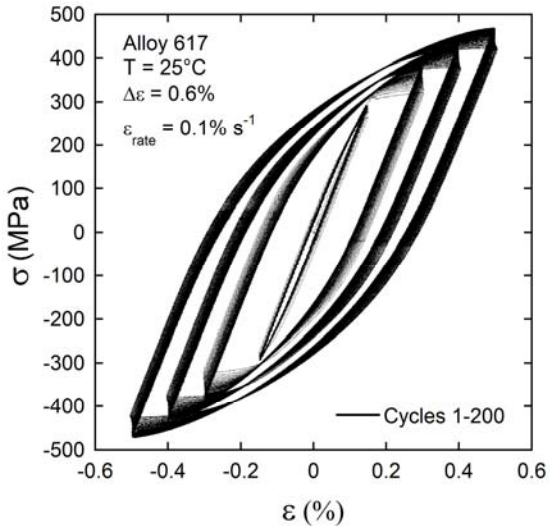

Fig. 14: Multiple strain-range test hysteresis loops at 25°C

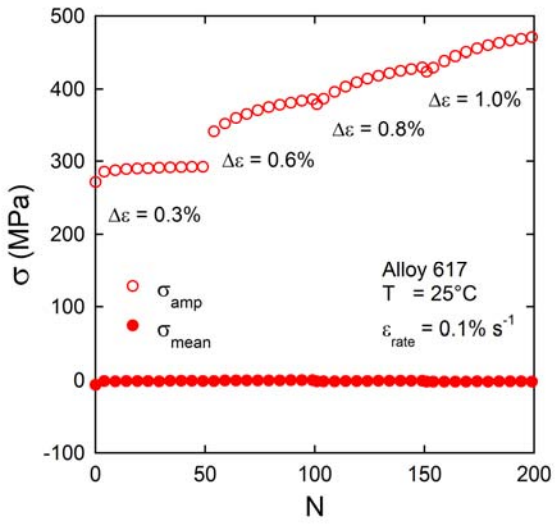

Fig. 15: Multiple strain-range test stress amplitude and mean stress responses at 25°C

As mentioned earlier and listed in Table 1 that a total of 10 multiple strain-range (UF1-MSR) tests have been performed. Here, four strain ranges were chosen to be applied over the course of the test, 0.3%, 0.6%, 0.8%, and 1.0%, 50 cycles for each range. These tests were performed over five temperatures, 25°C, 650°C, 750°C, 850°C, 950°C, and two strain-rates, 0.1% s^{-1} 0.04% s^{-1}. In order to maintain the clarity of the results two summary plots Figs. 16 and 17 are presented. In Fig 16 the responses at the lower three temperatures are shown. Here it is observed that, as is described above, with successive cycling during each applied strain range the stress amplitude has a tendency to saturate. In addition, upon increasing the strain range, further hardening is seen.

At the lower temperatures seen in Fig. 16 no strain-rate-dependence was observed during the course of the experiments at the two strain-rates tested. However, this does not indicate that there is no strain-rate dependence at these temperatures as was described earlier in the strain-rate dependence section. While there does not exist a large strain-rate effect between the strain-rates of 0.1% s^{-1} and 0.04% s^{-1}, there does exist significant strain-rate dependence at lower strain-rates (see Fig. 6). Moving to the higher temperatures of 850°C and 950°, interesting changes in the responses appear as shown in Fig. 17. First, at 850°C, strain-rate dependence becomes evident at the two higher strain-ranges of 0.8% and 1.0%. Again, it should be noted that a more significant strain-rate response may be seen at lower strain-rates (see Figs. 7 and 8). Unlike the lower temperatures, at 950°C, instead of additional

hardening, softening was observed upon increasing the strain range from 0.3% and 0.6%. With further increase of strain range no additional softening or hardening were observed during the span of the MSR tests. Additionally, 950°C was the only temperature to show complete strain-rate dependence at the two strain-rates performed in this study: 0.1% s^{-1} and 0.04% s^{-1}.

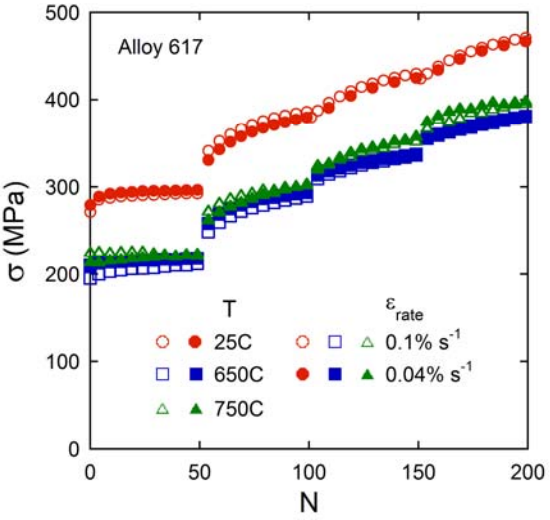

Fig. 16: Multiple strain-range test responses at 25°C, 650°C, and 750°C

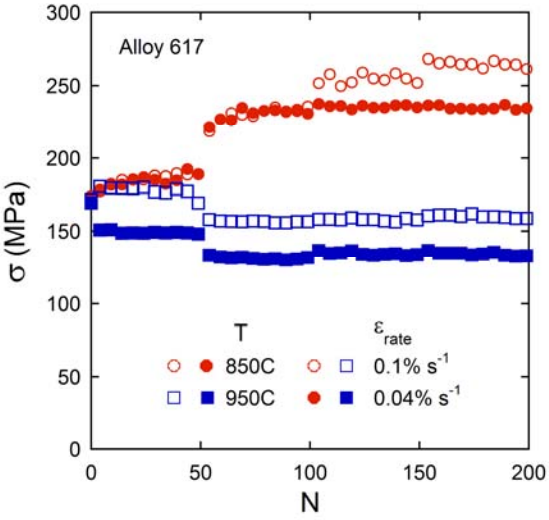

Fig. 17: Multiple strain-range test responses at 850°C and 950°C

3.4 Strain Range Dependence

As part of the NGNP program, but not in this specific investigation, fatigue tests were performed at INL over strain ranges ranging from 0.3% to 3.0% at both 850°C and 950°C [11]. In order to present the full picture of alloy 617's response some of the Wright et al. [11] results will be recapitulated here. In Figs. 18 and 19 the stress amplitude response is plotted as a function number of cycles for multiple strain ranges at both 850°C and 950°C, respectively. Examining Fig. 18 it is observed that the degree of initial cyclic hardening increases with increasing applied strain range after which a plateau is reached. In addition, with increasing applied strain range there is a progressive reduction in fatigue life. Upon increasing the temperature to 950°C the opposite stress amplitude response is seen in Fig. 19; alloy 617 softens with increasing applied strain range. For the lower two strain ranges, 0.3 and 0.4%, the material exhibits a stabilized stress amplitude response, whereas, for the higher

three strain ranges, 0.6, 1.0 and 2% cyclic softening is observed, with an increase in the degree of cyclic softening with increasing strain range. Also, like 850°C, with increasing strain range, there is a continual decrease in fatigue life.

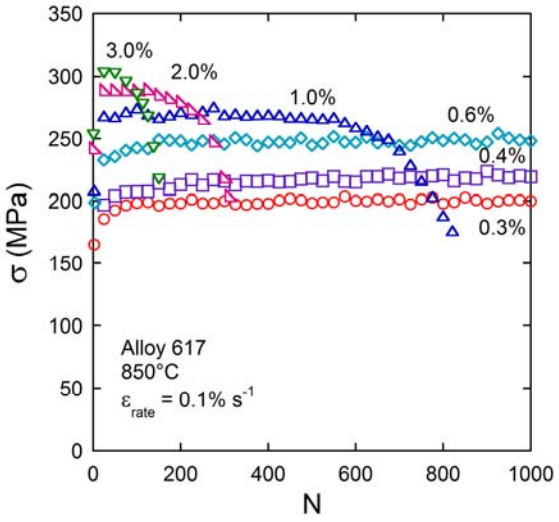

Fig. 18: Stress amplitude response at 850°C at 6 separate strain ranges (Data from [11])

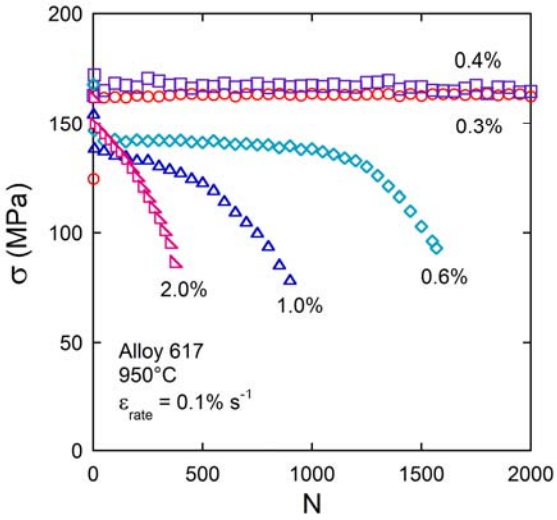

Fig. 19: Stress amplitude response at 950°C at 5 separate strain ranges (Data from [11])

Figures 20 - 23 aim to show the strain range response at different strain rates. In Fig. 20 the stress amplitude response is shown for fatigue tests performed at 950°C for two different strain ranges, 0.4% and 0.6%, and at a strain rate of 0.1% s^{-1}. In Fig. 21 the fatigue response for the same strain ranges and temperature are plotted for the lower strain rate of 0.04% s^{-1}. The main observation from these results is that as described previously with increasing applied strain range the fatigue life is reduced and cyclic softening in increased. No clear trend in the fatigue life was seen as a function of strain rate between the rates of 0.1% s^{-1} and 0.4% s^{-1}; however, as shown in Fig. 8, the much lower strain rate of 0.04% s^{-1} shows a greatly reduced fatigue life. The same responses are shown in Figs. 22 and 23 except for fatigue-creep tests with a 1 min. tensile strain hold. In this case the strain range response still holds, i.e. that increasing applied strain range yields a greater degree of cyclic softening and a reduced fatigue life; however, again no clear trend was seen in the fatigue life as a function of strain between 0.1% s^{-1} and 0.4% s^{-1}.

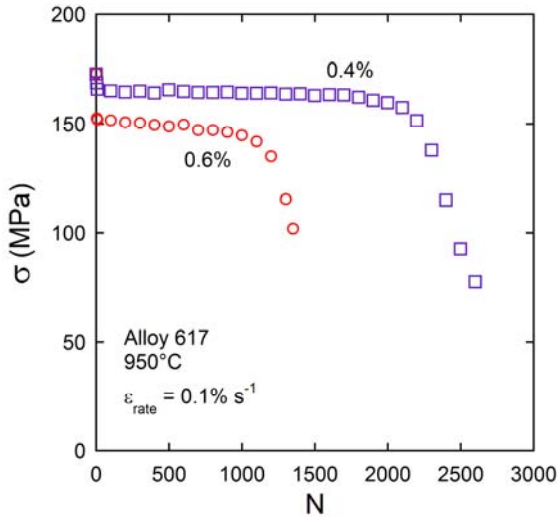

Fig. 20: Stress amplitude comparison of fatigue tests performed at a strain range of either 0.4% and 0.6%, strain rate of 0.1% s^{-1} and at a temperature of 950°C

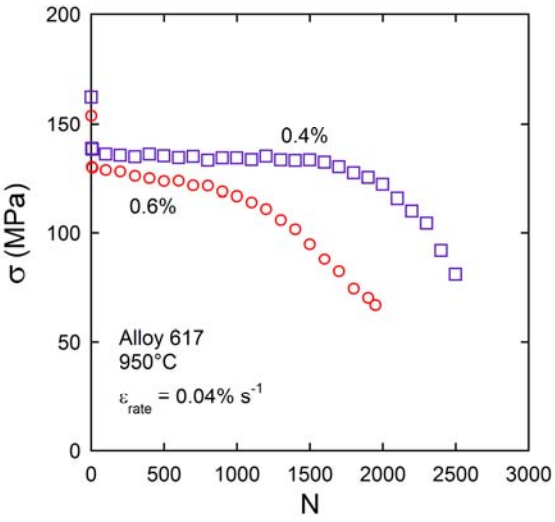

Fig. 21: Stress amplitude comparison of fatigue tests performed at a strain range of either 0.4% and 0.6%, strain rate of 0.04% s^{-1} and at a temperature of 950°C

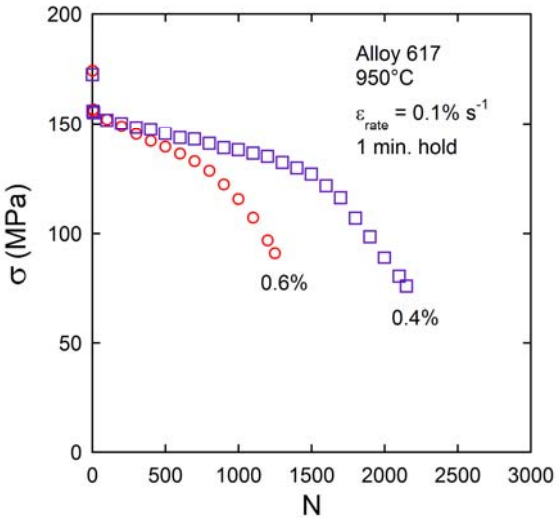

Fig. 22: Stress amplitude comparison of fatigue-creep tests performed at a strain range of either 0.4% or 0.6%, strain rate of 0.1% s^{-1} and at a temperature of 950°C

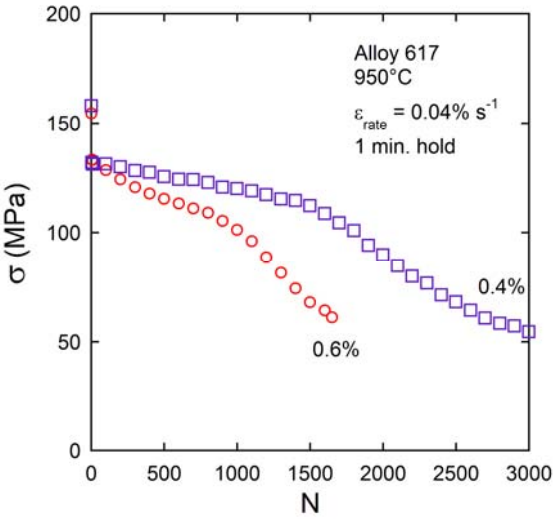

Fig. 23: Stress amplitude comparison of fatigue-creep tests performed at a strain range of either 0.4% or 0.6%, strain rate of 0.04% s^{-1} and at a temperature of 950°C

3.5 Fatigue-Creep Responses

In total eight fatigue-creep tests have been performed as shown in Table 1. At 850°C four tests have been performed at a strain range of 0.6% and at two strain-rates, 0.1% s^{-1} and 0.04% s^{-1} with one repeat. A typical fatigue hysteresis loop response at 850^{o}C performed at 0.1% s^{-1} is shown in Fig. 24a and typical fatigue-creep hysteresis loop response at 850°C in Fig. 24b. In Fig. 24c, stress amplitude responses are plotted as function of loading history (fatigue or fatigue-creep), strain rate, and number of cycles. It was found that at that at 850°C the application of a one minute tensile strain hold led to a reduced degree of initial cyclic hardening and increase cyclic softening later in the cycle life. In addition, a reduction in fatigue life was observed when a one minute tensile strain hold was applied at a strain rate of 0.1% s^{-1}; however, when a one minute strain hold was applied at 0.04% s^{-1} no trend in the fatigue life was observed with the available data.

At 950°C four tests were performed in total, two at each strain range (0.4% and 0.6%) and at the two aforementioned strain rates. A typical fatigue-creep hysteresis loop response from 950^{o}C test is shown in Fig. 25a and stress relaxation as a function of time during the hold in Fig. 25b. It was observed that at 950°C first a period of quick relaxation occurred during the first 10-25 seconds followed by slow and gradual relaxation for the rest of the hold time. Note that the origin of the time axis in Fig. 25b corresponds to the beginning of the tensile strain hold. The stress amplitude responses at a strain range of 0.4% and 0.6% are plotted in Figs. 26a and b as function of the peak hold, strain rate and number of cycles. Similar to 850°C it was found that a one minute tensile strain hold led to increased cyclic softening (Figs. 26a and b). At 950°C the applied tension hold leads to an increased rate of cyclic softening at every strain-rate and strain range as seen in Figs. 25 and 26; however, at 950°C a one minute tensile strain hold led to reduced fatigue lives at both strain rates investigated.

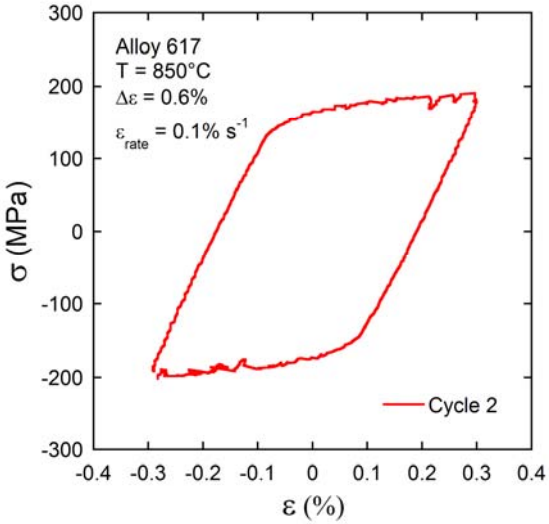

Fig. 24a: Stress-strain hysteresis response of fatigue test performed at 850°C, a strain range of 0.6%, and a strain rate of 0.1% s^{-1}.

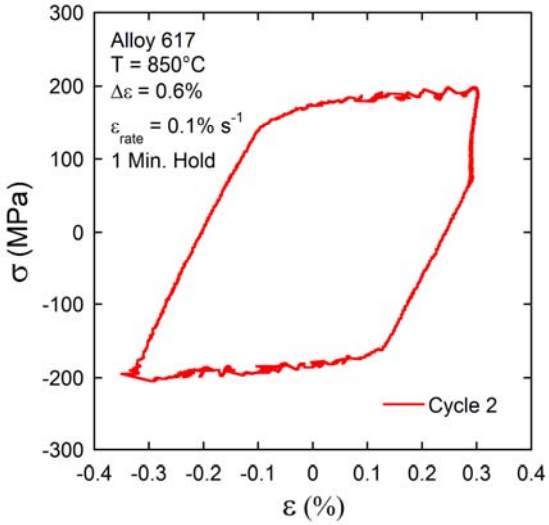

Fig. 24b: Stress-strain hysteresis response of fatigue-creep test performed at 850°C, a strain range of 0.6%, a strain rate of 0.1% s^{-1}, and a 1 min. tensile strain hold.

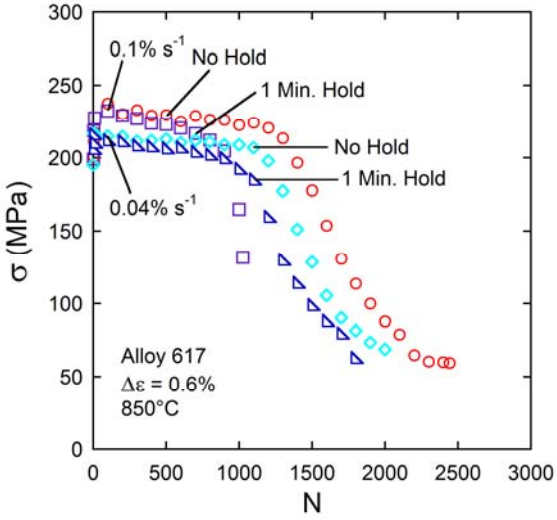

Fig. 24c: Stress amplitude comparison of fatigue and fatigue-creep tests performed at a strain range of 0.6%, two strain rates and a temperature of 850°C

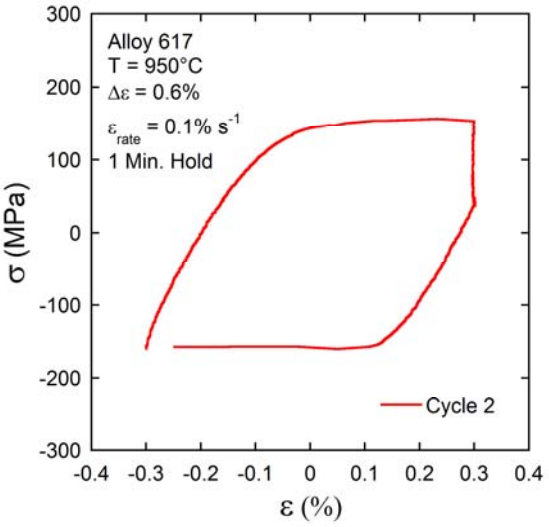

Fig. 25a: Stress-strain hysteresis response of fatigue-creep test performed at 950°C, a strain range of 0.6%, a strain rate of 0.1% s^{-1}, and a 1 min. tensile strain hold

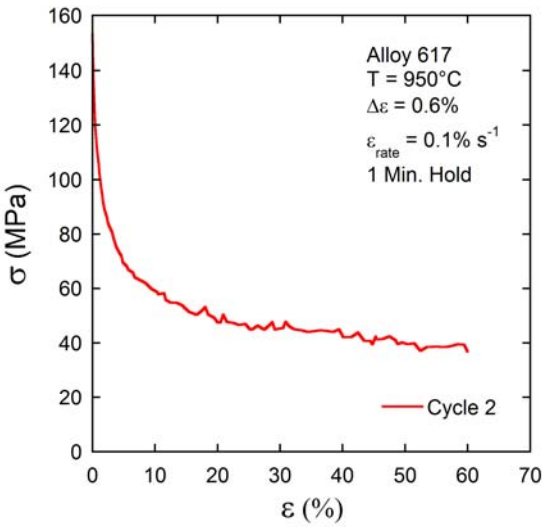

Fig. 25b: Stress relaxation response during 1 min. tensile strain hold for a fatigue-creep test performed at 950°C, strain range of 0.6% and a strain rate of 0.1% s^{-1}

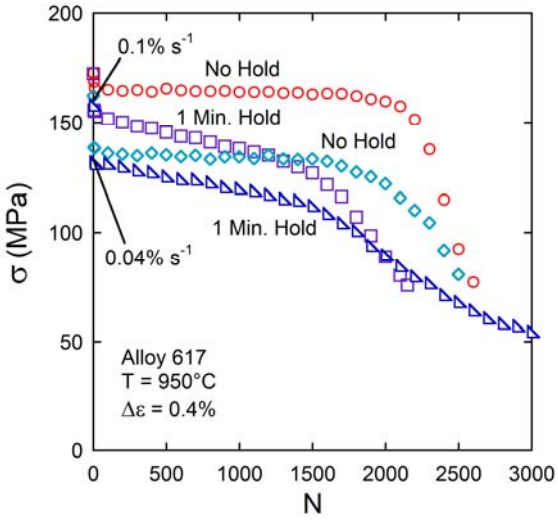

Fig. 26a: Stress amplitude comparison of fatigue and fatigue-creep tests performed at a strain range of 0.4%, two strain rates and a temperature of 950°C

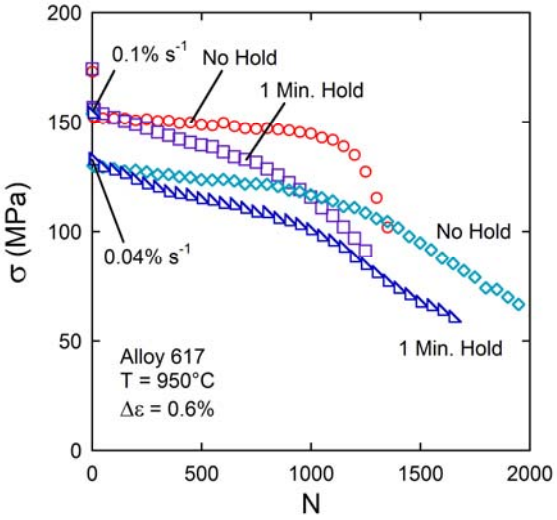

Fig. 26b: Stress amplitude comparison of fatigue and fatigue-creep tests performed at a strain range of 0.6%, two strain rates and a temperature of 950°C

These results hold with the results found in Carroll et al. [12] where an applied tension hold led to an increase in the cycle softening response as well as decreased fatigue lives at 950°C. In Carroll et al. [12], fatigue-creep tests were performed at 950°C, at three strain ranges, 0.3, 0.6, and 1.0%, and with up to four tension strain hold durations of 3, 10, 30, and 150 min. It was observed that the there was no further decrease in the stress

amplitude response with hold times greater than 3 min. Additionally, it was found that at a strain range of 0.3% hold times greater than 3 min. did not cause a further decrease in fatigue life. At the larger strain ranges of 0.6% and 1.0%, no further decrease in fatigue life was observed with a hold times greater than or equal to 10 min. In contrast, Rao et al. [9] found that at 950°C and at a strain range of 0.6%, further increases in hold times always yielded further reductions in fatigue life for tensile, compressive, and tensile and compressive strain holds.

From a constitutive modeling perspective it is important to quantify the degree of relaxation for a given applied hold time. In Fig. 27 the relaxed stress, as outlined in Fig. 3, is presented against number of cycles. In general, it is observed that with cycles, the magnitude of relaxation decreases with a similar trend as the cyclic softening response. Fig. 28 displays the normalized relaxed stress at 950°C as defined by Eqn. 4. It is interesting to note that initially the normalized relaxed stress is constant with cycles, whereas later in the cycle life the normalized relaxed stress decreases as shown in Fig. 28. This indicates that for a large portion of the cycle life the magnitude of relaxation is proportional to the peak tensile stress, but this proportionality breaks down towards the end of the cycle life as damage accumulates.

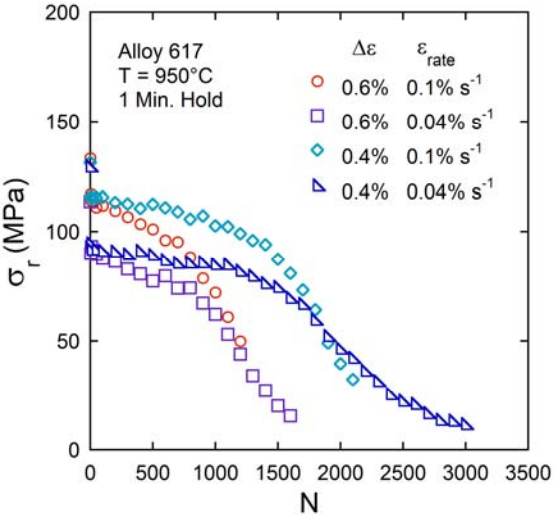

Fig. 27: Relaxed stress against number of cycles for fatigue-creep tests performed at 950°C.

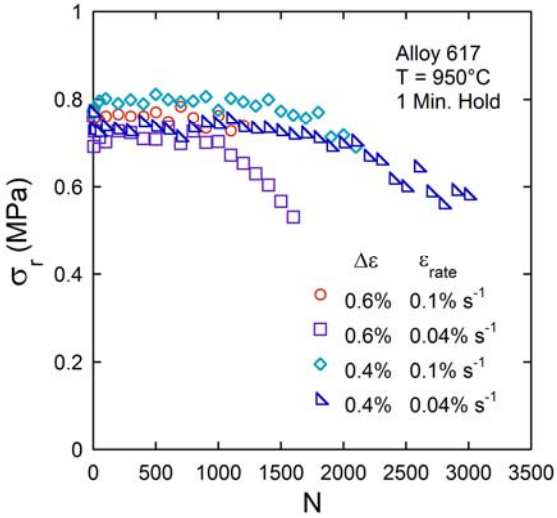

Fig. 28: Normalized relaxed stress against number of cycles for fatigue-creep tests performed at 950°C.

3.6 Plastic Energy Dissipation

Currently, there exist many different types of life estimating techniques for predicting the fatigue life of various metals or alloys. These include the Manson-Coffin relationships for low-cycle-fatigue (LCF) and the stress-life (S-N) equations or curves for high cycle fatigue (HCF). However, these rules consider either the plastic strain range in the case of LCF or the peak stress for HCF and not the relationship between them. Therefore, to consider the distinct material hysteresis response, a composite fatigue failure criterion based on dissipated plastic strain energy has been suggested by many researchers [20]. Hence, it will be endeavored to elucidate the dissipated plastic strain energy response for alloy 617 such that future researches may use the information in the development of a dissipated plastic strain energy criterion for ASME codification.

To determine the dissipated plastic strain energy the following approach was used: convert total strain into plastic strain and then calculate the incremental dissipated energy using the trapezoidal rule as shown in Eqn. 5. Then the total dissipated energy for that cycle was calculated as the summation of each increment as shown in Eqn. 6. The benefit of calculating the hysteresis area in plastic strain space is that the negative area experienced during unloading does not have to be removed. This allows for an incremental approach to be easily implemented.

$$\Delta W_i = \frac{1}{2}\left(\varepsilon_{p,i} - \varepsilon_{p,i-1}\right) * \left(\sigma_i + \sigma_{i-1}\right) \tag{5}$$

$$\Delta W = \sum_{i=1}^{n} \Delta W_i \tag{6}$$

Figs. 29 and 30 present the dissipated plastic energy per cycle as a function of temperature performed at a strain range of 0.6% and a strain-rate of 0.1% s^{-1}. Here it is observed that, with increasing temperature, there is only a small degree of variation in the initial plastic strain energy dissipated for the temperatures of 25°C – 850°C. However, this trend does not hold at 950°C. Unlike the responses presented in Morrow [20], the plastic strain energy per cycle only reached a stable value at 25°C, which itself had a stable cyclic hardening response after the initial 100 cycles. Instead, every other temperature showed a

trend of decreasing plastic strain energy dissipation with successive cycling. At 650 and 750°C this reduction is caused by the large degree of cyclic hardening which reduces the plastic strain range of the hysteresis loops. On the other hand, at 850 and 950°C, this reduction is due to the reduction in peak stress from cyclic softening. Therefore, it is noted that under strain control loading, the plastic strain energy response itself cannot be used to describe the cyclic hardening/softening behavior of the material.

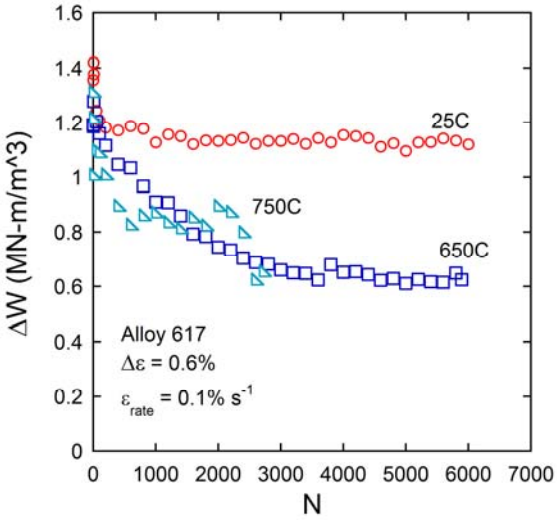

Fig. 29: Plastic strain energy dissipation per cycle against cycles for fatigue tests at 25°C, 650°C, 750°C.

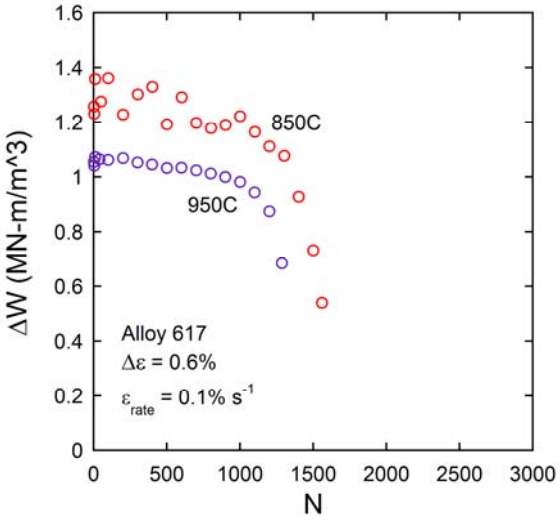

Fig. 30: Plastic strain energy dissipation per cycle against cycles for fatigue tests at 850°C and 950°C.

The effect of strain range on the plastic strain energy response can be seen in Fig. 31. Here with a reduction in strain range there is a significant decrease in the plastic strain energy response. Again, the cyclic plastic strain energy response varies relative to cyclic stress amplitude response for a given strain range. Thus a test showing a stable cyclic stress amplitude response will also show a stable plastic strain energy response, however, tests with a softening or hardening cyclic stress amplitude response will likely show a variable plastic strain energy response.

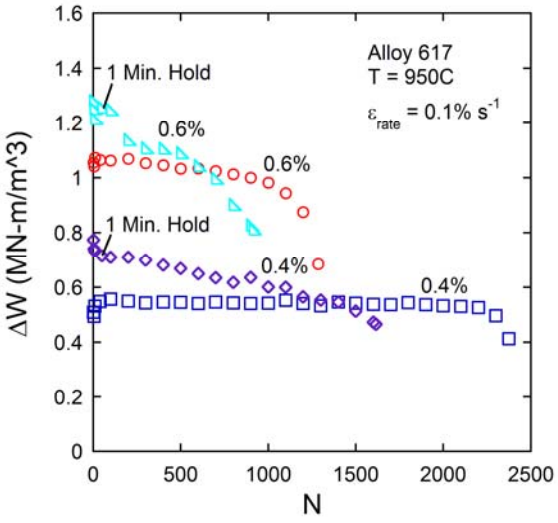

Fig. 31: Plastic strain energy dissipation per cycle against cycles comparison of strain range and hold time at 950°C

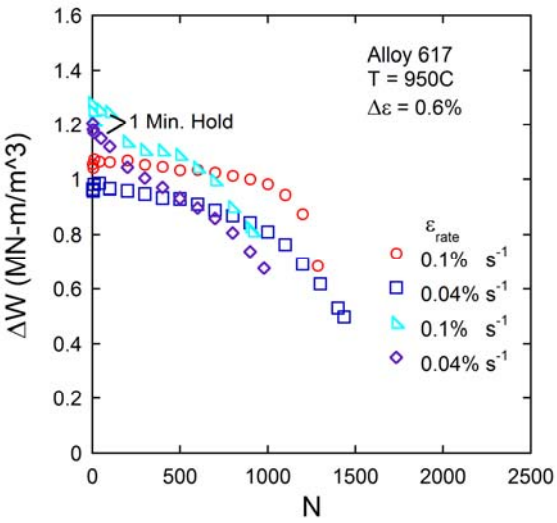

Fig. 32: Plastic strain energy dissipation per cycle against cycles comparison of strain rate and hold time at 950°C

All other parameters being equal, a test with an applied tensile strain hold will have a larger plastic strain range. Thus, under fatigue-creep loading, the plastic strain energy per cycle is initially higher compared to fatigue loading. But due to the cyclic softening observed under fatigue-creep loading, there is a reduction in the plastic strain energy observed per cycle. However, it is noted that cyclic softening by itself will not always cause a decreased plastic strain energy response. If the widening of the hysteresis loop is large enough to compensate for the lower stresses, a stable or even increasing energy response can exist. Finally, the applied strain-rate did not have a large effect on the plastic strain energy response at 950°C as shown in Fig. 32.

In Table 3 the average plastic strain energy dissipated per cycle, total plastic strain energy dissipated, and the number of cycles to failure is shown for each applicable experiment performed. The average plastic strain energy per cycle was determined by taking the mean of each available data point up to the failure cycle. The total dissipated energy was taken as the integral of the plastic strain energy versus cycle curve. That is the summation of the plastic strain energy dissipated in each cycle. The dissipated energy for cycles that hysteretic data was not recorded for was taken as the average of the energy of the previously recorded cycle and the next recorded cycle. Again, the summation was terminated at the failure cycle for the given test.

Table 3 – Plastic Strain Energy Response

Temp.	Hold Time	Δε	ε̇	Avg. ΔW	W_f	N_f
(°C)	Min.	(%)	(% s^{-1})	MN-m/m^3	MN-m/m^3	(Cycles)
650	-	0.6	0.1	1.04	4412	5895
	-	0.6	0.04	1.03	4935	6475
750C	-	0.6	0.1	1.01	2324	2725
	-	0.6	0.04	1.07	1953	2060
850C	-	0.6	0.1	1.05	1812	1685
	-	0.6	0.1	1.25	1826	1560
	-	0.6	0.04	1.16	1494	1355
	-	0.6	0.04	1.18	1311	1135
	1	0.6	0.1	1.47	1581	1165
	1	0.6	0.1	1.49	1389	985
	1	0.6	0.04	1.39	1880	1440
	1	0.6	0.04	1.39	1553	1180
950	-	0.4	0.1	0.54	1275	2375
	-	0.4	0.04	0.50	1104	2285
	-	0.6	0.1	1.04	1288	1285
	-	0.6	0.04	0.92	1205	1435
	1	0.4	0.1	0.71	1003	1615
	1	0.4	0.04	0.65	959	1700
	1	0.6	0.1	1.22	978	915
	1	0.6	0.04	1.11	914	980

3.7 Variability in Alloy 617 Responses

A concurrent study performed by the Idaho National Laboratory has generated a large set of high temperature, fatigue and fatigue-creep data including, in some cases, up to four repeat tests in the NDMASS data base [1-2, 11-13]. With the availability of repeat tests, some observations on the variability can be made. In general, variability in the fatigue life is expected. However, from a constitutive modeling perspective the variability of stress amplitude, cyclic hardening/softening, and hysteresis loop shape are equally as important.

Beginning with the fatigue tests at 850°C and in the data set developed by the INL for the NDMASS data base [1-12, 11-13], very little variation is seen in the stress amplitude, cyclic hardening/softening, and hysteresis loop shape responses. However, at the strain range of 0.6%, and a strain-rate of 0.1% s^{-1} this study has produced two additional tests with the same test parameters. Comparing the responses between the two data sets shows a larger variability than seen previously. In Fig. 33 the data set produced by the INL, depicted as

circles, triangles, and squares, shows a greater degree of cyclic hardening compared to responses from this study. However, it should be noted that the fatigue lived from both data sets did not vary markedly.

Moving to the fatigue tests performed at 950°C, a larger degree of variation in the material response is seen in repeated tests. In particular, the strain ranges of 0.3%, 0.6%, and 1.0% displayed the largest variations. In each case there tends to be an outlying experiment that exhibits a markedly different stress amplitude response. For example, Figs. 34-36 show for the strain ranges of 0.3%, 0.6% and 1.0%, every test performed under the same loading conditions for that strain range. At the strain ranges of 0.3% and 0.6%, the outlying test exhibits a stronger stress amplitude response, and thus, can be excluded for modeling purposes. However, at 0.6%, the outlying test displays a softer stress amplitude response and cannot be excluded.

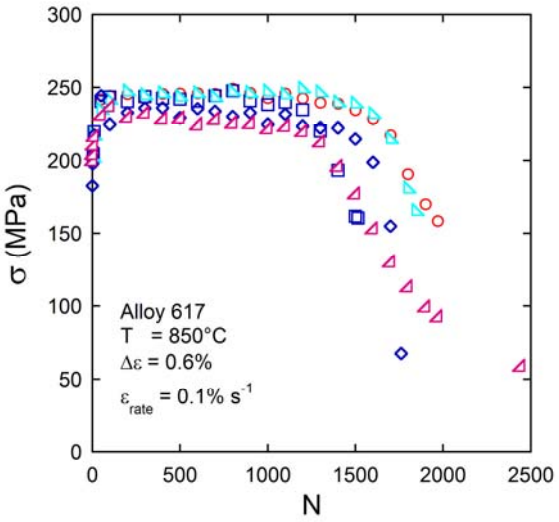

Fig. 33: Strain amplitude response (SAR) at 850°C, at strain range of 0.6%, and a strain rate of 0.1% s^{-1}

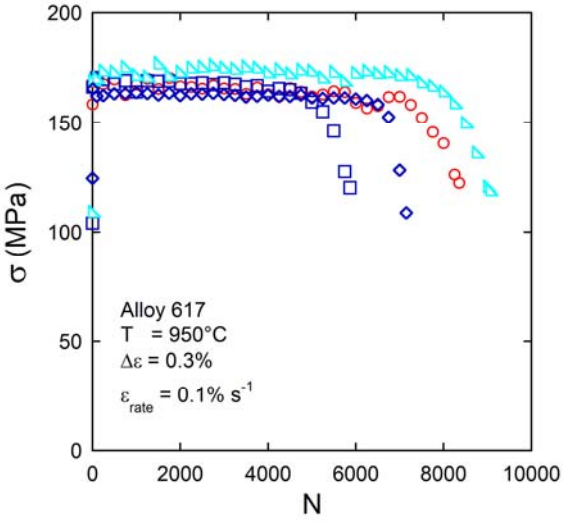

Fig. 34: Strain amplitude response at 950°C, at strain range of 0.3%, and a strain rate of 0.1% s^{-1}

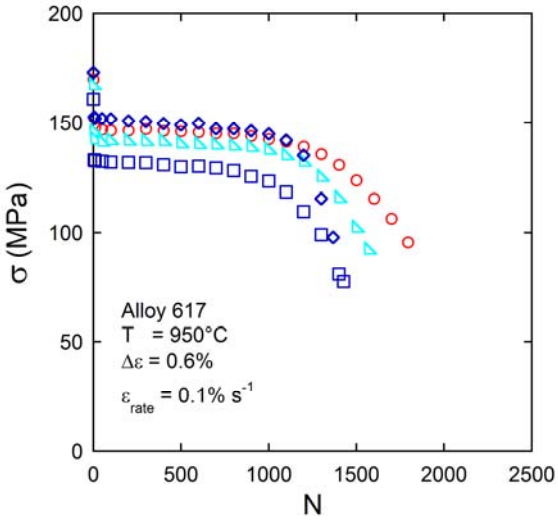

Fig. 35: SAR at 950°C, at strain range of 0.6%, and a strain rate of 0.1% s^{-1}

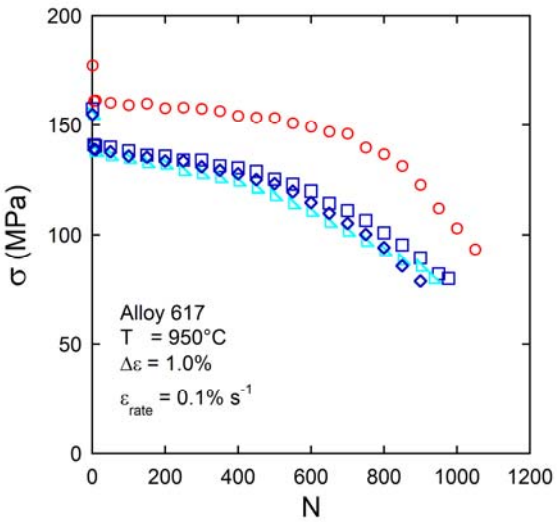

Fig. 36: SAR at 950°C, at strain range of 1.0%, and a strain rate of 0.1% s^{-1}

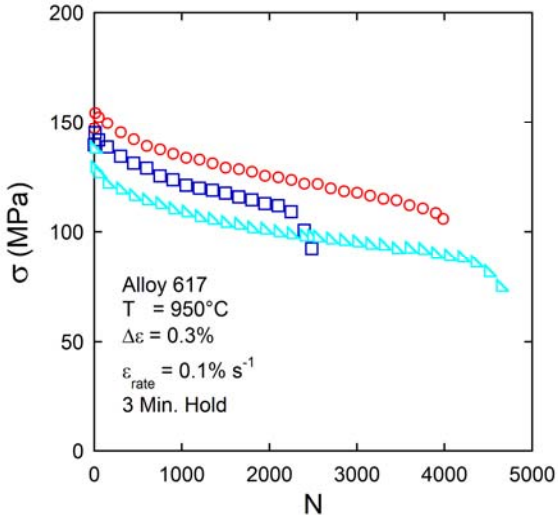

Fig. 37: Strain amplitude response at 950°C, at strain range of 0.3%, and a strain rate of 0.1% s^{-1} and a hold time of 3 min.

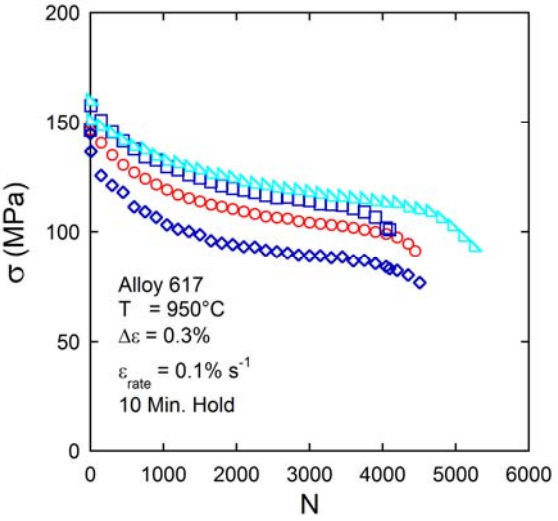

Fig. 38: Strain amplitude response at 950°C, at strain range of 0.3%, and a strain rate of 0.1% s^{-1} and a hold time of 10 min.

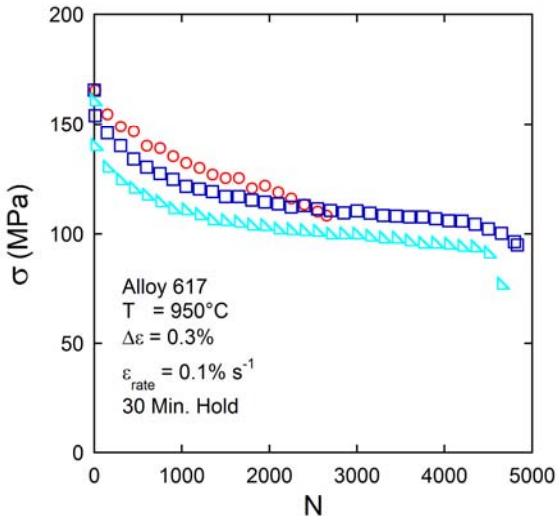

Fig. 38: Strain amplitude response at 950°C, at strain range of 0.3%, and a strain rate of 0.1% s^{-1} and a hold time of 30 min.

Thus far, only the variability in the fatigue response has been discussed. In the present study, at 850°C, two fatigue-creep tests were repeated. But these tests did not show a significant degree of variation in their stress amplitude response. In contrast, at 950°C and in the data set developed at the INL a greater extend of variation in the material strength is observed for repeated tests. For example, in Figs. 37 through 38 the degree of variation in the material response is evident. Lastly, it should be noted that for all of repeated experiments performed between this investigation and the INL's, only two experiments displayed a significant deviation in the trend of cyclic hardening or softening. Specifically, the two aforementioned fatigue tests conducted in this investigation which showed cyclic softening whereas the tests performed under the same conditions in the INL investigation showed a plateau of stress. Therefore, in general, it is observed that the average material strength in the duration of a test is the variable most subject to fluctuations and not the rate at which cyclic hardening or softening occurs. That is to say that the stress amplitude curves have the greatest tendency to shift along the stress axis without a change in slope.

4. Conclusion

A broad range of low-cycle fatigue and fatigue-creep responses have been developed for alloy 617 for the temperature range 25°C to 950°C. It has been found at temperatures

ranging from 25°C to 750°C there exists significant cyclic hardening in the material response. As the temperature increases this response reduces to only to a slight degree of cyclic hardening at 850°C and, depending on the loading conditions, softening at 950°C. For the two loading rates investigated in this study alloy 617 displays relatively rate-independent behavior at temperatures less than or equal to 750°C. However at both 750°C and 850°C rate-dependence becomes much more prominent at lower strain-rates [10]. Alloy 617 shows strain range-dependence at all of the temperatures investigated. This manifested itself as increased hardening with increasing applied strain range from 25°C to 850°C; however, at 950°C additional softening was seen with an increasing strain range. Higher applied strain ranges at all temperatures lead to shorter fatigue lives. The application of a tensile strain hold led to both a shorter fatigue life and increased cyclic softening at both 850°C and 950°C. Dissipated plastic strain energy per cycle was found to decrease with cycles for both the cyclic hardening responses seen at 25°C – 750°C and the cyclic softening response seen 850°C and 950°C and thus cannot be related directly to the stress amplitude response. Furthermore, it was found that for all other testing parameters being constant, fatigue-creep tests displayed higher dissipated plastic strain energy per cycle in comparison to fatigue tests. Finally, at 950°C a large variability was seen in the cyclic stress amplitude response for repeated tests, especially under fatigue-creep loading.

5. Acknowledgements

This research is being performed using funding received from the DOE Office of Nuclear Energy's Nuclear Energy University Programs.

6. References

[1] Wright, J.K. (2008). Next Generation Nuclear Plant Intermediate Heat Exchanger Materials Research and Development Plan. *Idaho National Laboratory, PNL – 2804.*

[2] Carroll, L.J., Cabet, C., Madland, R., Wright, R.N. (2011) Creep and Environmental Effect on the High Temperature Creep-Fatigue Behavior of Alloy 617. *J. of ASTM Intl,* Vol. 8, No. 6.

[3] Ren, W., Swindeman, R. (2009) A Review on Current Status of Alloys 617 and 230 for Gen IV Nuclear Reactor Internals and Heat Exchangers. *J. of Pressure Vessel Technology,* Vol. 131.

[4] Huntington Alloys, Inc. (1983) Inconel Alloy 617 Stress Rupture and Tensile Data Package.

[5] McCoy, H. E., and King, J. F. (1985) Mechanical Properties of Inconel 617 and 618. *U.S. Department of Energy, Report No. ORNL/TM-9337.*

[6] Baldwin, D. H., Kimball, O. F., and Williams, R. A. (1986) Design Data for Reference Alloys: Inconel 617 and Alloy 800H. *General Electric Companyfor the Department of Energy, Contract No. DE-AC03-80ET34034.*

[7] Strizak, J.P., Brinkman, C. R., Booker, M.K., Rittenhouse, P.L. (1982) The Influence of Temperature Environment, and Thermal Aging on the Continuous Cycle Fatigue Behavior of Hastelloy X and Inconel 617. *Oak Ridge National Laboratory, Contract No. W-7405-eng-26.*

[8] Burke, M.A., and Beck, C.G. (1984) The High Temperature Low Cycle Fatigue Behavior of the Nickel Base Alloy IN-617. *Metallurgical Transactions A,* Vol. 15A, pp. 661-670.

[9] Rao, K.B.S, Meurer, H.P., Schuster, H. (1988) Creep-Fatigue Interaction of Inconel 617 at 950°C in Simulated Nuclear Reactor Helium. *Materials Science and Engineering*, A104, pp. 37-51

[10] Rao, K.B.S, Schiffers, H., Schuster, H., and Nickel, H. (1988) Influence of Time and Temperature Dependent Processes on Strain Controlled Low Cycle Fatigue Behavior of Alloy 617. *Metallurgical Transactions A*, 19A, pp. 359-371.

[11] Wright, J.K., Carroll, L.J., Simpson, J.A., Wright, R.N. (2013) Low Cycle Fatigue of Alloy 617 at 850°C and 950°C. *J. of Engineering Materials and Technology,* Vol. 135.

[12] Carroll, L.J., Cabet, C., Wright, R.N. (2010) The Role of Environment on High Temperature Creep-Fatigue Behavior of Alloy 617. *ASME PVP Conf. 2010*, PVP2010-26126

[13] Carroll M.C., Carroll, L.J. (2013) Developing Dislocation Subgrain Structures and Cyclic Softening During High-Temperature Creep-Fatigue of a Nickel Alloy. *Metallurgical and Materials Transactions A,* Vol. 44A, pp. 3592-3607

[14] Lemaitre, J. Chaboche, J.L. (1990) Mechanics of Solid Materials. *Cambridge University Press*, pp. 256.

[15] Bairstow, L. (1911) The Elastic Limits of Iron and Steel under Cyclical Variations of Stress. *Philosophical Transactions of the Royal Society of London*, Series A, Vol. 210, pp. 35-55.

[16] Dugdale, D.S. (1959) Stress-Strain Cycles of Large Amplitude. *J. Mech. Phys. Solids,* Vol. 7, pp. 135-142.

[17] Landgraf, R.W., Morrow, J., Endo, T. (1969) Determination of the Cyclic Stress-Strain Curve. *Journal of Materials,* JMLSA, Vol. 4, No. 1, pp. 176-188.

[18] Chaboche, J. L., Dang Van, K., & Cordier, G. (1979). Modelization of the Strain Memory Effect on the Cyclic Hardening of 316 Stainless Steel, SMiRT'5, Div. L, Berlin, LI, 1(3).

[19] Hassan, T., Kyriakides, S. (1994) Ratcheting of Cyclically Hardening and Softening Materials, *Int'l J. of Plasticity*, Vol. 10, No. 2, pp.149-212.

[20] Morrow J. (1965) Cyclic Plastic Strain Energy and Fatigue of Metals. STP378-EB.

High Temperature Multiaxial Fatigue and Ratcheting Experimental Responses of Alloy 617

Shahriar Quayyum[1] , Mainak Sengupta[2], Gloria Choi[2], Clifford J. Lissenden[2] and Tasnim Hassan[1,*]

[1]*Department of Civil, Construction and Environmental Engineering, North Carolina State University, Raleigh, NC, USA*
[2]*Department of Engineering Science and Mechanics, The Pennsylvania State University, University Park, PA, USA*

Abstract

One of the most challenging tasks in the design development of next generation nuclear plant (NGNP) is the design of intermediate heat exchanger (IHX) which is expected to operate in the temperature range of 800-950ºC. Nickel based Alloy 617 is one of the leading candidate materials for intermediate heat exchanger (IHX) of the next generation nuclear plant (NGNP). The temperature range is in the creep regime and system start-up, operation and shut-down cycles will induce low-cycle fatigue damages in the IHX components. Moreover, the state of stress at critical locations of IHX components can be multiaxial. Hence, a detailed understanding of the creep-fatigue and ratcheting responses of the material is required for the design of IHX. In this study, a broad set of high temperature multiaxial experiments were conducted on Alloy 617 to investigate the creep-fatigue and creep-ratcheting phenomena. The results were critically evaluated to elucidate the effect of different test parameters on the multiaxial creep-fatigue and creep-ratcheting responses of the material. Experiments were conducted by prescribing different multiaxial loading histories in axial and shear directions at 25ºC, 650ºC, 850ºC and 950ºC with different strain rates and strain amplitudes. Experimental results revealed that the axial strain ratcheting and cyclic hardening/softening responses of Alloy 617 vary significantly with temperature levels, loading non-proportionality, strain rates and strain amplitudes indicating the dependence of creep-fatigue and ratcheting responses on these parameters. The examination of the Alloy 617 multiaxial experimental responses enables us to identify various modeling features that will be needed in a unified constitutive model (UCM) for simulation of the whole set of multiaxial responses developed in this study.

Keywords: High Temperature Fatigue, Ratcheting, Fatigue, Creep-Fatigue, Mutliaxial Ratcheting, Unified Constitutive Modeling

* Corresponding author, Email: thassan@ncsu.edu, Phone: 1-919-515-8123

1. Introduction

The US Department of Energy decided the high temperature gas cooled reactor (HTGR) design to be used in constructing the next generation nuclear plants (NGNPs). The HTGR will be able to provide low risk and cost effective nuclear power for electricity and hydrogen production. One of the critical components of the HTGR is the intermediate heat exchanger (IHX) which will carry most of the reactor thermal output to a secondary circuit, that will power a turbine for electricity generation. An additional heat exchanger will take approximately 10% of the thermal energy of the reactor and divert it as process heat to the hydrogen production plant (Corwin, 2006; Wright, 2006; Wright *et al.*, 2008). The anticipated operating temperature of the IHX ranges from 800-950ºC which is in the creep regime. Due to start-up, operation and shut-down cycles, the IHX will be subjected to thermo-mechanical low-cycle fatigue loading, with long hold periods at peak temperatures (within 850-950ºC), and pressure up to 8 MPa (Natesan *et al.*, 2009). Moreover, the state of stress at critical locations of IHX and other HTGR components can be multiaxial. Meeting such a strenuous demand makes the design of the IHX among the most challenging tasks of NGNP design development. In fact, the Independent Technical Review Group (ITRG) identified IHX as a high risk NGNP component (INEEL/EXT-04-01816).

The American Society of Mechanical Engineers (ASME) design code (Section III, subsection NH) currently does not include design provisions for Alloy 617 or any materials for temperatures above 760ºC. Hence, one of the primary objectives of the NGNP initiative is to conduct very high temperature testing of the IHX candidate materials in order to develop technology and tools for selection of materials for high temperature nuclear application, design code development, licensing and construction activities. Even though the HTGR design is yet to be finalized, various candidate alloys are under consideration. The primary candidate materials for the intermediate heat exchanger (IHX) of the NGNP are the Alloys 617 and 230. Because of the available material database, experience base, and available product forms, Alloy 617 is the top choice as the IHX material. However, not much data is available in the literature on the experimental response of Alloy 617 at high temperature; especially no data is available on the multiaxial experimental response of Alloy 617. In addition, no unified constitutive model ever demonstrated in the literature for simulating the viscoplastic behavior of Alloy 617 at high temperature. Hence, NGNP IHX materials R&D Plan (INL-PLN-2804) recommended a long list of experiments on alloy 617 for developing design curves and a unified constitutive model (UCM) toward overcoming the challenge of IHX design using Alloy 617.

Different researchers investigated the influence of different test parameters such as temperature, strain rate, strain range and hold time at different environmental conditions by performing uniaxial low-cycle fatigue, creep and creep-fatigue tests on Alloy 617. Significant data applicable to the Gen IV systems were generated from investigations by the HTGR programs at the Oak Ridge National Laboratory and General Electric Co. in the United States (McCoy and King, 1985; Baldwin *et al.*, 1986). Burke and Beck (1984), Breitling *et al.* (1988), Rao *et al.* (1988a, 1988b), Nagato *et al.* (1989), Corum and Blass (1991), Ren *et al.* (2006), Rahman *et al.* (2009), Wright *et al.* (2012), Chen *et al.* (2013) and Maier *et al.* (2011, 2013) performed fully reversed axial strain controlled low-cycle fatigue (LCF) and creep-fatigue tests on Alloy 617 at higher temperatures and different loading rates. It was observed that with increase in temperature, the peak stress and the fatigue life decreased. Softening of material was observed at higher temperatures after few initial cycles of hardening. Unlike the response at

lower temperatures, Alloy 617 exhibited high sensitivity to loading rate at very high temperatures. The number of cycles to macrocrack initiation decreased with decreasing strain rates and with increasing temperature. Cyclic hardening and softening behavior of the alloy was found to depend on temperature and strain rate conditions employed. However, the influence of the strain rate on the creep-fatigue lifetime was not conclusive (Rao *et al.*, 1988a, 1988b; Breitling *et al.*, 1988; Nagato *et al.*, 1989).

The effect of hold time on the fatigue life of Alloy 617 under uniaxial loading was investigated by Totemeier and Tian (2007), Carroll *et al.*, (2010, 2011), Cabet *et al.*, (2011), Wright *et al.*, (2012) and it was concluded that irrespective of the position of hold at peak strain in a cycle, hold time always reduced fatigue life compared to continuous-cycling tests. Previous work has also desmonstrated for Alloy 617 that a hold time during the tensile portion of the fatigue cycle was more damaging than compressive holds or both a tensile and compressive hold (Meurer *et al*., 1984; Tsuji and Condo, 1987; Rao *et al.*, 1988a, 1988b; Breitling *et al.*, 1988). This was also reconfirmed recently by Chen *et al.* (2013) who performed LCF and creep–fatigue testing of Alloy 617 and Haynes 230 in the air at 850ºC with different strain ranges and hold time at maximum tensile strain for 3, 10 or 30 min. Compared to the LCF results, the cycles to failure for both materials decreased under creep–fatigue test conditions. Longer hold time at maximum tensile strain caused a further reduction in the creep–fatigue life of both materials. Moreover, Totemeier and Tian (2007) and Wright *et al.* (2012) observed decrease in the number of cycles to crack initiation with increase in the strain range.

From the literature it is evident that the LCF, creep and the creep-fatigue damage mechanism of Alloy 617 are sensitive to temperature, strain rate and strain range. Moreover, no literature was found on the multiaxial creep-fatigue and creep-ratcheting failure mechanism of Alloy 617. However, multiaxial fatigue and creep data are desirable for providing the basis for the development of constitutive equations, and are used to confirm the adequacy of application of the von-Mises effective strain and other approaches for fatigue analysis (Ren and Swindeman, 2009). The study reported herein undertakes a broad set of multiaxial creep-fatigue and ratcheting experiments on Alloy 617 at very high temperatures thereby mimic the conditions of IHX critical locations. Experiments were conducted prescribing different multiaxial loading histories at 25ºC, 650ºC, 850ºC and 950ºC in the axial and shear, stress and strain space with different strain rates and strain amplitudes. These multiaxial experimental responses of Alloy 617 were critically evaluated to understand the influence of multiaxial loading, interactions between creep-fatigue-ratcheting failure responses, and effects of loading rates and strain amplitudes. The multiaxial experimental responses will provide data for developoing the ASME-NH Code provisions for Alloy 617 and help in developing an experimentally validated UCM. The experimental responses will also help in ensuring the robustness of the UCM through simulating a broad set of multiaxial creep-fatigue-ratcheting responses. Such a UCM will help engineers adopt the design by inelastic analysis method for designing critical NGNP components. Multiaxial experiments performed and the experimental responses are elaborated in the following.

2. Experimental Study

2.1. Test setup

Many researchers have worked on elevated temperature material coupon testing to demonstrate complexity and different techniques for carrying out these tests. The most complete experimental description has been provided by Ellis and Bartolotta (1997), who have advocated the use of an adjustable coil fixture for induction heating. Such a fixture is convenient to use and provides access to the specimen surface. This facilitates the measurement of strain with the help of a high-temperature extensometer. An induction heater is used for heating the specimen to the test temperature. Lissenden *et al.* (2000) have studied the axial-torsional load effects on Haynes 188 at 650ºC and have explained the experimental procedure and instruments in good detail. Previous researchers like Chen *et al.* (2005), Totemeier and Tian (2007) who have worked on elevated temperature testing have used similar kinds of testing equipment to conduct uniaxial tests. Therefore, due to its widespread acceptability, an induction heating system with flexible coil fixture and water cooled grips has been adopted in this research.

Alloy 617 specimens used in testing were machined in the form of thin-walled tubular specimens. The specimens were machined from a 38 mm thick annealed plate with the axis of the specimen aligned in the rolling direction. The chemical composition of the alloy is provided in Table 1. The gage section has an external diameter of 21 mm and an internal diameter of 18 mm and has a total length of 305 mm (see Fig. 1 and Fig. 2a for more details). The end sections were 30 mm in diameter so that they could be gripped in the hydraulic collet grips without crushing the tube. Multiaxial experiments were conducted using a universal axial-torsion hydraulic testing system with ±245kN axial force and ±2830 N-m torque capacity. The specimen was held in water cooled hydraulic collet grips in the vertical position. The axial and shear strains were measured using high temperature biaxial extensometer. The extensometer was also water cooled. A 7.5 KW radio-frequency induction heater was used to achieve the test temperatures of 650ºC, 850ºC and 950ºC. The induction heater sends out a high-frequency current to three coils that were mounted on an adjustable-positioning-mechanism rig. These coils induced eddy currents on the specimen surface and resistance in the specimen created joule heating. Thermocouples were spot welded to the specimen to measure and control the test temperature. The temperature gradient was kept within 1% of the desired temperature as described in ASTM E606 (1980). Fig. 2b shows the experimental setup with specimen gripped and extensometer mounted.

Table 1 Chemical composition of Alloy 617 in wt. % [Carroll *et al.*, 2011]

Ni	Cr	Co	Mo	C	Fe	Al	Ti	Si	Mn	Cu
Balance	21.9	11.4	9.3	0.08	1.7	1.0	0.3	0.1	0.1	0.04

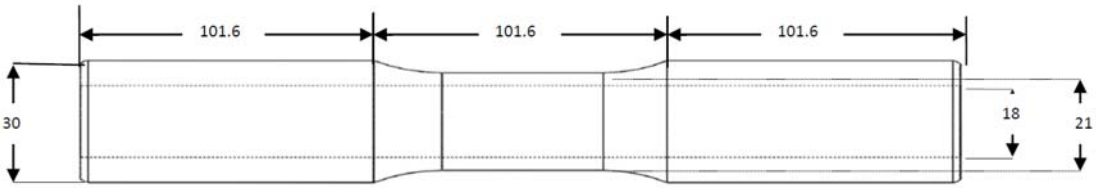

Fig. 1 Schematic of the specimen with dimensions in mm.

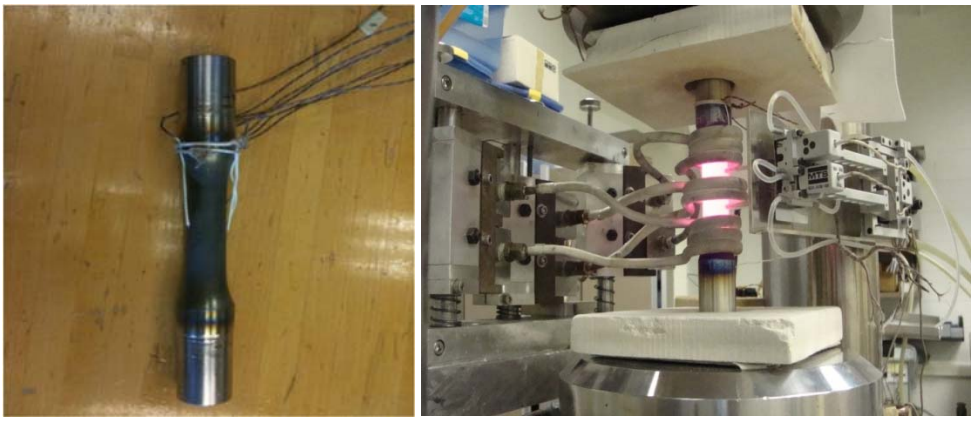

(a) (b)

Fig. 2 (a) Specimen, and (b) experimental setup.

2.2. Test Type and Loading Histories

To investigate the multiaxial creep-fatigue and creep-ratcheting interaction of Alloy 617, hybrid strain controlled and stress controlled loading histories were prescribed on the specimens. Thirty two experiments were performed for investigating the effect of temperature, strain rate, strain amplitude and loading history on the multiaxial behavior of Alloy 617. These thirty two experiments were conducted using two different strain rates (0.04%/s and 0.1%/s) and multiple strain amplitudes (0.2%, 0.3% and 0.4%) at 25ºC, 650ºC, 850ºC and 950ºC. In the discussion, strain amplitude refers to the equivalent strain amplitude in case of the multiaxial loading. To study the effect of loading history, three different types of loading histories MR1, MR2 and MOP were considered as shown in Fig. 3. The MR1 test involved applying a steady axial stress and symmetric shear strain cycles (Fig. 3a). The cyclic shear strain could create cyclic hardening or softening under a small degree of loading non-proportionality. Due to inelastic interaction between the steady axial stress and shear strain, ratcheting of axial strain occurs (see Section 3.1 for more details). The MR2 loading history involved applying a cyclic axial stress with a mean stress, dwell periods at the positive and negative peaks, and symmetric shear strain cycles along a bow-tie path (Fig. 3b). The bow-tie loading path mimics stress history of piping under cyclic bending (Corona *et al.*, 1996). The MR2 loading path also results in axial strain ratcheting (see Section 3.2 for details). Since the axial stress is cyclic, fatigue damage is more detrimental under MR2 than MR1. The cyclic shear strain could result in cyclic hardening or softening under intermediate degree of loading non-proportionality which in turn influences axial strain ratcheting rate (Hassan *et al.*, 2008).

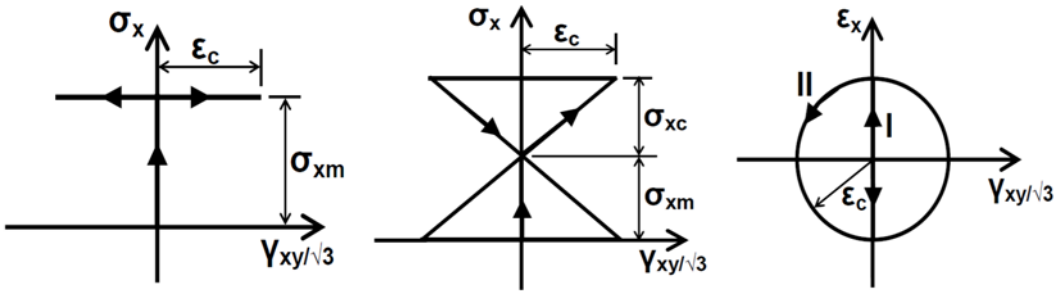

(a) MR1 (b) MR2 (c) MOP

Fig. 3 (a) MR1, (b) MR2 and (c) MOP loading histories prescribed in the multiaxial experiments on Alloy 617 specimens.

The MOP loading path in Fig. 3c involved 100 axial strain cycles (Path I) followed by 100, 90º out-of-phase cycles (path II) followed by 100 more axial strain cycles (path I). These tests demonstrate cyclic hardening-softening behavior under highest degree of loading non-proportionality (Lamba and Sidebottom, 1978; Hassan and Kyriakides, 1994). Data from these tests would be needed for determination of the unified constitutive model multiaxial or non-proportional parameters (see Section 3.3 for more details). Table 2 shows the test matrix of the multiaxial experiments performed on Alloy 617 using these three loading paths.

Table 2 Test matrix of multiaxial experiments

Load Path	No. of Specimens	Temp. (ºC)	Strain Rate (%/s)	Strain Amp. (%)
MR1	12	25,650, 850, 950	0.04, 0.1	0.2, 0.3,0.4
MR2	10	25, 650, 850, 950	0.04, 0.1	0.18, 0.4
MOP	10	25, 650, 850, 950	0.04, 0.1	0.2, 0.3

3. Multiaxial Experimental Results

The MR1 and MR2 experiments were conducted by prescribing different temperatures, strain amplitudes and strain rates under varying degree of loading non-proportionality to investigate the ratcheting-creep-fatigue life, ratcheting strain rates and limits, mean-stress effect, cyclic hardening-softening and failure modes of Alloy 617. The creep strain, axial strain ratcheting and cyclic hardening-softening behavior of the material would be of particular interest. MOP experiments were primarily performed to study the cyclic hardening-softening of Alloy 617 under highest degree of loading non-proportionality and to determine the UCM parameters. The loading parameters in the MR1 and MR2 experiments and resulting fatigue life and failure modes are summarized in Table 3. The experimental responses of MR1, MR2 and MOP tests and the effects of various test parameters on the multiaxial creep-fatigue and ratcheting response of Alloy 617 are discussed in the subsequent sections.

Table 3 Summary of MR1 and MR2 experiments

Test	T (ºC)	$\dot{\gamma}$ (%/s)	$\gamma_{xy}/\sqrt{3}$ (%)	N_f	t_f (min)	Failure Mode
MR1	25	0.1	0.2	10050	1340	NF*
	650	0.1	0.2	10010	1334	NF
	850	0.04	0.2	3230	1077	Crack
	850	0.1	0.2	3770	502	Crack
	850	0.1	0.3	1794	341	Crack
	850	0.04	0.4	955	634	Crack
	850	0.1	0.4	1052	281	Crack
	950	0.04	0.2	1300	434	Necking
	950	0.1	0.2	1742	232	Crack
	950	0.1	0.3	799	160	LD*
	950	0.04	0.4	235	157	LD
	950	0.1	0.4	262	70	Necking
MR2	25	0.1	0.18	11273	2706	NF
	650	0.1	0.18	10010	2402	NF
	850	0.04	0.18	1968	1181	Crack
	850	0.1	0.18	2247	540	Crack
	850	0.04	0.4	646	431	Crack
	850	0.1	0.4	492	130	NF
	950	0.04	0.18	274	164	LD
	950	0.1	0.18	1139	273	Crack
	950	0.04	0.4	121	81	NF
	950	0.1	0.4	207	55	NF

*LD – localized deformation, NF – no failure

3.1. MR1 Tests

The MR1 test involved applying a steady axial stress and a cyclic shear strain on the specimen as shown in Fig. 3a. The steady axial stress resulted in creep strain in the axial direction. The cyclic shear strain could create cyclic hardening or softening of the shear stress. Due to the plastic coupling, it could also lead to axial strain ratcheting. Axial strain accumulation with number of cycles is of great interest because it will play an important role in the ultimate life of the specimen. The strain-controlled, shear stress-strain hysteresis loops will provide additional information about the material behavior at elevated temperatures. Ratcheting will also depend on the mean stress and the loading proportionality of the test. The MR1 test has a lower degree of loading non-proportionality since the axial stress is held constant while the shear strain is cycled. Twelve experiments were conducted for the MR1 kind of tests. Five experiments were conducted at 850ºC and five experiments were conducted at 950ºC with two different strain rates of 0.04%/s and 0.1%/s and three different stain amplitudes of 0.2%, 0.3% and 0.4%. Two experiments were also conducted at 25ºC and 650ºC with.1%/s strain rate to compare the material behavior at higher and lower temperatures. The fast and slow strain rates help us understand the effect of loading rate on the material behavior. In all the experiments, the axial stress was held constant at 12 MPa. The multiaxial responses that are of interest for MR1experiment are shown in Fig. 4 for one experiment conducted at 850ºC.

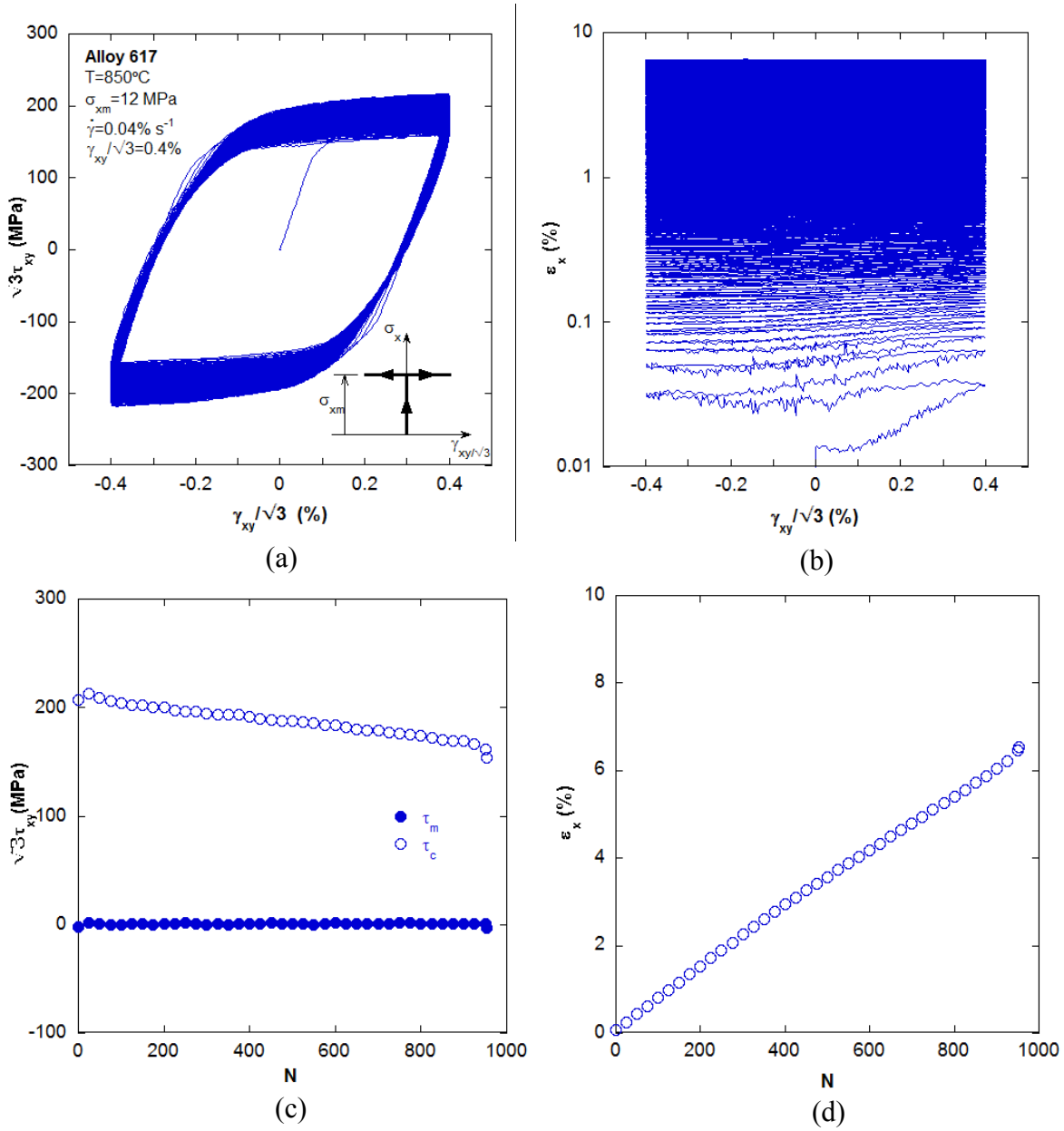

Fig. 4 Experimental response of Alloy 617 for MR1 experiment at 850ºC with 0.04%/s strain rate and 0.4% strain amplitude. (a) Equivalent stress-strain hysteresis loops; (b) Axial strain plotted against equivalent shear strain; (c) Equivalent stress amplitude and mean plotted against number of loading cycles; (d) Maximum axial strain in each cycle plotted against number of loading cycles.

The equivalent stress-strain hysteresis loops as shown in Fig. 4a shows cyclic hardening for few initial cycles followed by cyclic softening of the material, whereas Fig. 4b shows accumulation of axial strain with progressive loading cycles (axial strain ratcheting). The cyclic hardening/softening behavior can be more clearly observed when equivalent stress amplitude and mean are plotted against number of loading cycles as shown in Fig. 4c. It was evident that the mean stress remained constant during cycling whereas the equivalent stress amplitude showed

initial hardening followed by softening. Similarly the axial strain ratcheting is clearly visible in Fig. 4d, where maximum axial strain in each cycle is plotted against number of loading cycles. In the subsequent sections, the comparison between different experimental responses and the effects of different test parameters will be discussed using the plots similar to Fig. 4c and Fig. 4d. However, it is very interesting to see that although the there was no axial stress cycling, the axial strain continued to increase up to failure. This is because of the presence of the constant axial stress which might be inducing creep strain in the axial direction.

3.2. MR2 Tests

The MR2 test involved applying a cyclic axial stress with mean stress and symmetric hold times as well as symmetric shear strain cycles on the specimen. This kind of test path is called bow-tie path as shown in Fig. 3b. Unlike the MR1 test where the steady axial stress resulted in creep, the cyclic axial stress with a non-zero mean stress in MR2 test resulted in ratcheting. Since the axial load was cyclic, fatigue damage could be more significant in these tests compared to MR1 tests. The cyclic shear strain could result in cyclic hardening or softening and also lead to axial strain ratcheting. The accumulation in axial strain due to ratcheting could decide the ultimate life of the specimen. The effect of temperature on the viscoplastic material behavior can be understood from the plastic strain range of the shear stress-shear strain hysteresis plots. The MR2 test has a higher degree of non-proportional loading as compared to the MR1 tests due to the bow-tie test path. The effect of higher-degree of non-proportional loading on the ratcheting behavior will be of great interest. Ten experiments were conducted for the MR2 kind of tests. Four experiments were conducted at 850ºC and four experiments were conducted at 950ºC with two different strain rates of 0.04%/s and 0.1%/s and two different stain amplitudes of 0.18% and 0.4%. Two experiments were also conducted at 25ºC and 650ºC with 0.1%/s strain rate to compare the material behavior at higher and lower temperatures. The fast and slow strain rates help us understand the effect of loading rate on the material behavior. The equivalent strain amplitude for four MR2 tests was 0.18% (compared to 0.2% for MR1 tests) to compensate for the increase in the axial stress range and so that the equivalent stresses are comparable with the MR1 type of tests. The axial stress was cycled from a minimum value of 0 MPa to maximum value of 24 MPa with a mean of 12 MPa. Fig. 5 shows multiaxial experimental responses of Alloy 617 for one MR2 test performed at 950ºC. These plots are similar to Fig. 4 where cyclic hardening/softening and axial strain accumulation are of particular interest. The equivalent stress-strain hysteresis loops (Fig. 5a) and the equivalent stress amplitude (Fig. 5c) plots show gradual softening of the material at 950ºC. The material also showed increasing axial strain ratcheting with number of loading cycles as can be seen in Fig. 5b and Fig. 5d. This is similar to what was observed in Fig. 4.

3.3. MOP Tests

It is well known that in many materials, non-proportional multiaxial cyclic loading can induce significantly more hardening than proportional cyclic histories (Lamba and Sidebottom, 1978; Sliwowski, 1979; Kanazawa *et al.*, 1979; Tanaka *et al.*, 1985; McDowell, 1985). Thus, the cyclic hardening/softening characteristics of a material cannot be captured solely from uniaxial experiments (Hassan and Kyriakides, 1994). In this study, the MOP loading path incorporated the highest degree of non-proportionality (Fig. 3c) through the 90º out-of-phase axial and shear strain

cycles (circular load path, Path II). The experimental response of Alloy 617 for one MOP experiment performed at 850ºC is shown in Fig. 6. The stress and strain response of Alloy 617 for path I, II and III are shown in Fig. 6a, b and c, respectively.

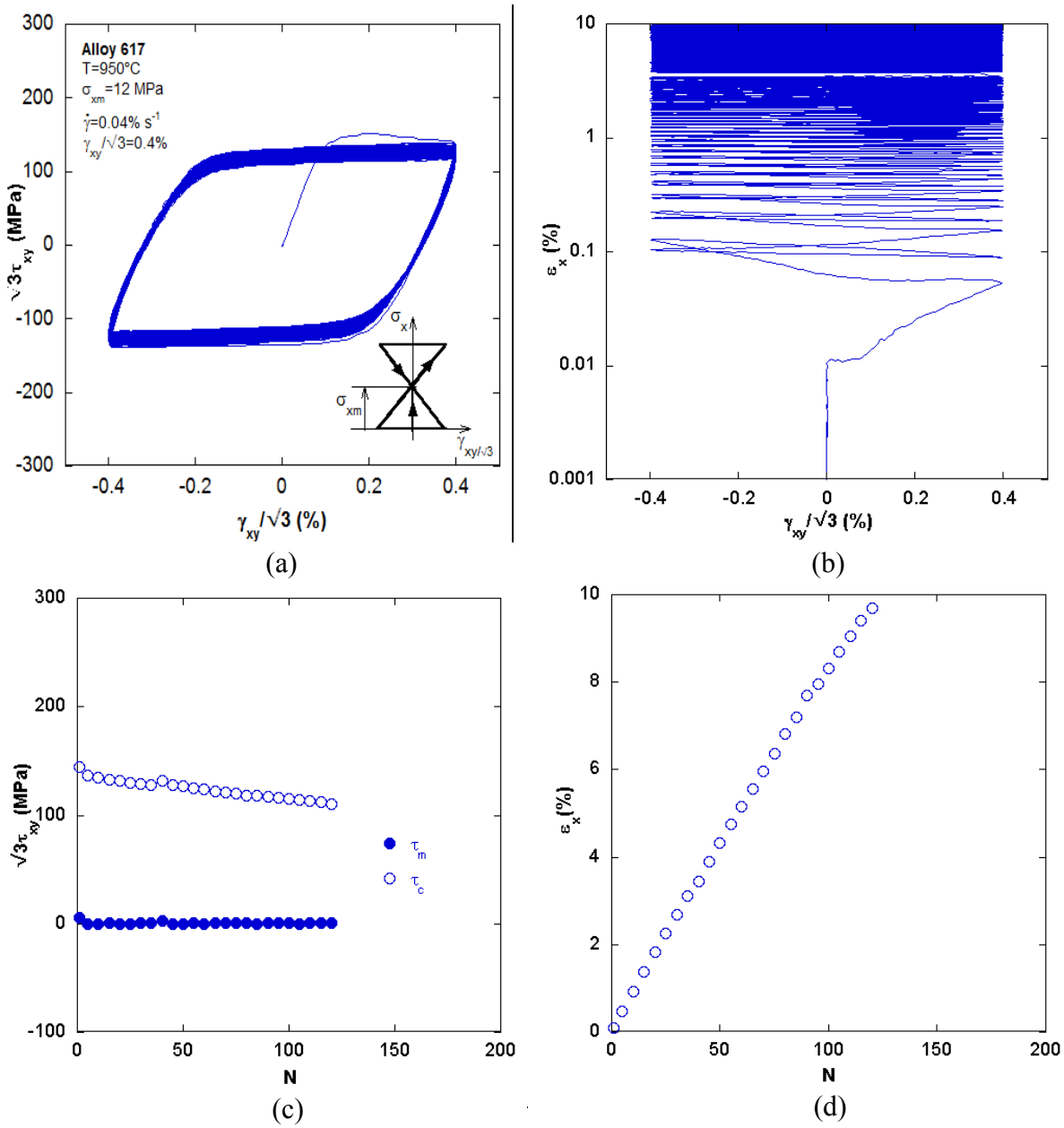

Fig. 5 Experimental response of Alloy 617 for MR2 experiment at 950ºC with 0.04%/s strain rate and 0.4% strain amplitude. (a) Equivalent stress-strain hysteresis loops; (b) Axial strain plotted against equivalent shear strain; (c) Equivalent stress amplitude and mean plotted against number of loading cycles; (d) Maximum axial strain in each cycle plotted against number of loading cycles.

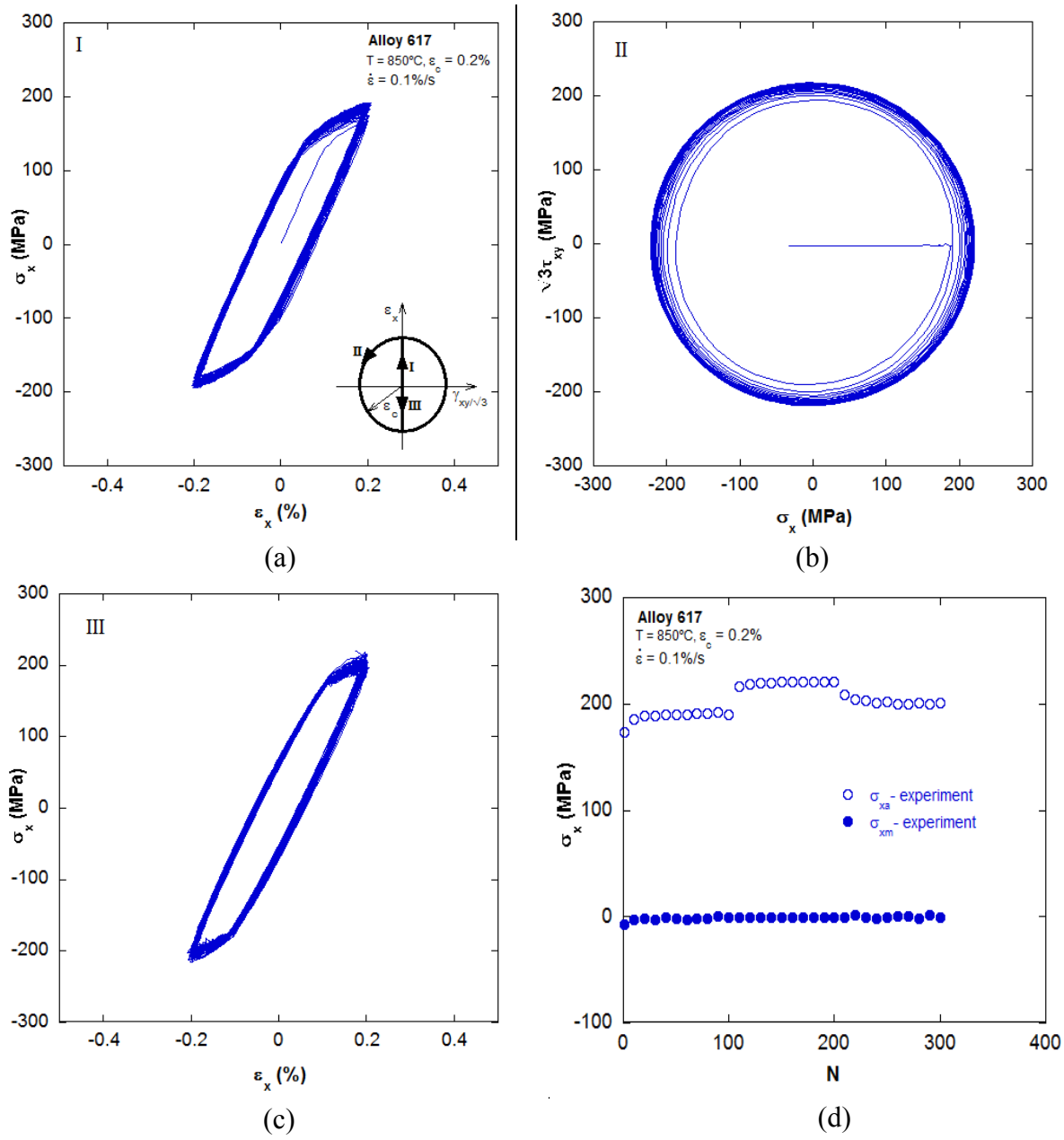

Fig. 6 Experimental response of Alloy 617 for MOP experiment at 850ºC with 0.1%/s strain rate and 0.2% strain amplitude. (a) Axial stress-strain response for path I; (b) Equivalent stress response for path II; (c) Axial stress-strain response for path III; (d) Axial stress amplitude and mean plotted against number of loading cycles; (e) Decrease of shear stress during proportional cycles for path III.

Axial stress amplitudes from the MOP load history is plotted in Fig. 6d, where a marked discontinuous increase in the axial stress amplitude was observed immediately after the axial strain cycle (path I) was changed to 90º out-of-phase cycle (path II) (Tanaka *et al.*, 1985; Hassan and Kyriakides, 1994; Krishna *et al.*, 2009). This cross effect can be accounted for by a large resistance brought about by a stable dislocation structure formed in the preceding proportional cycles to the dislocation movement in the subsequent cycles in another direction (Tanaka *et al.*,

1985). Conversely, when path II cycle is changed to axial strain cycle, abrupt change from highest non-proportional load path to low non-proportional path (because of small residual shear stress as shown in Fig. 6e, abrupt softening of Alloy 617 is observed at both 850ºC and 950ºC. However, there was no significant hardening observed during the 90º out-of-phase cycles (Fig. 6d) at 850ºC. During developing a unified constitutive model, it is very important to capture the stress jump when proportional cycles are changed to non-proportional cycles and subsequent stress drop when non-proportional cycles are changed to proportional cycles. Data from MOP tests would help in determining the unified constitutive model non-proportional or multiaxial parameter for capturing this stress jump and drop.

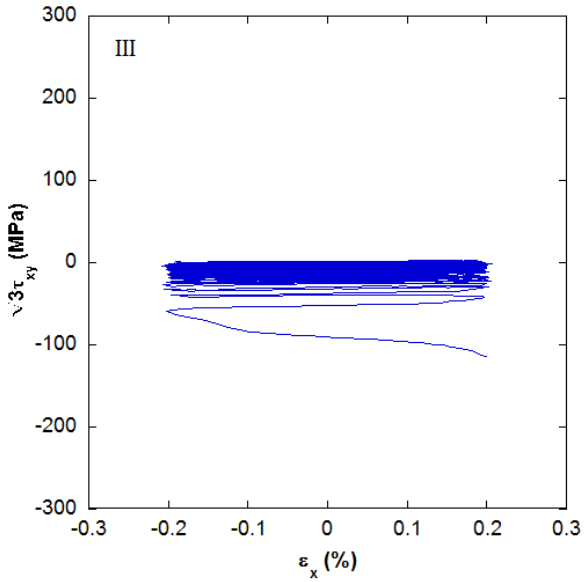

(e)

Fig. 6 continued.

3.4. Effect of Temperature

To maintain its economic advantage over early generation reactor systems, the HTGR of NGNP uses helium at temperatures higher than 900ºC and pressures up to 8 MPa for a design life of 60 years (Ren and Swindeman, 2009; Charit and Murty, 2010). Conceptual design requires an outlet temperature of greater than 850ºC to efficiently generate hydrogen, with a maximum expected temperature of 950ºC (Carroll *et al.*, 2010, 2011; Wright *et al.*, 2012). Hence, in this study, the multiaxial experiments were conducted at 850ºC and 950ºC to characterize the material behavior in this temperature range which is in the creep regime for Alloy 617. Multiaxial experiments were also conducted at 25ºC and 650ºC to compare the material behavior at higher and lower temperatures. The material showed ominously different behavior at higher and lower temperatures. Also, at higher temperature range, the material showed completely different behavior at 850ºC and 950ºC. Fig. 7 shows equivalent stress amplitudes from MR1 and MR2 loading experiments plotted against the number of loading cycles for different strain rates and strain amplitudes. It was observed that irrespective of strain rate, strain amplitude and loading path, at 850ºC, the material showed cyclic hardening for the initial few cycles followed by cyclic softening, whereas at 950ºC, the material showed gradual softening.

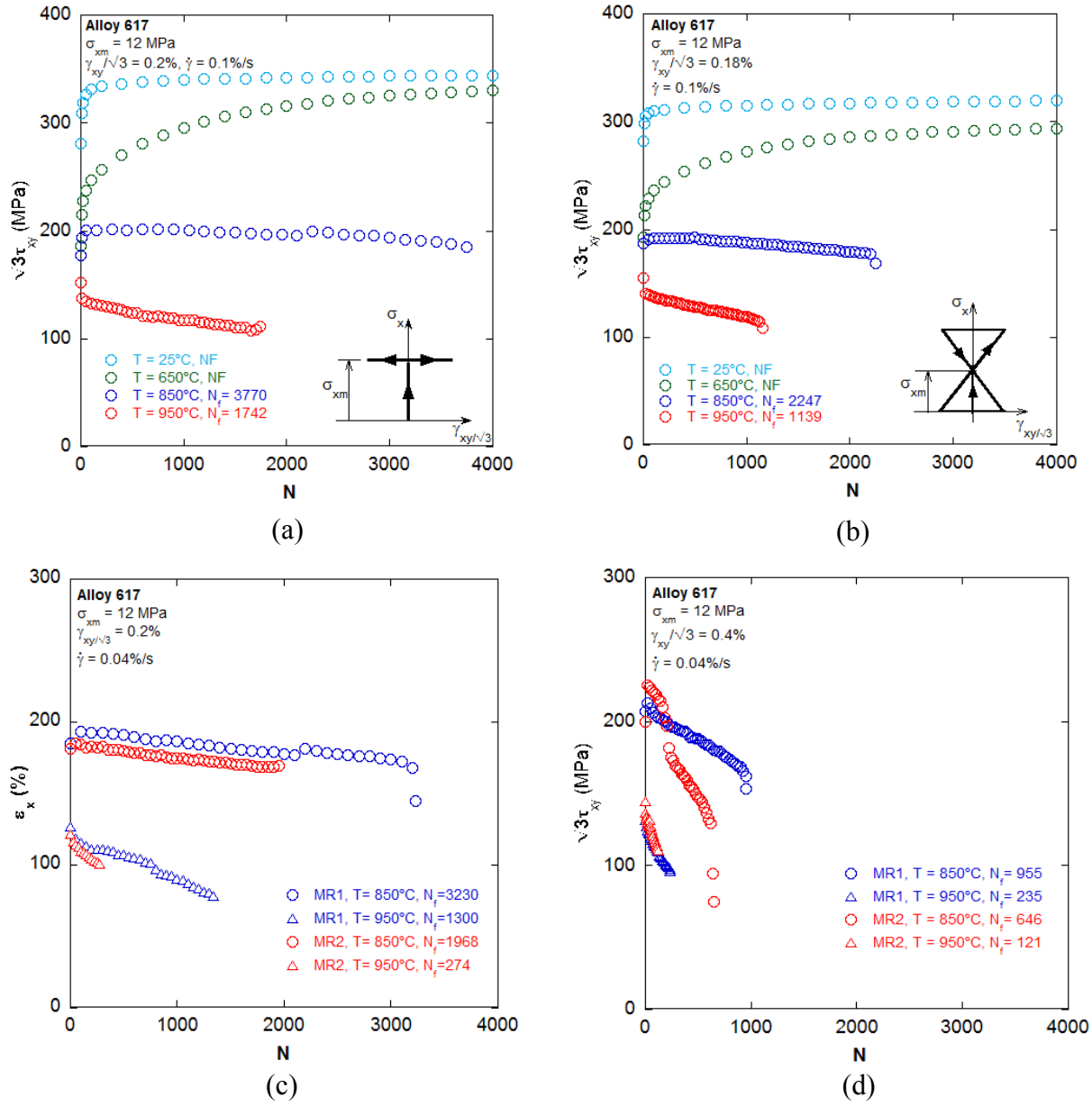

Fig. 7 Equivalent stress amplitude plotted against the number of loading cycles for MR1 and MR2 experiments at different temperatures. (a) MR1 tests at 0.1%/s strain rate with 0.2% strain amplitude; (b) MR2 tests at 0.1%/s strain rate with 0.18% strain amplitude; (c) MR1 and MR2 tests at 0.04%/s strain rate with 0.2% strain amplitude; (d) MR1 and MR2 tests at 0.04%/s strain rate with 0.4% strain amplitude.

Similar response was observed by Burke and Beck (1984), Rao *et al.* (1988a, 1988b) and Chen *et al.* (2013) from uniaxial fatigue experiments on Alloy 617 at high temperatures. They attributed the initial cyclic hardening at 850ºC to the cumulative effects of dislocation generation with their mutual interaction and to the immobilization of dislocations by fine scale carbide precipitation. Initially, the dislocation density was low, and because of repeated cyclic deformation, the dislocation slip and multiplication occurred rapidly, causing strain hardening. At some point, the newly formed dislocation structure stabilized under the magnitude of cyclic

strain imposed. The subsequent cyclic softening at 850ºC was attributed to the dislocation recovery process occurring during persistent strain cycling. The cyclic softening at 950ºC was attributed to dislocation annihilation and rearrangement into a configuration which offered less resistance to cyclic deformation (Rao *et al.*, 1988a). It is interesting to note in Fig. 7 that the equivalent stress amplitude did not stabilize to a steady state value, instead keep decreasing with increasing cycles at both 850ºC and 950ºC.

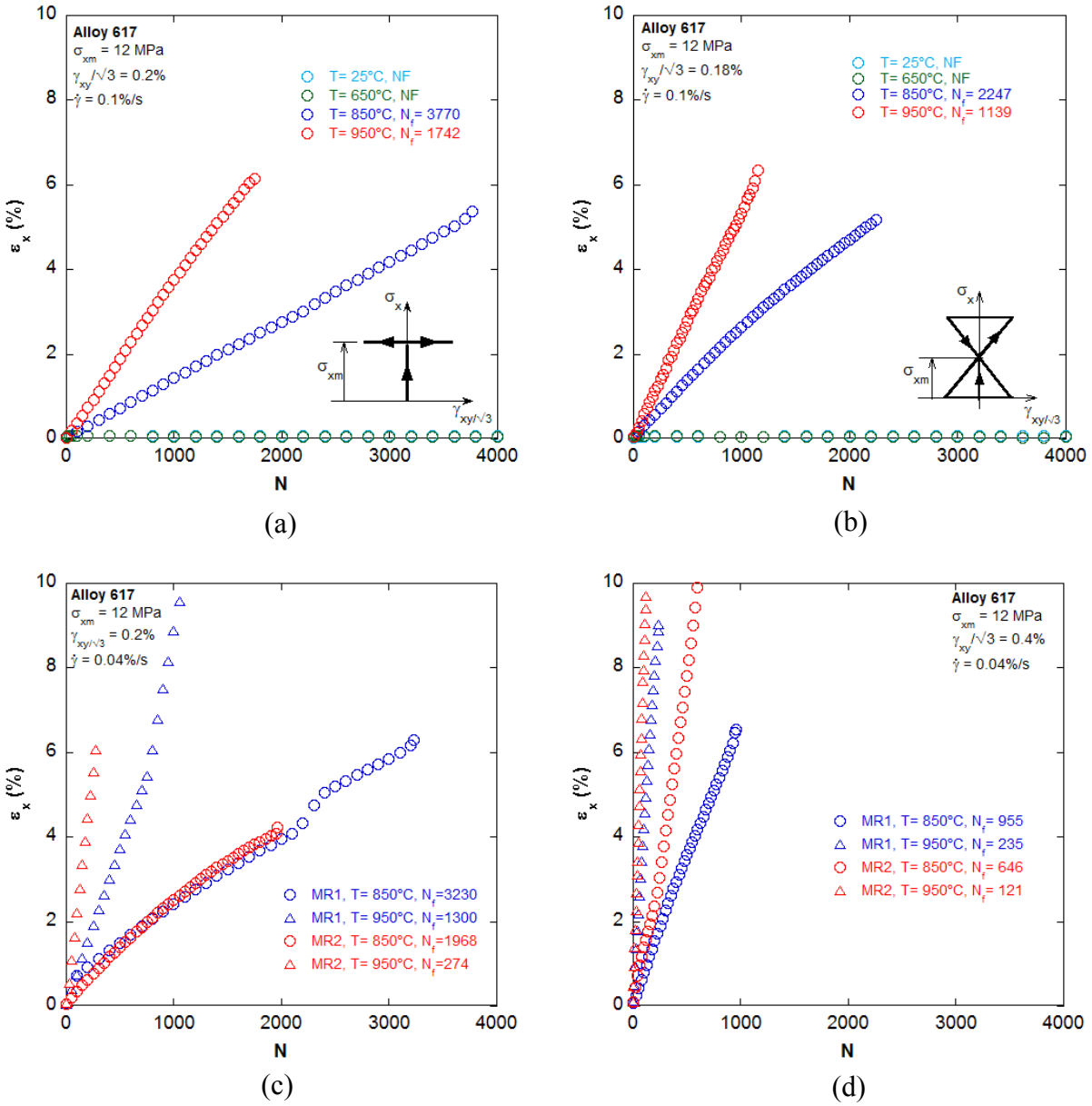

Fig. 8 Maximum axial strain in each cycle as a function of number of cycles in MR1 and MR2 experiments showing ratcheting rates. (a) MR1 tests at 0.1%/s strain rate with 0.2% strain amplitude; (b) MR2 tests at 0.1%/s strain rate with 0.18% strain amplitude; (c) MR1 and MR2 tests at 0.04%/s strain rate with 0.2% strain amplitude; (d) MR1 and MR2 tests at 0.04%/s strain rate with 0.4% strain amplitude.

On the contrary, at 25ºC the material showed hardening for few initial cycles and then it reached a steady state of stress, whereas at 650ºC, the material was continuously hardening without showing any steady state stress up to 4000 cycles. It was also interesting to note that the material did not fail at both 25ºC and 650ºC and hence, the tests were stopped manually at 10000 cycles for both the experiments. It was also observed in Fig. 7 that the equivalent stress amplitude as well as the fatigue life of Alloy 617 was lower at 950ºC compared to 850ºC regardless of the strain rate and strain amplitude. The fatigue life reduced by a factor of more than two when the temperature was increased from 850ºC to 950ºC. This reduction in fatigue life might be influenced by the increased axial strain ratcheting rate with increase in temperature as shown in Fig. 8. There was a sharp increase in the axial strain ratcheting rate as the experiment temperature changed from 850ºC to 950ºC. On the other hand, the ratcheting rate was insignificant at 25ºC and 650ºC, as a result of which the material did not fail at these temperatures. The effect of temperature on the viscoplastic material behavior can be observed from the elastic and plastic strain amplitude of the equivalent stress-strain hysteresis loops in Fig. 9, where the first cycle equivalent hysteresis loops from MR1 and MR2 experiments are plotted. It was evident that as the temperature increased there was an increase in the hysteresis loop width which indicated increase in the plastic strain amplitude. Especially, at 950ºC, the hysteresis loop width was larger than that at 850ºC, which indicated larger plastic strain amplitude at 950ºC. This in turn increased the axial strain ratcheting at higher temperature which eventually reduced fatigue life. It was also noted from the hysteresis loop plots of Fig. 9 that with increase in temperature, the elastic response of the material decreased. At 950ºC, the material showed almost no elastic response.

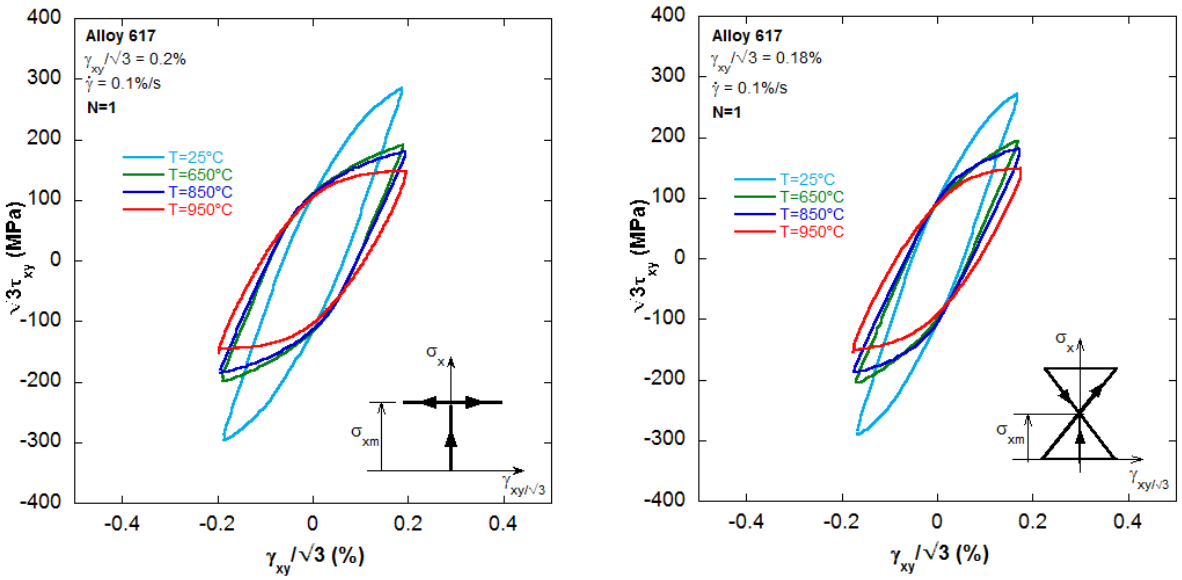

Fig. 9 Equivalent stress-strain hysteresis loops from the first loading cycle at different temperatures. (a) MR1 tests with 0.2% strain amplitude; (b) MR2 tests with 0.18% strain amplitude.

The effect of temperature on the MOP experiments is shown in Fig. 10, where the axial stress amplitude is plotted as a function of number of loading cycles for 0.1%/s strain rate and 0.3%

strain amplitude. It showed similar trend that was observed for MR1 and MR2 experiments. At 25ºC and 650ºC, the material showed cyclic hardening, whereas at 850ºC, the material showed initial cyclic hardening followed by cyclic softening, and at 950ºC the material showed continuous cyclic softening. Also, the axial stress amplitude increased with decreasing temperature. It is interesting to note that during the 90ºout-of-phase cycles, the material did not show any significant cyclic hardening/softening only at 850ºC, but it showed cyclic hardening for both at 25ºC and 650ºC and cyclic softening at 950ºC. Another interesting thing to note here that at 25ºC and 650ºC, the stress did not drop when the non-proportional cycles (path II) were changed to proportional cycles (path III). This might be related to the formation of different dislocation structures at different temperatures during non-proportional cycles.

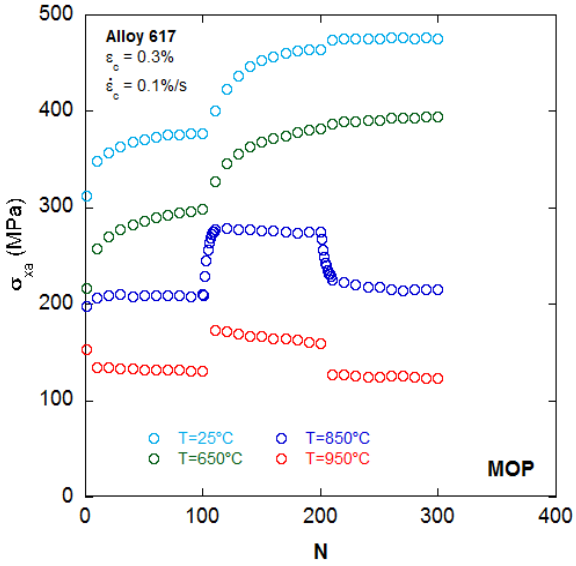

Fig. 10 Axial stress amplitude plotted as a function of number of loading cycles for MOP experiments performed at different temperatures with 0.1%/s strain rate and 0.3% strain amplitude.

3.5. Effect of Loading History

Fig. 7c, Fig. 7d and Fig. 11 illustrated comparison of the equivalent stress amplitude responses of Alloy 617 for MR1 and MR2 experiments at different temperatures up to failure, whereas Fig. 13 shows equivalent stress amplitude comparison for MR1, MR2 and MOP experiments for first 300 loading cycles. The equivalent stress amplitude of MR2 tests in all of the experiments was equal or less than the equivalent stress amplitude of MR1 experiments irrespective of temperature, strain rate and strain amplitude, except for experiment performed at 950ºC at 0.1%/s strain rate with 0.4% strain amplitude where MR2 test showed higher equivalent stress amplitude than that of MR1 test (Fig. 11b). In all the experiments, the 90º out-of-phase cycles produced the largest stress amplitude compared to MR1 and MR2 tests (Fig. 13) since it incorporated the highest degree of loading non-proportionality. Although MR2 tests had higher degree of loading non-proportionality compared to MR1 tests, it showed lower equivalent stress amplitude. This might have happened because of the presence of a hold at the peak axial stress for MR2 tests. However, the material showed similar trend in the cyclic hardening/softening behavior for both MR1 and MR2 tests. It can be observed that the life of Alloy 617 before failure

decreased with increase in the degree of loading non-proportionality as can be seen in Fig. 7c, Fig. 7d and Fig. 11 where the fatigue life was always lower for MR2 tests compared to MR1 tests. Under MR2 tests, Alloy 617 encountered axial stress fluctuation in presence of a nonzero axial mean stress which induced higher rate of axial strain ratcheting than under MR1 tests as shown in Fig. 8c, Fig. 8d and Fig. 12.

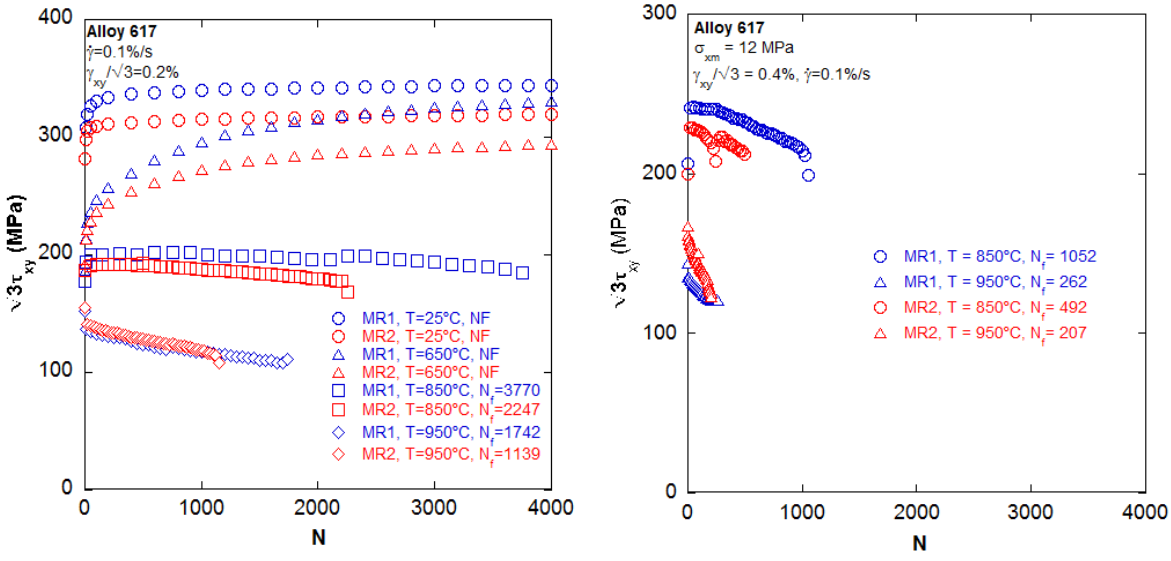

(a) (b)

Fig. 11 Equivalent stress amplitude plotted against number of loading cycles for MR1 and MR2 experiments performed at different temperatures. (a) 0.1%/s strain rate, 0.2% strain amplitude; (b) 0.1%/s strain rate, 0.4% strain amplitude.

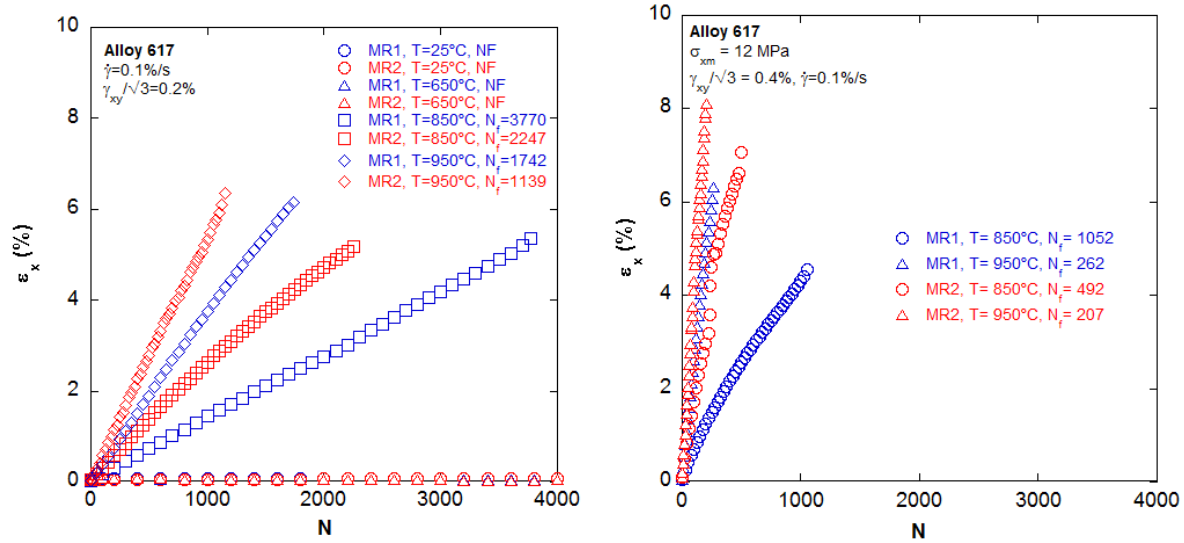

(a) (b)

Fig. 12 Axial strain accumulation with number of loading cycles for MR1 and MR2 experiments performed at different temperatures. (a) 0.1%/s strain rate with 0.2% strain amplitude; (b) 0.1%/s strain rate with 0.4% strain amplitude.

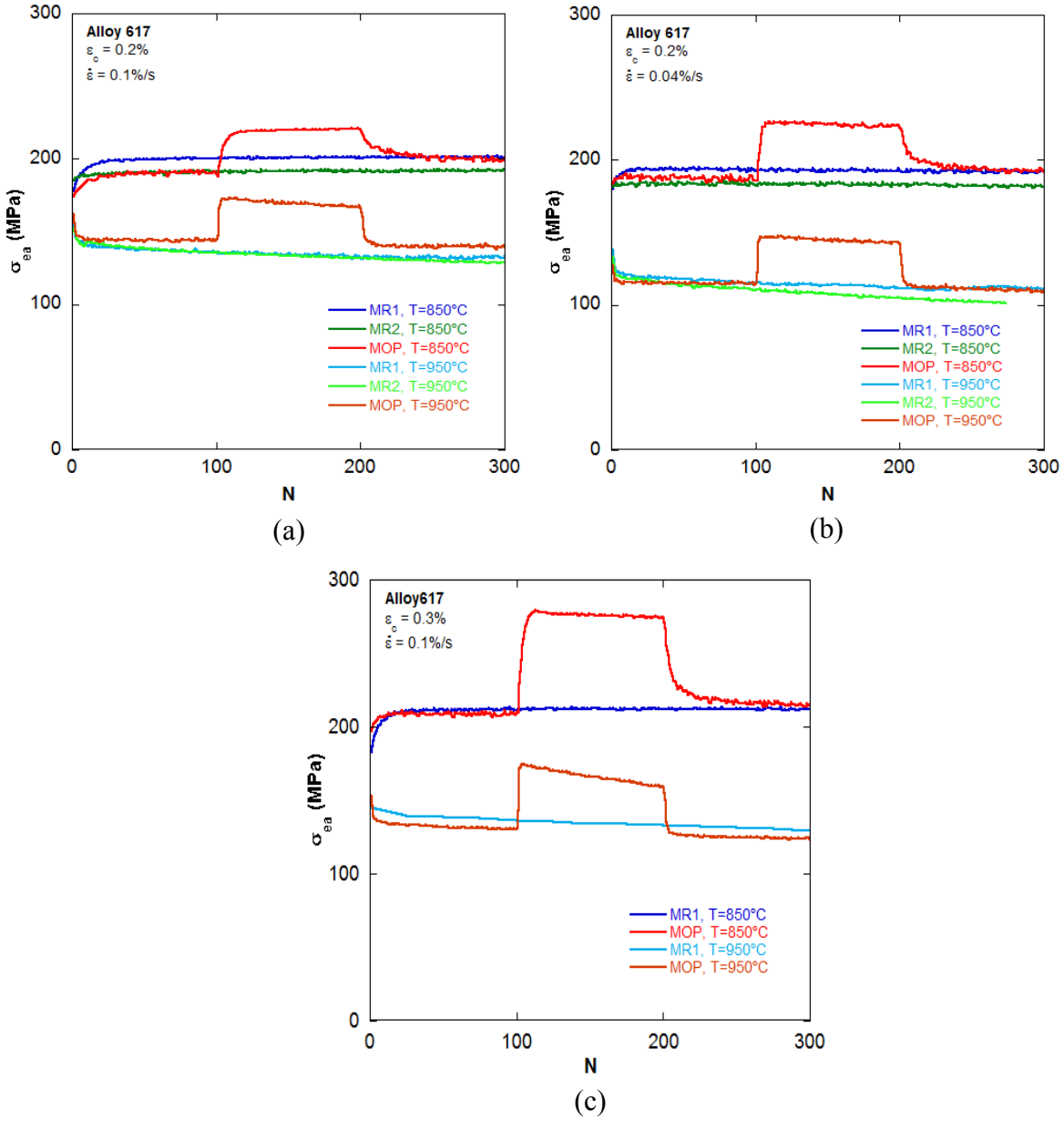

Fig. 13 Comparison of equivalent stress amplitude plotted as a function of number of loading cycles for MR1, MR2 and MOP experiments performed at different temperatures. (a) 0.1%/s strain rate with 0.2% strain amplitude; (b) 0.04%/s strain rate with 0.2% strain amplitude; (c) 0.1%/s strain rate with 0.3% strain amplitude.

In all the cases, regardless of the temperature, strain rate and strain amplitude, MR2 tests showed higher axial strain accumulation with number of loading cycles compared to MR1 tests. This signifies the effect of loading history on the multiaxial ratcheting response of Alloy 617. Although the degree of non-proportionality in the MR2 test was higher than in the MR1 test, however its direct influence is yet to be clear. Also, understanding the influence of the mean axial stress in the MR1 and MR2 tests on axial strain creep and thus on the axial strain ratcheting needs further study.

3.6. Strain Rate Sensitivity

The multiaxial experiments MR1, MR2 and MOP were conducted at two different loading rates (0.04%/s and 0.1%/s) to investigate the effect of strain rate on the creep-fatigue-ratcheting response of Alloy 617. The equivalent stress amplitudes and axial strain ratcheting from MR1 and MR2 tests are plotted as a function of the number of loading cycles in Fig. 14 and Fig. 16, respectively, to demonstrate the effects of strain rate on Alloy 617 at 850ºC and 950ºC. The loading rate effect in the MOP tests is shown in Fig. 15.

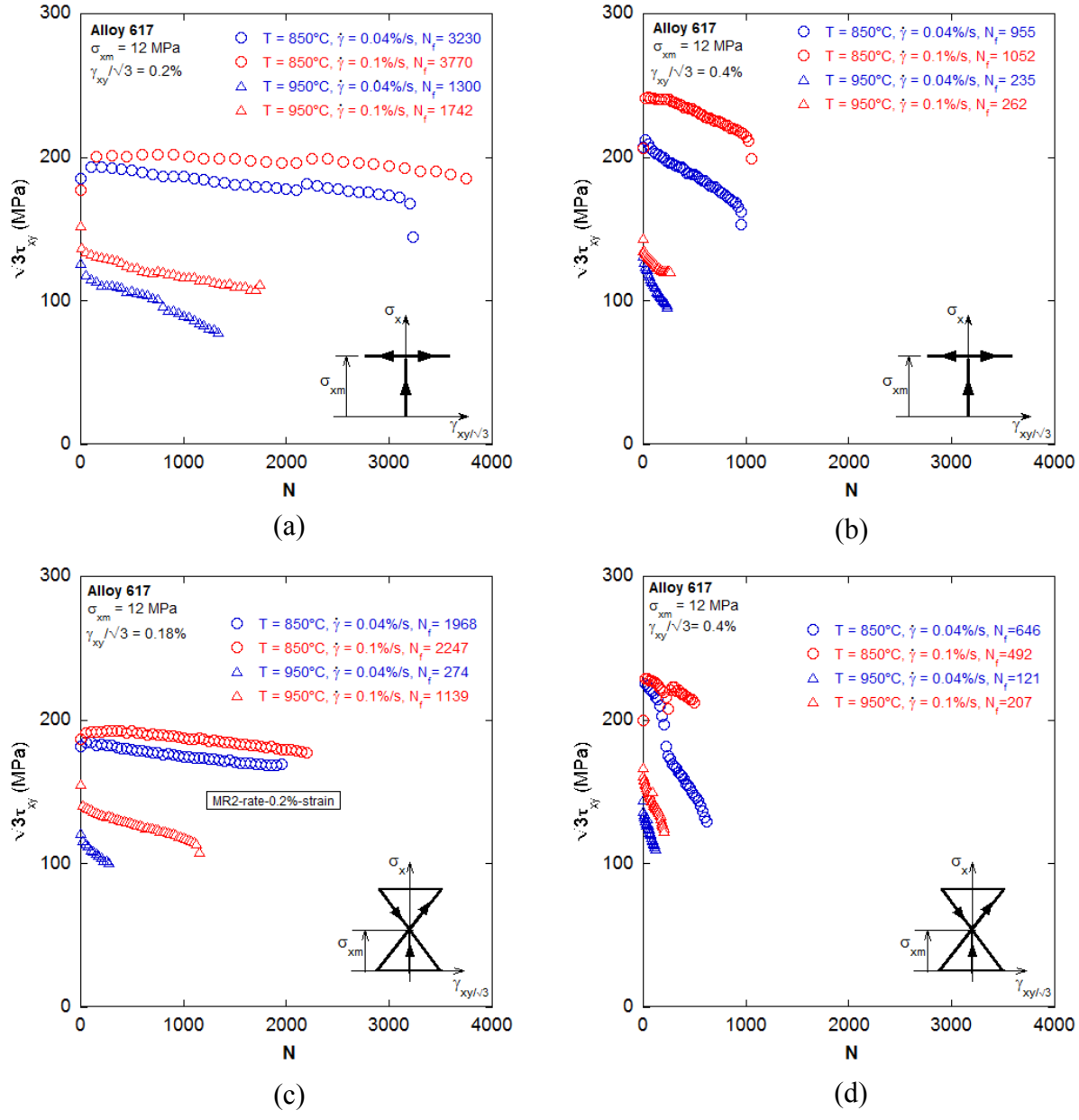

Fig. 14 Equivalent stress amplitude plotted against number of loading cycles for MR1 and MR2 experiments performed at different strain rates and different temperatures. (a) MR1 tests with 0.2% strain amplitude; (b) MR1 tests with 0.4% strain amplitude; (c) MR2 tests with 0.18 % strain amplitude; (d) MR2 tests with 0.4% strain amplitude.

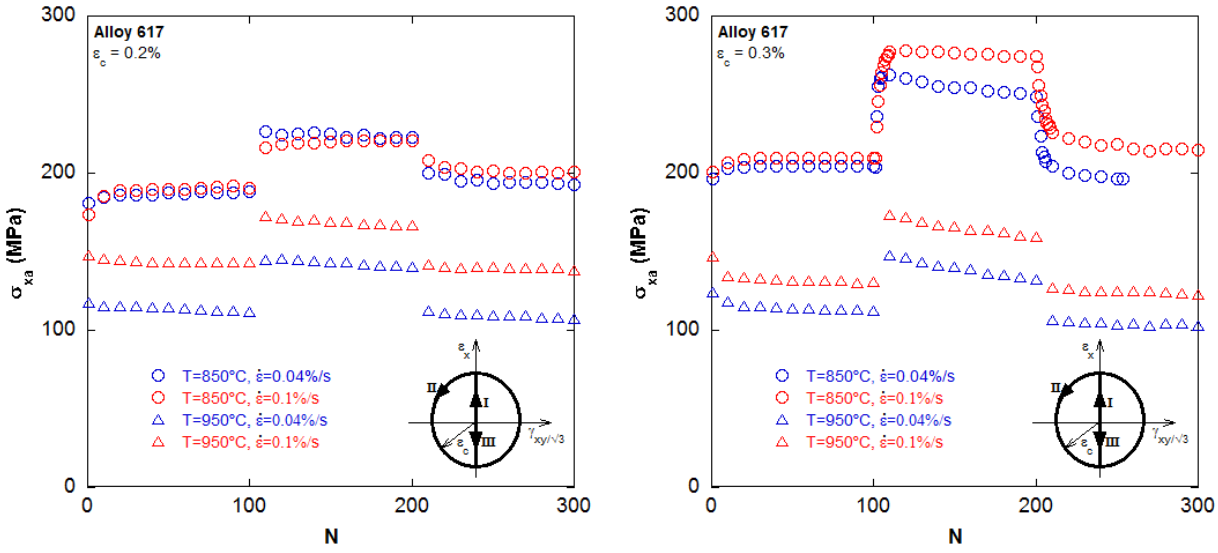

(a) (b)

Fig. 15 Axial stress amplitude plotted against number of loading cycles for MOP experiments at different temperatures and different strain rates. (a) 0.2% strain amplitude; (b) 0.3% strain amplitude.

The equivalent stress amplitude was smaller at 0.04%/s strain rate compared to that at 0.1%/s strain rate regardless of temperature, strain amplitude and loading path. At 850ºC, strain rate effect on the stress amplitude of Alloy 617 is small for all three loading histories at smaller strain amplitudes. For experiments at 850ºC with higher strain amplitudes, there is significant rate effect. However, at 850ºC slower loading rate leads to lower fatigue life of the material for both MR1 and MR2 experiments. At 950ºC, lower fatigue life at slower loading rate was observed for all the specimens tested except for MR1 experiment at 0.2% strain amplitude where slower loading rate seemed to increase the fatigue life of Alloy 617 (Fig. 14a). From the axial strain ratcheting plots of Fig. 16, it was observed that the axial strain increased linearly with the number of loading cycles. Slower loading (0.04%/s) rate showed higher axial strain ratcheting rate compared to faster loading rate for all the experiments performed at 950ºC. On the other hand, at 850ºC, the axial strain accumulation rate seemed to be insensitive of the loading rate for MR2 tests, whereas for MR1 tests, noticeable loading rate effect was observed with axial strain ratcheting rate increased for slower loading rate.

In the MOP tests, effects of loading rate was only observed at 950ºC (Fig. 15), where at 850ºC (Fig. 15a) Alloy 617 seemed to be rate independent for lower strain amplitudes, but experiments performed at 850ºC with higher strain amplitudes showed strain rate dependence for MOP tests (Fig. 15b). The above results show that slower loading rate at higher temperature is more detrimental to Alloy 617. Rao *et al.* (1988a, 1988b) observed similar type of strain rate dependent behavior of Alloy 617 under uniaxial fatigue loading. They explained that the low fatigue life at smaller strain rate was mainly attributed to the continuous increase in inelastic strain with cycle. The other factors that might have played a role in decreasing the fatigue life at slower strain rate are the intergranular crack initiation resulting from oxidation of surface connected grain boundaries and environmentally assisted mixed mode propagation. The effect of

loading rate was also evident from the equivalent shear stress-strain hysteresis loops plotted in Fig. 17, where it can be observed that at 950ºC, the plastic strain amplitude increased for slower loading rate compared to faster loading rate regardless of the strain amplitude and loading non-proportionality. This rate effect on the hysteresis loop shape was noticeable from the first loading cycle at 950ºC and it continued for rest of the loading cycles, whereas, at 850ºC with lower strain amplitude, the loop shape was insensitive to the loading rate in the first cycle, but with increasing number of loading cycle, the rate effect became more prominent. However, for higher strain amplitude, the effect of loading rate was seen from the very first cycle at 850ºC (not shown).

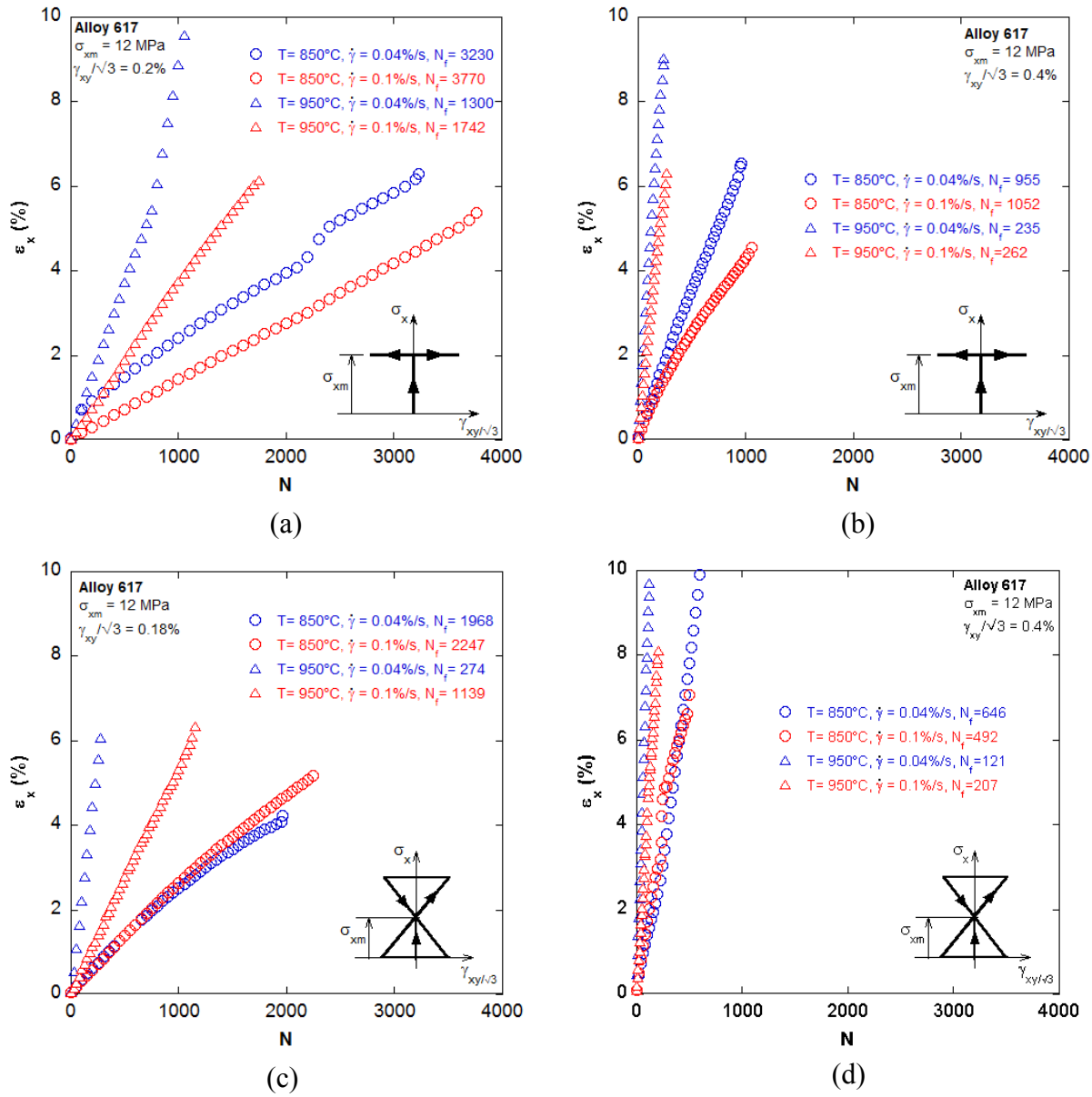

Fig. 16 Axial strain ratcheting with number of loading cycles for MR1 and MR2 experiments performed at different temperatures and strain rates. (a) MR1 tests with 0.2% strain amplitude; (b) MR1 tests with 0.4% strain amplitude; (c) MR2 tests with 0.18% strain amplitude; (d) MR2 tests with 0.4% strain amplitude.

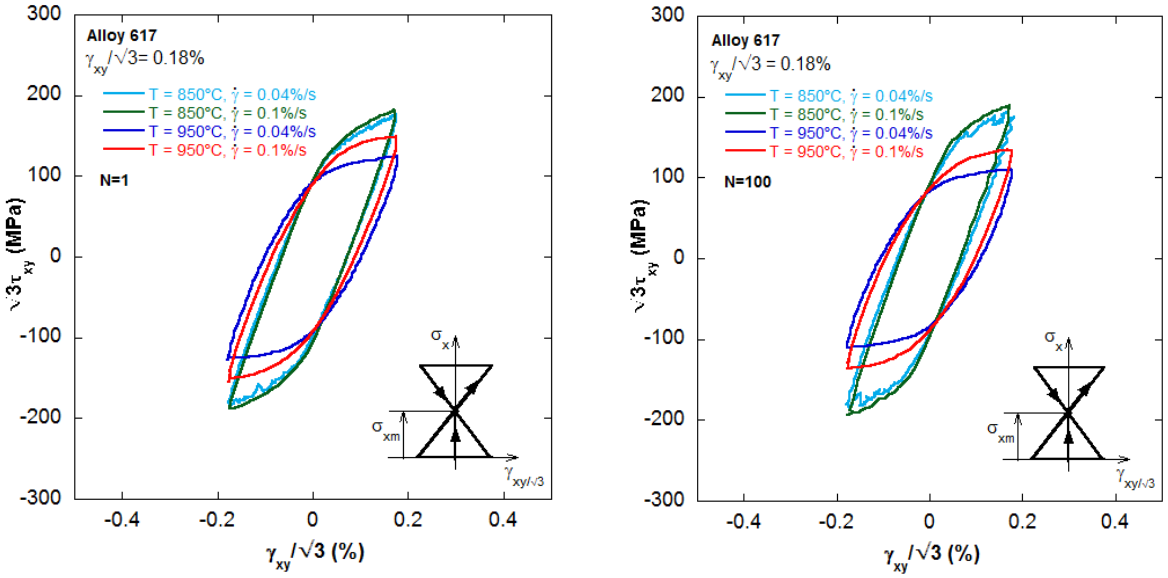

(a) (b)

Fig. 17 Equivalent stress-strain hysteresis loops at different temperatures and strain rates for MR2 experiment performed at 0.18% strain amplitude; (a) 1st cycle; (b) 100th cycle.

Another interesting phenomenon that was observed was serrated flow. Alloy 617 showed serrated stress-strain behavior only at 850ºC for slower strain rate (0.04%/s). For faster strain rate, no serrated flow was observed. The serrated flow is considered to be one of the manifestations of dynamic strain aging (DSA) (Reed-Hill, 1974). Fig. shows equivalent stress-strain hysteresis response of Alloy 617 for different loading cycles for one MR1 test performed at 850ºC with 0.04%/s strain rate.

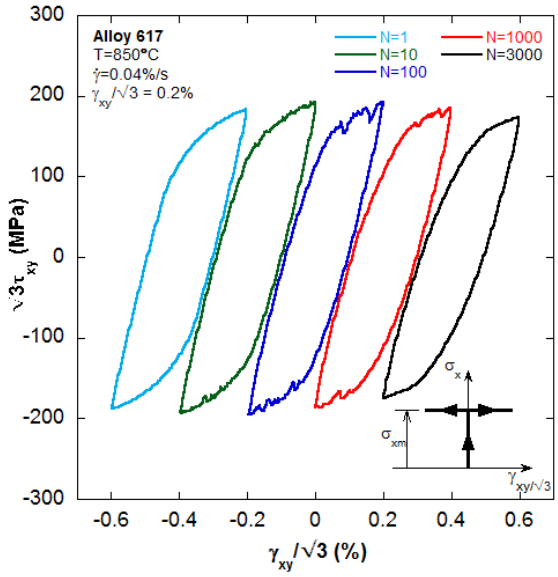

Fig. 18 Equivalent stress-strain hysteresis loops at different loading cycles for MR1 experiment performed at 850ºC with 0.2% strain amplitude and 0.04%/s strain rate showing serrated stress-strain behavior.

It can be observed that the first cycle did not have any serrations, but with the evolution of cycles the serrations became more substantial and the serrations gradually vanished away at the end of the loading cycles. Similar behavior was observed for MR2 test as can be seen in Fig. 17 where serrations were observed for both cycle 1 and 100 for slower loading rate at 850ºC. The serrated stress-strain behavior for Alloy 617 was also observed by Rao *et al.* (1988a) at 750ºC and 850ºC and Rahman *et al.* (2009) between 600-800ºC with slower loading rate. From the multiaxial experimental responses of Alloy 617 for different loading rates, it was evident that Alloy 617 is highly rate dependent at higher temperatures; especially at 950ºC. The rate effect was more dominant at higher strain amplitudes. However, the effect loading non-proportionality on the loading rate was not conclusive. It must be mentioned here that at 25ºC and 650ºC, Alloy 617 does not show any rate dependent behavior, and hence, tests at these temperatures were conducted for only one strain rate (0.1%/s).

3.7. Strain Amplitude Dependence

Three strain amplitudes (0.2%, 0.3%, 0.4%) were considered for the multiaxial experiments to determine the effect of strain amplitude on the creep-fatigue-ratcheting response of Alloy

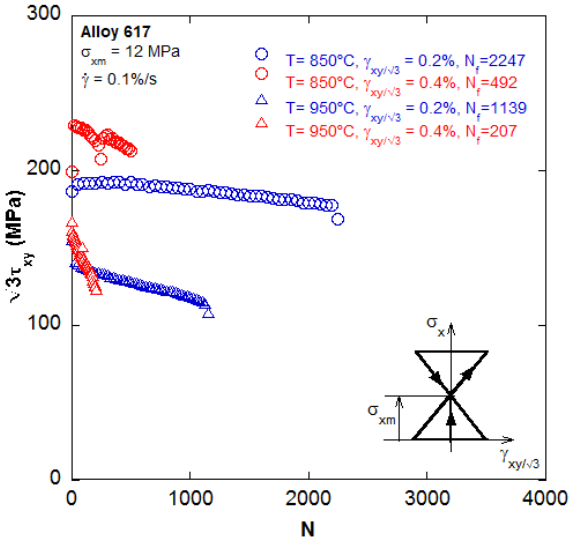

617.

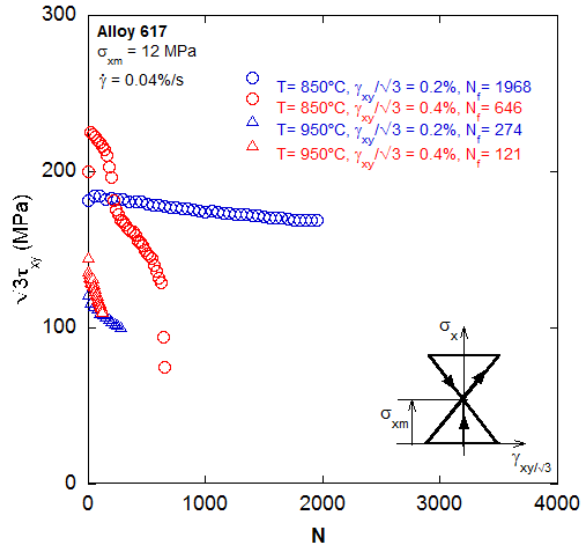

Fig. 19, Fig. 21, Fig. 22 show the effect of strain amplitude of the loading path on the equivalent stress amplitude, axial strain ratcheting and hysteresis loops in the MR1 and MR2 experiments, respectively, whereas

Fig. 20 shows the effect of strain amplitude of loading path on the axial stress amplitude for MOP experiments.

As expected, the equivalent and axial stress amplitude and axial strain ratcheting of Alloy 617 were influenced by the strain amplitude of the loading paths. With an increase in the strain amplitude, the creep-fatigue life reduced and the axial strain ratcheting rate increased

regardless of loading rate, temperature and loading history. An increase in strain amplitude signifies an increase in plastic strain amplitude as shown in Fig. 22, and this in turn increased the accumulation of axial strain ratcheting rate (Fig. 21). Consequently, the fatigue life decreased. It was noted that the effect of higher strain amplitude was more detrimental at higher temperature, and also the effect of loading rate was more significant at higher strain amplitudes. For MOP experiments, the stress jump due to cross effect was more significant for higher strain amplitude compared to lower strain amplitude at 850ºC for both slower and faster strain rates as shown in

Fig. 20. Especially, at 850ºC with faster strain rate, the stress jump was noteworthy. However, at 950ºC, the effect of strain amplitude on the stress jump was not as significant as observed at 850ºC for both the strain rates.

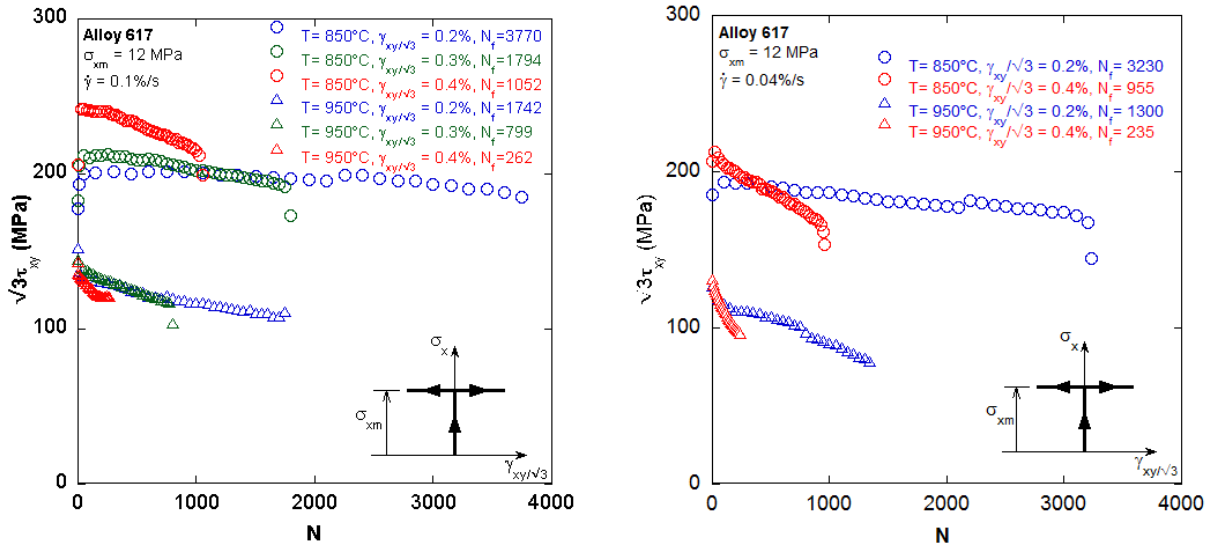

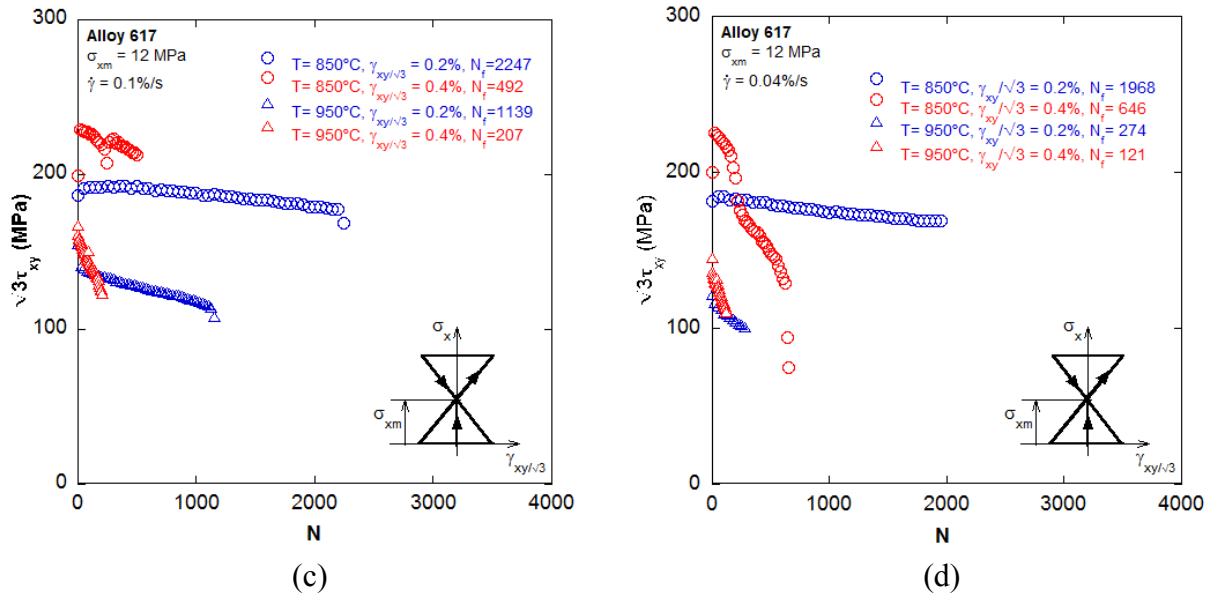

Fig. 19 Equivalent stress amplitude plotted against number of loading cycles for MR1 and MR2 experiments performed at different temperatures and strain amplitudes. (a) MR1 tests at 0.1%/s strain rate; (b) MR1 tests at 0.04%/s strain rate; (c) MR2 tests at 0.1%/s strain rate; (d) MR2 tests at 0.04%/s strain rate.

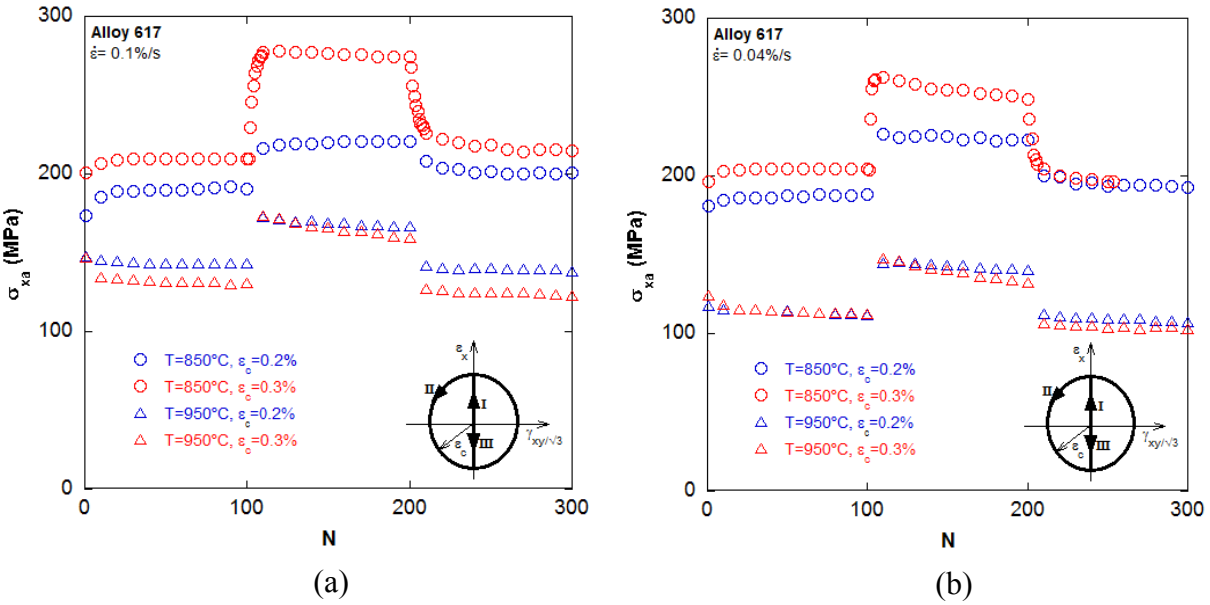

Fig. 20 Axial stress amplitude plotted against number of loading cycles for MOP tests at different temperatures and strain amplitudes. (a) 0.1%/s strain rate; (b) 0.04% strain rate.

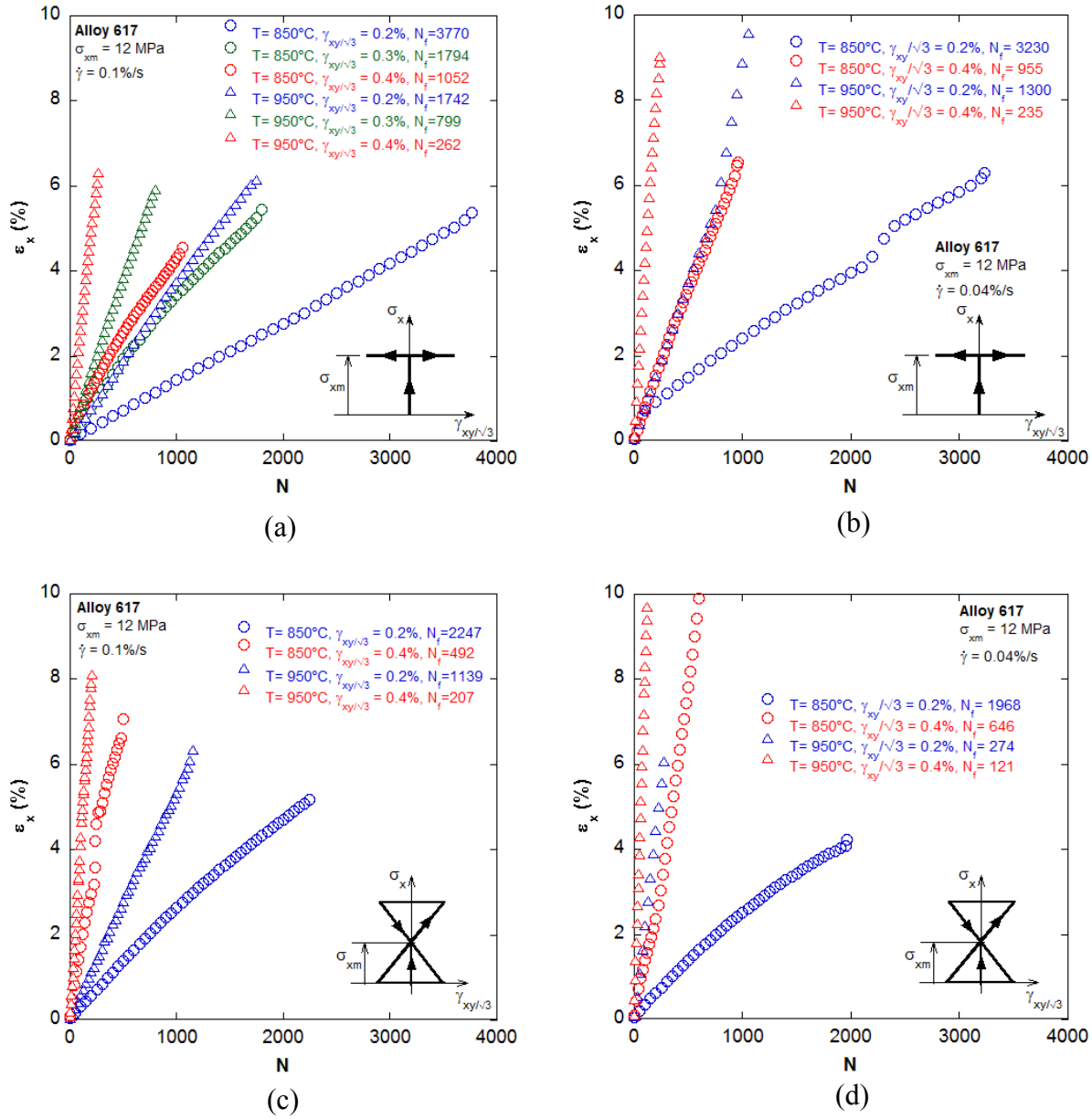

Fig. 21 Axial strain ratcheting with number of loading cycles for MR1 and MR2 tests performed at different temperatures and strain amplitudes. (a) MR1 tests at 0.1%/s strain rate; (b) MR1 tests at 0.04%/s strain rate; (c) MR2 tests at 0.1%/s strain rate; (d) MR2 tests at 0.04%/s strain rate.

3.8. Failure Modes

Table 3 shows a summary of MR1 and MR2 experiments in terms of number of loading cycles to failure (N_f), time to failure (t_f) and the associated failure modes observed. It was noted that all the specimens at 850ºC failed through either diagonal or transverse cracks in the gage section, whereas at 950ºC, the specimens failed by necking or localized deformation. In some

cases the specimens did not fail or the testing equipment became unstable during the high temperature testing. However, no crack or failure was observed for tests performed at 25ºC and 650ºC. The number of loading cycles to failure and time to failure shown in Table 3 also shows the effect of temperature, strain rate, strain amplitude and loading history and their interdependence as discussed above. To explain the failure mode of the material, microstructural investigation is required by using scanning electron microscopy (SEM) and transmission electron microscopy (TEM) since the failure mode and the material behavior is highly dependent on microstructural phenomena like crack initiation, transgranular, intergranular and intragranular propagation, carbide precipitation, surface oxidation and decarburization (Rao *et al.*, 1988a, 1988b, Burke and Beck, 1984).

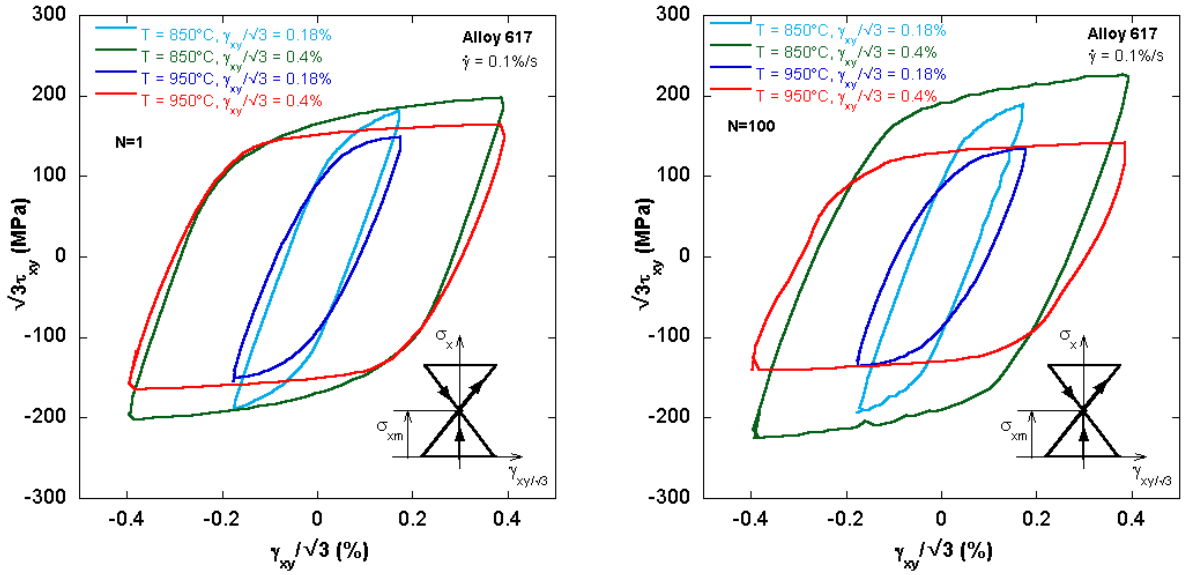

(a) (b)

Fig. 22 Equivalent stress-strain hysteresis loops at different temperatures and strain amplitudes for MR2 experiments performed at 0.1% strain rate. (a) 1st cycle; (b) 100th cycle.

4. Conclusion

A broad set of multiaxial experiments were conducted to investigate the creep-fatigue-ratcheting responses of Alloy 617 and thereby aid in developing an experimentally validated unified constitutive model (UCM) for simulation of the responses. Critical analysis of experimental responses led to the following conclusions:

- Multiaxial creep-fatigue and ratcheting responses of Alloy 617 were significantly influenced by the temperature, strain rate, strain amplitude and loading non-proportionality.
- The hardening/softening behavior of the alloy was different at higher and lower temperatures. At 25ºC, the material showed cyclic hardening for initial few cycles followed by steady stress state, whereas at 650ºC, the material showed continuous cyclic hardening up to 4000 cycles. For higher temperature range, the material showed cyclic hardening for the initial few cycles

followed by cyclic softening at 850ºC, whereas at 950ºC, the material showed continuous cyclic softening.

- At 950ºC and slower loading rate (0.04%/s), there was a significant reduction in the fatigue life of Alloy 617. With an increase in the strain amplitude, the decrease in fatigue life became more substantial.
- The effect of loading non-proportionality, strain amplitude and strain rate was noteworthy at 950ºC. The material seems to be insensitive to strain rate at 850ºC for lower strain amplitude, but at higher strain amplitude, the material showed rate dependence at 850ºC.
- The axial strain ratcheting rate was high at higher temperature (950ºC) and slower loading rate (0.04%/s). The ratcheting rate increases with an increase in the strain amplitude.
- Serrated stress-strain response was observed for Alloy 617 at 850ºC with slower loading rate which is one of the manifestations of dynamic strain aging (DSA).
- The loading history had strong influence on the creep-fatigue and ratcheting responses of Alloy 617. The fatigue life of material from MR2 tests was lower compared to MR1 tests. Since the axial stress was cycled in the MR2 tests the fatigue damage in these tests was more significant compared to the MR1 tests. Moreover, the influence of loading non-proportionality was evident from the cross hardening in the MOP tests.

These observations from the multiaxial experimental responses manifests the necessity of incorporating rate dependence, strain amplitude dependence and effect of loading non-proportionality and temperature in the development of the unified constitutive model (UCM) to provide a better prediction of the viscoplastic behavior of the material. The development of an improved UCM and it simulation responses is presented in another article by Islam et al. [2014] .

Copyright Notice
This manuscript has been authored by Battelle Energy Alliance, LLC under Contract No. DE-AC07-05ID14517 with the U.S. Department of Energy. The United States Government retains and the publisher, by accepting the article for publication, acknowledges that the United States Government retains a nonexclusive, paid-up, irrevocable, world-wide license to publish or reproduce the published form of this manuscript, or allow others to do so, for United States Government purposes.

Acknowledgement
The research is being performed using funding received from the DOE Office of Nuclear Energy's Nuclear Energy University Program.

Nomenclature

ε_x	Axial strain
ε_c	Axial strain amplitude
$\dot{\varepsilon}$	Axial strain rate
σ_x	Axial stress
σ_{xm}	Mean axial stress
σ_{xc}	Axial stress amplitude
γ_{xy}	Shear strain
$\dot{\gamma}$	Shear strain rate
τ_{xy}	Shear stress

τ_c Shear stress amplitude
τ_m Mean shear stress
N Number of loading cycles
t Time
T Temperature
N_f Number of loading cycles to failure
t_f Time to failure
LD Localized deformation
NF No failure
(•) Differential with respect to time

References

[1] ASTM Designation E606, 1980. Standard recommended practice for constant-amplitude low-cycle fatigue testing.

[2] Baldwin, D.H., Kimball, O.F., and Williams, R.A., 1986. Design data for reference alloys: Inconel 617 and Alloy 800H. General Electric Company for the Department of Energy, Contract No. DE-AC03-80ET34034.

[3] Breitling, H., Dietz, W., and Penkalla, H.J., 1988. Evaluation of mechanical properties of the Alloy NiCr22Co12Mo (Alloy 617) for heat exchanging components of HTGRs. IWGGCR, High Temperature Metallic Materials for Gas Cooled Reactors, Cracow, Poland.

[4] Burke, M.A., and Beck, C.G., 1984. The high temperature low cycle fatigue behavior of the nickel base alloy IN-617. Metall. Trans. A. 15A, 661-670.

[5] Carroll, L., Madland, R., and Wright, R., 2011. Creep-fatigue of high temperature materials for VHTR: effect of cyclic loading and environment. Paper 11284, Proceedings of ICAPP 2011, Nice, France.

[6] Carroll, L., Cabet, C., and Wright, R., 2010. The role of environment on high temperature creep-fatigue behavior of Alloy 617. PVP2010-26126, ASME 2010 Pressure Vessels and Piping Conference, ASME, Washington, USA.

[7] Charit, I., and Murty, K.L., 2010. Structural materials issues for the next generation fission reactors," Journal of Materials 62(9), 67-74.

[8] Chen X., Jiao R., and Kim K.S., 2005. On the Ohno-Wang kinematic hardening rules for multiaxial ratcheting modeling of medium carbon steel. Int. J. Plast. 21, 161-184.

[9] Chen, X., Sokolov, M.A., Sham, S., Erdman III, D.L., Busby, J.T., Mo, K., and Stubbins, J.F., 2013. Experimental and modeling results of creep-fatigue life of Inconel 617 and Haynes 230 at 850ºC. J. Nucl. Mater. 432, 94-101.

[10] Corona, E., Hassan, T., and Kyriakides, S., 1996. On the performance of kinematic hardening rules in predicting a class of biaxial ratcheting histories. Int. J. Plast.12, 117-145.

[11] Corum, J.M., and Blass, J.J., 1991. Rules for design of Alloy 617 nuclear components to very high temperatures. PVP (Am. Soc. Mech. Eng.) 215, 147–153.

[12] Corwin, W.R., 2006. U.S. Generation IV reactor integrated materials technology program. Nucl. Eng. Tech. 38, 591–618.

[13] Ellis J.R., and Bartolotta P.A., 1997. Adjustable work coil fixture facilitating the use of induction heating in mechanical testing. Multiaxial Fatigue and Deformation Testing Techniques, ASTM STP 1280, S. Kalluri and P. J. Bonacuse, Eds., American Society for Testing and Materials, 43-62.

[14] Hassan, T., Taleb, L., and Krishna, S., 2008, Influence of non-proportional loading on ratcheting responses and simulations by two recent cyclic plasticity models. Int. J. Plast. 24, 1863-1889.
[15] Hassan, T., and Kyriakides, S., 1994. Ratcheting of cyclically hardening and softening materials: II. Multiaxial behavior. Int. J. Plast. 10(2), 185-212.
[16] Independent Technology Review Group-INEEL/EXT-04-01816, June 2004. Design features and technology uncertainties for the next generation nuclear plant.
[17] INL-PLN-2804, April 2008. Next generation nuclear plant intermediate heat exchanger materials research and development plan.
[18] Kanazawa, K., Miller K.J., and Brown, M.W., 1979. Cyclic deformation of 1% Cr-Mo-V steel under out-of-phase loads. Fatigue Fract. Eng. Mater. Struct. 2(2), 217-228.
[19] Krishna, S., Hassan, T., Naceur, I.B., Sai, K., and Cailletaud, G., 2009. Macro versus micro-scale constitutive models in simulating proportional and nonproportional cyclic and ratcheting responses of stainless steel 304. Int. J. Plast. 25, 1910-1949.
[20] Lamba, H.S., and Sidebottom, O.M., 1978. Cyclic plasticity for nonproportional paths. Parts 1 and 2: Comparison with predictions of three incremental plasticity models. J. Eng. Mater. Technol. 100, 96-111.
[21] Lissenden, C.J., Walker, M.A., and Lerch, B.A., 2000. Axial-torsional load effects of Haynes 188 at 650. Multiaxial fatigue and Deformation Testing and Prediction, ASTM STP 1387, S. Kalluri and P. J. Bonacuse, Eds., American Society for Testing and Materials, West Conshohocken, PA, 99-125.
[22] Maier, G., Riedel, H., Seifert, T., Klower, J., and Mohrmann, R., 2011. Time and temperature dependent cyclic plasticity and fatigue crack growth of the nickel-base Alloy617B-experiments and model. Adv. Mater. Res. 278, 369-374.
[23] Maier, G., Riedel, H., and Somsen, C., 2013. Cyclic deformation and lifetime of Alloy 617B during isothermal low cycle fatigue. Int. J. Fatigue 55, 126-135.
[24] McCoy, H.E., and King, J.F., 1985. Mechanical properties of Inconel 617 and 618. U.S. Department of Energy, Report No. ORNL/TM-9337.
[25] McDowell, D.L., 1985. A two surface model for transient nonproportional cyclic plasticity: Part 2. Comparison of theory and experiments. ASME J. Appl. Mech. 52(2), 303-308.
[26] Meurer, H.P., Gnirss, G.K.H., Mergler, W., Raule, G., Schuster, H. and Ullrich, G., 1984. Investigations on the fatigue behavior of high-temperature alloys for high-temperature gas-cooled reactor components. Nucl. Technol. 66. 315-323.
[27] Nagato, K., Murakami, T. and Hashimoto, T., 1989. High temperature low-cycle fatigue strength of Hastelloy-XR. IWGGCR, High Temperature Metallic Materials for Gas Cooled Reactors, Cracow, Poland.
[28] Natesan, K., Moisseytsev, A., and Majumdar, S., 2009. Preliminary issues associated with the next generation nuclear plant intermediate heat exchanger design. J. Nucl. Mater. 392(2), 307-315.
[29] Project Proposal-NGNP grant-09-288. Creep-fatigue and creep-ratcheting failures of alloy 617: experiments and unified constitutive modeling towards addressing the ASME code issues.
[30] Rahman, M.S., Priyadarshan, G., Raja, K.S., Nesbitt, C., and Misra, M., 2009. Characterization of high temperature deformation behavior of INCONEL 617. Mech. Mater. 41, 261-270.

[31] Rao, K.B.S, Schiffers, H., Schuster, H., and Nickel, H., 1988. Influence of time and temperature dependent processes on strain controlled low cycle fatigue behavior of Alloy 617. Metall. Trans. A. 19A, 359-371.
[32] Rao, K.B.S., Meurer, H.P., and Schuster, H., 1988. Creep-fatigue interaction of Inconel 617 at 950ºC in simulated nuclear reactor helium. Mater. Sci. Eng. A104, 37-51.
[33] Reed-Hill, R.E., 1974. The inhomogeneity of plastic deformation. Rev. High Temp. Mat. 2, 217-242.
[34] Ren, W., and Swindeman, R., 2009. A review on current status of Alloys 617 and 230 for Gen IV nuclear reactor internals and heat exchangers. J. Pressure Vessel Technol. 131, 044002.
[35] Ren, W., Totemeier, T., Santella, M., Battiste, R., and Clark, D., 2006. Status of testing and characterization of CMS Alloy 617 and Alloy 230. U.S. Department of Energy, Report No. ORNL/TM-2006-547.
[36] Sliwowski, M., 1979. Behavior of stress-strain diagrams for complex cyclic loadings. Bulletin de I'Academie Polonaise Des Sciences, Serie des Sciences Techniques, Vol. 17, 115-124.
[37] Tsuji, H., and Kondo, T., 1987. Strain-time effects in low-cycle fatigue of nickel-base heat-resistant alloys at high temperatures. J. Nucl. Mater. 150, 259–265.
[38] Tanaka, E., Murakami, S., and Ooka, M., 1985. Effects of strain path shapes on non-proportional cyclic plasticity. J. Mech. Phys. Solids 33(6), 559-575.
[39] Totemeier T. C., Tian H., 2007. Creep-fatigue-environment interactions in INCONEL 617. Mater. Sci. Eng. 468 - 470, 81 – 87.
[40] Wright, R., Simpson, J., Wertsching, A., and Swank, W.D., 2008. High temperature behavior of candidate VHTR heat exchanger alloys. Proc. 4th International Topical Meeting on High Temperature Reactor Technology HTR 2008, Washington, DC, 1–5.
[41] Wright, J.K., Carroll, L.J., Cabet, C., Lillo, T.M., Benz, J.K., Simpson, J.A., Lloyd, W.R., Chapman, J.A., and Wright, R.N., 2012. Characterization of elevated temperature properties of heat exchanger and steam generator alloys. Nucl. Eng. Des. 251, 252-260.
[42] Wright, R.N., 2006. Summary of studies of aging and environmental effects on Inconel 617 and Haynes 230. INL/EXT-06-11750.

Constitutive Modeling of High Temperature Fatigue and Fatigue-Creep Responses of Alloy 617

P. Graham Pritchard and Tasnim Hassan*

Department of Civil, Construction and Environmental Engineering

North Carolina State University, Raleigh, NC

Abstract

The Intermediate Heat Exchanger (IHX) is a critical component in the design of Next Generation Nuclear Plants (NGNP) and will be subjected to low-cycle fatigue loading at high temperatures during its service life. To meet the design requirements of the IHX alloy 617, a nickel-chromium based alloy with excellent high-temperature strength, has been chosen as a candidate material. In order to design IHX components according to ASME Code Subsection NH design by analysis methodologies, a nonlinear constitutive model capable of predicting high temperature fatigue and fatigue-creep responses is required. This study made an effort to develop a high temperature, rate-dependent, unified constitutive model that is capable of simulating a wide variety of low-cycle fatigue material responses. This chapter presents the model development, implementation and experimental validation of the unified constitutive model against the experimental responses presented in Chapter 2. The current state of the unified constitutive model in simulating low-cycle fatigue responses and future work needed for further model development are enumerated.

* Corresponding author, thassan@ncsu.edu, 1-919-515-8123

1. Introduction

In the design of Next Generation Nuclear Plants (NGNP), the Intermediate Heat Exchanger (IHX) is a critical component. The IHX exchanger will be subjected to wide variety of low-cycle fatigue loading over the course of its service life due to both reactor start-ups and shut-downs and power transients. In addition, the outlet gas temperature of the IHX is expected to be in the range of 850°C – 950°C, a large increase from previous generations of nuclear power plants. The meet the requirement of the service conditions alloy 617, a nickel-chromium alloy with excellent high temperature strength and creep resistance has been chosen as the candidate material for the IHX component.

For the design of IHX components a nonlinear constitutive model capable of simulating a wide range of fatigue and fatigue-creep responses is required as per ASME Code subsection NH design by analysis methodologies. To meet this requirement a broad fatigue and fatigue-creep experimental database for alloy 617 was developed as presented in Chapter 2. The experimental responses from Carroll and her coworkers [1-3] and Wright et al. [4] are also used in experimental verification of the constitutive model. These fatigue and fatigue-creep experimental responses were generated across temperature ranging from 25°C to 950°C with particular focus paid to the elevated temperatures of 850°C and 950°C; note that fatigue-creep tests were only performed at 850°C and 950°C. For all temperatures the effect of loading rate and strain-range were investigated. Additionally, at 950°C, the effect of hold time under fatigue-creep loading was also studied.

This work will be split into five sections. First, the constitutive model that was implemented will be described. Second, the numerical implementation of the model will be discussed. Third, the parameter determination process will be outlined in detail. Fourth, representative model parameters will be presented for both rate-independent and rate-dependent responses. Finally, model simulations of the broad set of material responses will be presented to demonstrate the experimental validation of the model and elaborating future model development needs.

2. Unified Constitutive Model

In this section the equations which compose the constitutive model will be presented and their functions described. As can be seen in Eq. 1, the generalized Hooke's law was used to relate stress tensor $\underline{\sigma}$ and elastic strain tensor $\underline{\varepsilon}^e$ through the elasticity tensor $\underline{\underline{E}}$.

$$\underline{\sigma} = \underline{\underline{E}}\left(\underline{\varepsilon} - \underline{\varepsilon}^{in}\right) \quad \text{..... (1)}$$

Additive stain decomposition shown in Eqn. 2 was used to separate the elastic strain from the inelastic strain. This investigation utilized a unified constitutive model thus the inelastic strain term represents both the plasticity and creep strain components as one single value.

$$\underline{\varepsilon} = \underline{\varepsilon}^{e} + \underline{\varepsilon}^{in} \quad \text{..... (2)}$$

The Von-Mises yield surface, Eqn. 3, was used as the limit of the elastic domain. Note that R is the isotropic hardening term and is a function of the accumulated plastic strain p; $\underline{\sigma}$ and $\underline{s}$ represent the stress and deviatoric stress respectively; $\underline{\alpha}$ and $\underline{a}$ represent the back stress and deviatoric back stress respectively.

$$f\left(\underline{\sigma} - \underline{\alpha}\right) = J\left(\underline{\sigma} - \underline{\alpha}\right) - \sigma_o - R(p) \quad \text{..... (3)}$$

$$J\left(\underline{\sigma} - \underline{\alpha}\right) = \sqrt{\frac{3}{2}\left(\underline{s} - \underline{a}\right) : \left(\underline{s} - \underline{a}\right)} \quad \text{..... (4)}$$

A viscoplastic flow rule was adopted as suggested by Chaboche [5] and is expressed by Eqns. 5 and 6, where K and n are model parameters. The basis for the flow rule was constructed from Norton's power law of secondary creep. However, in this characterization the strain rate is not determined from the overall magnitude of the applied stress but from the overstress, the distance from the current stress state to the yield surface, which is in this case equivalent to the numerator in Eqn. 6.

$$\dot{\underline{\varepsilon}}^{in} = \frac{3}{2}\dot{p}\frac{\underline{s}-\underline{a}}{J\left(\underline{\sigma}-\underline{\alpha}\right)} \quad \text{..... (5)}$$

$$\dot{p} = \left\langle \frac{J\left(\underline{\sigma}-\underline{\alpha}\right)-R\left(p\right)-\sigma_o}{K} \right\rangle^n \quad \text{..... (6)}$$

The kinematic hardening rule used in this investigation is shown in Eqn. 7. It can be said to be composed of four primary components, a linear hardening term (Eqn. 7a), a dynamic recovery term (Eqn. 7b), a static recovery term (Eqn. 7c), and a temperature dependence term (Eqn. 7d). The combination of the linear hardening and the dynamic recovery terms are essential for the description of the hysteresis loop shape under typical reversed fatigue loading. The static recovery term allows for the prediction of stress relaxation. Lastly, for the prediction of anisothermal responses, the temperature term is necessary.

In order to show the development of this particular back stress the following brief history is presented. The base structure of the back stress is the kinematic hardening rule suggested by Armstrong and Frederick [6]. This was later expanded by incorporating the static-recovery term suggested by Chaboche [7]. Then the back stress was expanded by Chaboche et al. [8] to include superimposed back stress rules to increase the accuracy of model simulations. The multiaxial ratcheting term δ' and the correspondingly modified dynamic recovery term were introduced by Bari and Hassan [9]. Lastly, the temperature dependence term was suggested by Chaboche [10]. This study addresses the modeling of uniaxial responses only. Furthermore, the temperature term is only necessary to simulate anisothermal loadings, which is not a part of this investigation. With this in mind the kinematic rule can be reduced to the simpler form shown in Eqn. 8 which can be shown to be equivalent to Eqn. 7 under uniaxial and isothermal loading. Eqn. 9 describes the superposition of four kinematic rules as in Eqn. 8. The equivalent back stress, as used in Eqn. 7c is described by Eqn. 10. Note that C_i, γ_i, b_i, r_i, and δ' are all model parameters, γ_i being a function of both the radius of the strain memory surface, as will be discussed later, and the accumulated plastic strain; $\underline{n}$ is the normal to the yield surface.

$$\dot{\underline{a}}_i = \underbrace{\frac{2}{3} C_i \dot{\underline{\varepsilon}}^{in}}_{(a)} \underbrace{- \gamma_i (p,q) \left[\delta' \underline{a}_i + (1-\delta') (\underline{a}_i : \underline{n}) \underline{n} \right] \dot{p}}_{(b)} \underbrace{- b_i J(a_i)^{r-1} a_i}_{(c)} + \underbrace{\frac{1}{C_i} \frac{\partial C_i}{\partial T} \dot{T} \underline{a}_i}_{(d)} \quad (7)$$

$$\dot{\underline{a}}_i = \frac{2}{3} C_i \dot{\underline{\varepsilon}}^{in} - \gamma_i (p,q) \underline{a}_i \dot{p} - b_i J(a_i)^{r-1} a_i \quad \text{..... (8)}$$

$$\dot{\underline{a}} = \sum_{i=1}^{4} \dot{\underline{a}}_i \quad \text{..... (9)}$$

$$J(a_i) = \sqrt{\frac{3}{2} \underline{a}_i : \underline{a}_i} \quad \text{..... (10)}$$

To account for yield surface size change (isotropic hardening), two superimposed exponential hardening rules were implemented according to Eqns. 11-13. Having two superimposed rules increased the accuracy of cyclic hardening predictions at lower temperatures.

$$R = R_1 + R_2 \quad \text{..... (11)}$$

$$\dot{R}_1 = b_1 \left(R_1^{st} - R_1 \right) \dot{p} \quad \text{..... (12)}$$

$$\dot{R}_2 = b_2 \left(R_2^{st} - R_2 \right) \dot{p} \quad \text{..... (13)}$$

As shown in Chapter 1, alloy 617 shows significant strain-range dependent responses. To account for this behavior, a strain memory surface criterion, as proposed by Chaboche et al. [8], has been implemented as shown in Eqn. 14. Here $\underline{\varepsilon}^{in}$ represents the current plastic strain tensor, $\underline{Y}$ the kinematic center, and q_{sr} the current radius of the strain memory surface. The isotropic update rule for this criterion is shown in Eqn. 15 and the kinematic update rule in Eqn. 16. These equations are the same as proposed by Chaboche et al. [8] except that they incorporate an additional model parameter η, proposed by Nouailhas et al. [11], which allows one to control the proportional rate of kinematic and isotropic hardening of the strain memory surface. This parameter plays a large role in cases where a mean strain exists. Note

that $\underline{n}$ and $\underline{n}^*$, as shown in Eqns. 17 and 18, are the normals to the Von-Mises and the strain memory surfaces respectively.

$$g\left(\underline{\varepsilon}^{in}-\underline{Y}\right)=\left[\frac{2}{3}\left(\underline{\varepsilon}^{in}-\underline{Y}\right):\left(\underline{\varepsilon}^{in}-\underline{Y}\right)\right]^{1/2}-q_{sr}\le 0 \quad \text{..... (14)}$$

$$\dot{q}_{sr}=\eta\left\langle \underline{n}:\underline{n}^{*}\right\rangle \dot{p} \quad \text{..... (15)}$$

$$\dot{\underline{Y}}=\sqrt{\frac{3}{2}}(1-\eta)\left\langle \underline{n}:\underline{n}^{*}\right\rangle \underline{n}^{*}\dot{p} \quad \text{..... (16)}$$

$$\underline{n}=\sqrt{\frac{3}{2}}\frac{\underline{s}-\underline{a}}{J\left(\underline{\sigma}-\underline{\alpha}\right)} \quad \text{..... (17)}$$

$$\underline{n}^{*}=\sqrt{\frac{2}{3}}\frac{\underline{\varepsilon}^{p}-\underline{Y}}{J\left(\underline{\varepsilon}^{p}-\underline{Y}\right)} \quad \text{..... (18)}$$

The last modeling feature to be implemented is the γ_i hardening evolution presented below. As described by Krishna et al. [12], cyclic hardening or softening of materials can be induced by either expansion or contraction of the yield surface, and/or by shape change of the hysteresis curve. The modeling of yield surface size change (expansion or contraction) is conventionally known as isotropic hardening and achieved through Eqns. 3-4 and 11-13. Cyclic hardening or softening induced by hysteresis curve shape change can be achieved through evolving the plastic modulus C_i and/or dynamic recovery parameter γ_i in the kinematic hardening rule (Eqns. 8-9) as demonstrated by Krishna et al. [12]. In this study, cyclic hardening or softening will be modeled through evolving both the isotropic hardening parameter R using Eqns. 11-13 and kinematic hardening rule parameter γ_i using the rate equations in Eqns. 19-22. Note in Eqns. 19 that similar to the case of isotropic hardening a superposition of two hardening parameters was used. It was demonstrated in Chapter 2 that cyclic hardening or softening of alloy 617 can be strain-range dependent also. Hence, with this modeling scheme both cyclic hardening/softening and strain-range dependence can be considered. Strain range dependence is incorporated into the model by making the saturated values of γ_i, γ_i^{st} to be a function of the radius of the plastic strain memory surface (q_{sr}) as shown in Eqns. 22 and 23.

$$\gamma_i = \gamma_{ini,i} + \gamma_{1,i} + \gamma_{2,i} \quad \text{..... (19)}$$

$$\dot{\gamma}_{1,i} = D_{\gamma_{1,i}} \left(\gamma_{1,i}^{st}(q_{sr}) - \gamma_{1,i} \right) \dot{p} \quad \text{..... (20)}$$

$$\dot{\gamma}_{2,i} = D_{\gamma_{2,i}} \left(\gamma_{2,i}^{st}(q_{sr}) - \gamma_{2,i} \right) \dot{p} \quad \text{..... (21)}$$

$$\gamma_{1,i}{}^{st}\left(q_{sr}\right) = a_{\gamma_{1,i}} + b_{\gamma_{1,i}} e^{-c_{\gamma_{1,i}} q_{sr}} \quad \text{..... (22)}$$

$$\gamma_{2,i}{}^{st}\left(q_{sr}\right) = a_{\gamma_{2,i}} + b_{\gamma_{2,i}} e^{-c_{\gamma_{2,i}} q_{sr}} \quad \text{..... (23)}$$

3. Numerical Implementation of the Model

3.1 Elastic Update

The numerical implementation of the model follows the strain-driven, implicit, radial return scheme. One begins first with the fundamental relationship of the generalized 3D Hooke's Law. Again, isotropic behavior was assumed therefore the stiffness matrix, *E*, can be defined by just two material constants, in this case, the bulk and the shear moduli. The full definition can be seen in Appendix Eqn. A1-2. It is also emphasized that the vectorized forms of the stress and strain tensors were used to reduce the number of calculations required, in which case care must be taken when calculating the tensorial dot product; this specificity is outlined in Appendix A.3. After the stiffness relation has been defined (Eqn. 24), both $\underline{\sigma}_{n+1}$ and $\underline{\varepsilon}^{e}_{n+1}$ are subdivided into their previous n-th component and the increment required to reach the n+1-th (Eqn. 25), which yields the n+1-th component as in Eqn. 26. Using additive strain decomposition (Eqn. 1), the elastic strain increment can be replaced by the difference between the total strain and plastic strain increment (Eqn. 27). However, as shown in the Appendix A.2. The product of the elastic stiffness tensor and the plastic strain increment can be simplified to just $2G\Delta\underline{\varepsilon}^{in}_{n+1}$ yielding Eqn. 28.

$$\underline{\sigma}_{n+1} = \underline{\underline{E}}\,\underline{\varepsilon}^{e}_{n+1} \quad \text{..... (24)}$$

$$\underline{\sigma}_{n} + \Delta\underline{\sigma}_{n+1} = \underline{\underline{E}}\left(\underline{\varepsilon}^{e}_{n} + \Delta\underline{\varepsilon}^{e}_{n+1}\right) \quad \text{..... (25)}$$

$$\Delta\underline{\sigma}_{n+1} = \underline{\underline{E}}\,\Delta\underline{\varepsilon}^{e}_{n+1} \quad \text{..... (26)}$$

$$\Delta\underline{\sigma}_{n+1} = \underline{\underline{E}}\left(\Delta\underline{\varepsilon}_{n+1} - \Delta\underline{\varepsilon}^{in}_{n+1}\right) \quad \text{..... (27)}$$

$$\Delta\underline{\sigma}_{n+1} = \underline{\underline{E}}\Delta\underline{\varepsilon}_{n+1} - 2G\Delta\underline{\varepsilon}^{in}_{n+1} \quad \text{..... (28)}$$

With the incremental stress tensor defined, it is now necessary to verify whether the new stress increment exists within the yield surface or not. Thus a trial stress increment and trail stress is defined as depicted in Eqns. 29 and 30. If the trial stress exists within or just on the yield surface, that is if the yield criterion, Eqn. 31, is less than or equal to zero, the plastic strain increment is zero and hence the trial stress is equivalent to the actual stress increment.

$$\Delta\underline{\sigma}^{tr}_{n+1} = \underline{\underline{E}}\Delta\underline{\varepsilon}_{n+1} \quad \text{..... (29)}$$

$$\underline{\sigma}^{tr}_{n+1} = \underline{\sigma}_{n+1} + \Delta\underline{\sigma}^{tr}_{n+1} \quad \text{..... (30)}$$

$$J\left(\underline{\sigma}^{tr}_{n+1} - \underline{\alpha}_{n+1}\right) = \sqrt{\frac{3}{2}\left(\underline{s}^{tr}_{n+1} - \underline{a}_{n+1}\right) : \left(\underline{s}^{tr}_{n+1} - \underline{a}_{n+1}\right)} \leq 0 \quad \text{..... (31)}$$

However, before the yield criterion can be evaluated $\underline{a}_{n+1,i}$ needs to be calculated. This is done assuming an elastic increment. With this assumption the equation for the back stress update reduces to Eqn. 32. Manipulating Eqn. 32 one can see that the update of the back stress can be expressed explicitly as a function of $J_{n+1,i}$; $J_{n+1,i}$ is defined by Eqn. 34. Expressing $\underline{a}_{n+1,i}$ in this fashion reduced the total number of equations that will be used in the Newton-Raphson update. Substituting Eqn. 33 into Eqn. 34 yields with some manipulation the zero-form for the update of $J_{n+1,i}$. $J_{n+1,i}$ can then be found by using the Newton-Raphson update procedure outline in Section 3.2.5.

$$\underline{a}_{n+1,i} - \underline{a}_{n,i} = -b_i J\left(\underline{a}_{n+1,i}\right)^{r_i - 1} \underline{a}_{n+1,i} \quad \text{..... (32)}$$

$$\underline{a}_{n+1,i} = \frac{\underline{a}_{n,i}}{1 + b_i J^{r_i - 1}_{n+1}} \quad \text{..... (33)}$$

$$J^{r_i - 1}_{n+1} = \sqrt{\frac{3}{2}\underline{a}_{n+1,i} : \underline{a}_{n+1,i}} \quad \text{..... (34)}$$

$$\Omega(J_{n+1,i}) = J_{n+1,i} - \sqrt{\frac{3}{2}\left(\frac{\underline{a}_{n,i}}{1 + b_i J^{r_i - 1}_{n+1,i}}\right) : \left(\frac{\underline{a}_{n,i}}{1 + b_i J^{r_i - 1}_{n+1,i}}\right)} \quad \text{..... (36)}$$

After updating $\underline{a}_{n+1,i}$, if it is found that the current stress point is within the yield surface, the updated stress and strain values, $\underline{\sigma}_{n+1}$ and $\underline{\varepsilon}_{n+1}$, can be defined by Eqns. 37 and 38 respectively. Not that if it is found to be a plastic increment $\underline{a}_{n+1,i}$ will have to be recalculated.

$$\underline{\sigma}_{n+1} = \underline{\sigma}_n + \Delta\underline{\sigma}^{tr}_{n+1} \quad \text{..... (37)}$$

$$\underline{\varepsilon}_{n+1} = \underline{\varepsilon}_n + \Delta\underline{\varepsilon}_{n+1} \quad \text{..... (38)}$$

If a portion of the trial stress exists outside the yield surface, that is if the yield criterion is greater than zero, then it is known that n+1-th strain increment will be composed of both elastic and a plastic component; therefore, Eqn. 37 will be no longer valid and is replaced by Eqn. 39. This equation can then be converted into deviatoric space (Eqn. 40) as it will be needed later on. Since not all strain increments are known prior to each loading step Eqns. 39 and 40 are not exactly correct. An additional term is required in either case to account for this as shown in Eqns. 41 and 42. The derivation and definition of each of the additional terms are defined in Appendix A.4.

$$\underline{\sigma}_{n+1} = \underline{\sigma}_n + \Delta\underline{\sigma}^{tr}_{n+1} - 2G\Delta\underline{\varepsilon}^{in}_{n+1} = \underline{\sigma}^{tr}_{n+1} - 2G\Delta\underline{\varepsilon}^{in}_{n+1} \quad \text{..... (39)}$$

$$\underline{s}_{n+1} = \underline{s}_n + \Delta\underline{s}^{tr}_{n+1} - 2G\Delta\underline{\varepsilon}^{in}_{n+1} = \underline{s}^{tr}_{n+1} - 2G\Delta\underline{\varepsilon}^{in}_{n+1} \quad \text{..... (40)}$$

$$\underline{\sigma}_{n+1} = \underline{\sigma}^{tr}_{n+1} - 2G\Delta\underline{\varepsilon}^{in}_{n+1} + \Delta p\underline{y}_{n+1} \quad \text{..... (41)}$$

$$\underline{s}_{n+1} = \underline{s}^{tr}_{n+1} - 2G\Delta\underline{\varepsilon}^{in}_{n+1} + \Delta p\underline{x}_{n+1} \quad \text{..... (42)}$$

3.2 Plastic strain update

3.2.1 Identification of unknowns

In order to find the updated stress tensor it is now necessary to find the plastic strain increment defined in Eqn. 5 for the current loading step. This requires that the unknown variables $\dot{p}_{n+1}$, $\underline{a}_{n+1}$, and $\underline{s}_{n+1}$ be found. Since there does not exist an easily formulated expression for $\underline{s}_{n+1}$ a more convenient term can be defined as seen in Eqn. 43. This term, $\underline{q}_{n+1}$,

is referred to as the kinematic radial distance. The deviatoric stress can be further be replaced by Eqn. 42 yielding the more useful form of Eqn. 44.

$$\underline{q}_{n+1} = \underline{s}_{n+1} - \underline{a}_{n+1} \quad \text{..... (43)}$$

$$\underline{q}_{n+1} = \underline{s}^{tr}_{n+1} - 2G\Delta\underline{\varepsilon}^{in}_{n+1} - \underline{a}_{n+1} + \Delta p\underline{x}_{n+1} \quad \text{..... (44)}$$

3.2.2 Development of zero-form function for back stress update

It turns out that the vector $\underline{a}_{n+1,i}$ can be expressed in terms of a scalar value $J_{n+1,i}$. This idea was first suggested by Kullig and Wippler [13] and serves to increase the efficiency of the back stress update by reducing the total number of equations. To accomplish this, one begins with the expression for the individual back stress update as shown in Eqn. 45. Next Eqn. 45 is multiplied by the time increment and then the incremental inelastic strain is replaced by Eqn. 5 yielding Eqn. 46. With some algebraic manipulation an expression for $\underline{a}_{n+1,i}$ is arrived at as seen in Eqn. 47. Note that $J_{n+1,i}$ is defined in Eqn. 48 and Eqn. 49 represents a simplifying substitution. Eqn. 47 now represents the explicit update of $\underline{a}_{n+1,i}$ as a function of the scalar value $J_{n+1,i}$; however, $J_{n+1,i}$ is still unknown. To update it the Newton-Raphson method will be used and thus the zero-form function must be developed. This is done by simply substituting Eqn. 47 into Eqn. 48. The zero-form function Ω for the update of $J_{n+1,i}$ is now expressed as Eqn. 50.

$$\frac{\underline{a}_{n+1,i} - \underline{a}_{n,i}}{\Delta t} = \frac{2}{3}C_i\frac{\Delta\varepsilon^{in}_{n+1}}{\Delta t} - \gamma\underline{a}_{n+1,i}\frac{\Delta p}{\Delta t} - b_i J\left(a_{n+1,i}\right)^{r_i-1}a_{n+1,i} \quad \text{..... (45)}$$

$$\underline{a}_{n+1,i} - \underline{a}_{n,i} = C_i\Delta p\frac{\underline{q}_{n+1}}{J\left(q_{n+1}\right)} - \gamma_i a_{n+1,i}\Delta p - b_i\Delta t J\left(\underline{a}_{n+1,i}\right)^{r_i-1}\underline{a}_{n+1,i} \quad \text{..... (46)}$$

$$\underline{a}_{n+1,i} = \frac{\underline{a}_{n,i} + C_i\Delta p\dfrac{\underline{q}_{n+1}}{J\left(\underline{q}_{n+1}\right)}}{\left(1+\gamma_i\Delta p + b_i\Delta t J_{n+1,i}{}^{r_i-1}\right)} = w_i\left(\underline{a}_{n,i} + C_i\Delta p\frac{\underline{q}_{n+1}}{J\left(\underline{q}_{n+1}\right)}\right) \quad \text{..... (47)}$$

$$J_{n+1,i} = \left(\frac{3}{2}\underline{a}_{n+1,i} : \underline{a}_{n+1,i}\right)^{\frac{1}{2}} \quad \text{..... (48)}$$

$$w_i = 1 + \gamma_i \Delta p + b_i \Delta t J_{n+1,i}^{\,r_i - 1} \quad \text{..... (49)}$$

$$\Omega\left(J_{n+1,i}\right) = J_{n+1,i} - w_i \left(\frac{3}{2} \left[\underline{a}_{n,i} + C_i \Delta p \frac{\underline{q}_{n+1}}{J\left(\underline{q}_{n+1}\right)} \right] : \left[\underline{a}_{n,i} + C_i \Delta p \frac{\underline{q}_{n+1}}{J\left(\underline{q}_{n+1}\right)} \right] \right)^{\frac{1}{2}} \quad \text{..... (50)}$$

3.2.3 Development of zero-form function for kinematic radial distance

Similar to $J_{n+1,i}$, in order to update $\underline{q}_{n+1}$ the Newton-Raphson method was used. To develop the zero-form function for this variable one begins with the definition of $\underline{q}_{n+1}$ as shown in Eqn. 44. Then combining Eqn. 44 and Eqn. 9 one arrives at Eqn. 51. Next Eqn. 5 is used to replace the incremental plastic strain and Eqn. 47 is used to replace $\underline{a}_{n+1,i}$ yielding Eqn. 52. With some algebraic manipulation the zero-from function F can be expressed as Eqn. 53.

$$\underline{q}_{n+1} = \underline{s}_{n+1}^{tr} - 2G\Delta\underline{\varepsilon}_{n+1}^{in} - \sum_{i=1}^{4} \underline{a}_{n+1,i} + \Delta p \underline{x}_{n+1} \quad \text{..... (51)}$$

$$\underline{q}_{n+1} = \underline{s}_{n+1}^{tr} - 3G\Delta p \frac{\underline{q}_{n+1}}{J\left(\underline{q}_{n+1}\right)} - \sum_{i=1}^{4} w_i \left(\underline{a}_n + C_i \Delta p \frac{\underline{q}_{n+1}}{J\left(\underline{q}_{n+1}\right)} \right) + \Delta p \underline{x}_{n+1} \quad \text{..... (52)}$$

$$F\left(\underline{q}_{n+1}\right) = \underline{q}_{n+1} + \left(3G\Delta p + \sum_{i=1}^{4} C_i w_i \Delta p \right) \frac{\underline{q}_{n+1}}{J\left(\underline{q}_{n+1}\right)} - \underline{s}_{n+1}^{tr} + \sum_{i=1}^{4} w_i \underline{a}_n - \Delta p \underline{x}_{n+1} \quad \text{..... (53)}$$

3.2.4 Development of zero-form function for incremental plastic strain

To update $\dot{p}$ its zero-form function needs to be developed, or rather the zero-form function for Δp since the time increment is known. Again one starts with the definition of $\dot{p}$ as shown in Eqn. 54; note the absence of the McCauley bracket as it is known that plastic strain increment will be greater than zero. Manipulating Eqn. 54 it can be re-expressed as Eqn. 55. As the right hand side of this equation is already of function of Δp the left hand side must now be manipulated to be a function of Δp by itself. To accomplish this first $\underline{q}_{n+1}$ must be expressed as a function of Δp. This is done by rearranging Eqn. 52 such that only $\underline{q}_{n+1}$ is

on the left hand side as shown in Eqn. 56. However $\underline{q}_{n+1}$ has not been completely moved to the left hand side; it still exists in J($\underline{q}_{n+1}$). To eliminate it completely one begins with the definition of J($\underline{q}_{n+1}$) and then inserts the expression for $\underline{q}_{n+1}$ just developed to obtain Eqn. 57. Rearranging Eqn. 57 and reinserting the expression for $\phi_{n+1}(\Delta p)$ one arrives at Eqn. 58. Multiplying through by the denominator Eqn. 58 can be re-expressed as Eqn. 59. Now the dependence on $\underline{q}_{n+1}$ can be eliminated by substituting the second definition of $J(\underline{q}_{n+1})$, Eqn. 55, into Eqn. 59. Then with only a slight rearrangement of the expression the zero-form function can be expressed as seen in Eqn. 60.

$$\frac{\Delta p_{n+1}}{\Delta t_{n+1}} = \left(\frac{J\left(\underline{\sigma}_{n+1} - \underline{\alpha}_{n+1}\right) - \sigma_o - R}{K} \right)^n \quad \text{..... (54)}$$

$$J\left(\underline{\sigma}_{n+1} - \underline{\alpha}_{n+1}\right) = J\left(q_{n+1}\right) = K\left(\frac{\Delta p_{n+1}}{\Delta t_{n+1}} \right)^{\frac{1}{n}} + \sigma_o + R \quad \text{..... (55)}$$

$$\underline{q}_{n+1} = \frac{\underline{S}^{tr}_{n+1} - \sum_{i=1}^{4} w_i \underline{a}_{n,i} + \Delta p \underline{x}_{n+1}}{\left(1 + \frac{\Delta p_{n+1}}{J\left(q_{n+1}\right)} \left[\sum_{i=1}^{4} w_i C_i + 3G \right] \right)} = \frac{Z_{n+1}}{\phi_{n+1}\left(\Delta p\right)} \quad \text{..... (56)}$$

$$J\left(q_{n+1}\right) = \left(\frac{3}{2} \underline{q}_{n+1} : \underline{q}_{n+1} \right)^{\frac{1}{2}} = \left(\frac{3}{2} \frac{Z_{n+1}}{\phi_{n+1}\left(\Delta p\right)} : \frac{Z_{n+1}}{\phi_{n+1}\left(\Delta p\right)} \right)^{\frac{1}{2}} \quad \text{..... (57)}$$

$$J\left(q_{n+1}\right) = \frac{\left(\frac{3}{2} Z_{n+1} : Z_{n+1} \right)^{\frac{1}{2}}}{\left(1 + \frac{\Delta p_{n+1}}{J\left(q_{n+1}\right)} \left[\sum_{i=1}^{4} w_i C_i + 3G \right] \right)} \quad \text{..... (58)}$$

$$J\left(q_{n+1}\right) + \Delta p_{n+1} \left[\sum_{i=1}^{4} w_i C_i + 3G \right] = \left(\frac{3}{2} Z_{n+1} : Z_{n+1} \right)^{\frac{1}{2}} \quad \text{..... (59)}$$

$$L\left(\Delta p\right) = K\left(\frac{\Delta p_{n+1}}{\Delta t_{n+1}} \right)^{\frac{1}{n}} + \sigma_o + R + \Delta p_{n+1} \left[\sum_{i=1}^{4} w_i C_i + 3G \right] - \left(\frac{3}{2} Z_{n+1} : Z_{n+1} \right)^{\frac{1}{2}} \quad \text{..... (60)}$$

3.2.5 Convergence of unknowns

One may have remarked that the zero-form functions for the update of $\underline{q}_{n+1}$ and J_{n+1} are not independent of each other. That is to say that the zero-form update of $\underline{q}_{n+1}$ is a function of J_{n+1} and vice versa. In addition, the zero-form for both $\underline{q}_{n+1}$ and J_{n+1} are a function of Δp. Therefore each variable cannot be updated independently from one another. Thus the technique utilized by Ahmed [14] will be used for the update of each of the three variables. This approach uses two loops, one nested inside the other and can be visualized through the flow charts shown in Fig. 1.

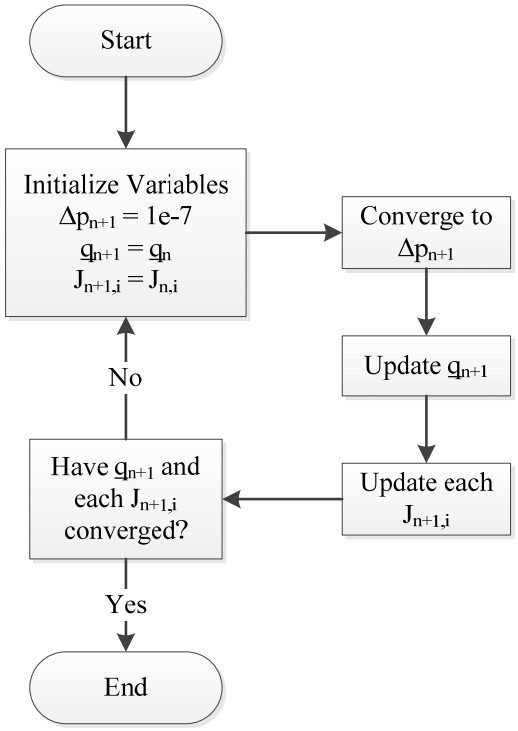

Fig. 1: Unknown variable update routine.

In this approach Δp_{n+1} is converged to inside the $\underline{q}_{n+1}$ $J_{n+1,i}$ convergence loop based on the initial assumptions of $\underline{q}_{n+1}$ and $J_{n+1,i}$. With a converged value of Δp_{n+1} found, $\underline{q}_{n+1}$ and then each J_{n+1} are updated. Then the convergence of both $\underline{q}_{n+1}$ and $J_{n+1,i}$ are checked. If all of the variable have converged then the routine is exited; otherwise, the updated values of

Δp_{n+1}, $\underline{q}_{n+1}$, and $J_{n+1,i}$ are used as the initial values for each of the respective variable in the next iteration.

3.2.6 Newton-Raphson method

The Newton-Rahpson method was implemented in the following fashion. First an initial assumption for the unknown variable is made, Eqn. 61, where $\underline{\lambda}$ is a general unknown variable. Next an updated approximation of $\underline{\lambda}$ made using Eqn. 62. This process is repeated until convergence is reached; that is to say when the tolerance, as defined by Eqn. 63, is less than a given value. In this investigation a tolerance of 1e-5 was found to be satisfactory.

$$\underline{\lambda}_{n+1}^{k} = \underline{\lambda}_{initial} \quad \text{..... (61)}$$

$$\underline{\lambda}_{n+1}^{k+1} = \underline{\lambda}_{n+1}^{k} - \left[\Lambda'\left(\underline{\lambda}_{n+1}^{k}\right) \right]^{-1} \Lambda\left(\underline{\lambda}_{n+1}^{k}\right) \quad \text{..... (62)}$$

$$tol = \left| 1 - \frac{\left\| \underline{\lambda}_{n+1}^{k} \right\|}{\left\| \underline{\lambda}_{n+1}^{k+1} \right\|} \right| \quad \text{..... (63)}$$

Note that sometimes Δp_{n+1}^{k+1} will be less than zero during the convergence routine. Since Δp cannot be less than zero, if Δp_{n+1}^{k+1} was found to be less than zero during the convergence routine a new estimate was made as negative one tenth of the current value (negative so that the new estimate will be positive). This allowed for the avoidance of non-convergence during the update of Δp. Also, as $J_{n+1,i}$ should be positive, if a similar problem occurred, it was avoided in the same fashion.

3.2.7 Update of Stress and Strain

With Δp, $\underline{q}_{n+1}$, and $J_{n+1,i}$ converged the updated stresses and strain can now be found. The new strain increment can be found in accordance with Eqn. 5. Next the new updated strain can be found using Eqn. 41 with the correction term modification.

3.2.8 Strain range dependence

With the updated value of the inelastic strain known the strain memory surface can be updated. This is done similarly to the update of the inelastic strain. The two equations that govern the update of the strain memory surface variables q_{sr} and $\underline{Y}$ are Eqns. 15 and 16. So beginning in the same manner as the update of the previous unknown variables, the zero-form functions for both q_{sr} and $\underline{Y}$ will be developed. Discretizing Eqn. 15 yields Eqn. 64. With a slight modification of Eqn. 64 yields the zero-form Eqn. 65. Next Eqn. 16 is discretized yielding Eqn. 66. Again with a slight modification the zero-from function $\underline{Y}_{n+1}$ can be found (Eqn. 67).

$$\underline{q}^{sr}_{n+1} - \underline{q}^{sr}_{n} = \eta\left(\underline{n}_{n+1} : \underline{n}^{*}_{n+1}\right)\Delta p_{n+1} \quad \text{..... (64)}$$

$$F_1\left(\underline{q}^{sr}_{n+1}\right) = \underline{q}^{sr}_{n+1} - \underline{q}^{sr}_{n} - \eta\left(\underline{n} : \underline{n}^{*}\right)\Delta p \quad \text{..... (65)}$$

$$\underline{Y}_{n+1} - \underline{Y}_{n} = \sqrt{\frac{3}{2}}\left(1-\eta\right)\left(\underline{n}_{n+1} : \underline{n}^{*}_{n+1}\right)\Delta p \quad \text{..... (66)}$$

$$F_2\left(\underline{Y}_{n+1}\right) = \underline{Y}_{n+1} - \underline{Y}_{n} - \sqrt{\frac{3}{2}}\left(1-\eta\right)\left(\underline{n}_{n+1} : \underline{n}^{*}_{n+1}\right)\Delta p \quad \text{..... (67)}$$

3.2.9 Newton-Raphson method for the update of strain range dependence variables

Unlike for the update of Δp, $\underline{q}_{n+1}$, and $J_{n+1,i}$ the multivariate form of the Newton-Raphson method was used to update both the q_{sr} and $\underline{Y}$. Like for the case of the previous set of unknown variables the zero-form function for each variable are functions of multiple variables. However it was found that in this case the multivariate form of the Newton-Raphson method provided a more stable update to the strain memory surface variables thereby motivating the use of the more costly update procedure. To use this update method first a vector of the initial values for both variables is set as seen in Eqn. 68. Then the updated value is found by using the product of the inverse of the Jacobian for both zero form functions times the combined zero-form function as shown in Eqn. 69. The combined zero-form function as wells as the Jacobian are given in Eqns. 70 and 71 respectively. Lastly, the tolerance for each individual is calculated as shown in Eqn. 72.

$$\underline{\lambda}_{n+1}^{k} = \left[\underline{\lambda}_{n+1,1}^{k} \quad \underline{\lambda}_{n+1,2}^{k} \right]^{T} = \left[\underline{\lambda}_{initial,1}^{k} \quad \underline{\lambda}_{initial,2}^{k} \right]^{T} \quad \text{..... (68)}$$

$$\underline{\lambda}_{n+1}^{k+1} = \underline{\lambda}_{n+1}^{k} - J_f^{-1}(\underline{\lambda}_{n+1}^{k}) F(\underline{\lambda}_{n+1}^{k}) \quad \text{..... (69)}$$

$$F = \left[\underline{F}_1 \quad \underline{F}_2 \right]^{T} \quad \text{..... (70)}$$

$$J_f = \begin{bmatrix} \dfrac{\partial \underline{F}_1}{\partial \underline{\lambda}_{n+1,1}^{k}} & \dfrac{\partial \underline{F}_1}{\partial \underline{\lambda}_{n+1,2}^{k}} \\ \dfrac{\partial \underline{F}_2}{\partial \underline{\lambda}_{n+1,1}^{k}} & \dfrac{\partial \underline{F}_2}{\partial \underline{\lambda}_{n+1,2}^{k}} \end{bmatrix} \quad \text{..... (71)}$$

$$tol_i = \left| 1 - \frac{\left\| \underline{\lambda}_{n+1,i}^{k} \right\|}{\left\| \underline{\lambda}_{n+1,i}^{k+1} \right\|} \right| \quad \text{..... (72)}$$

3.2.10 Isotropic Cyclic Hardening or Softening

Isotropic hardening was implemented after the update of the strain-memory surface. The expressions governing the update of the isotropic hardening variable R are given in Eqns. 11-13. As is visible in Eqns. 12 and 13 the rate form of the equation can be integrated. The integrated forms of Eqns. 12 and 13 are given in Eqns. 73 and 74. Note that Eqn. 11 still applies and the total isotropic hardening terms is the sum of each individual term.

$$R_1 = R_1^{st} \left(1 - e^{-b_{r1} p} \right) \quad \text{..... (73)}$$

$$R_2 = R_2^{st} \left(1 - e^{-b_{r2} p} \right) \quad \text{..... (74)}$$

3.2.11 Kinematic Cyclic Hardening or Softening

The update of the back stress variable γ_i was done last. Here, as opposed to the isotropic cyclic hardening update, γ_i was not updated using an integrated form. This was done as integration was not possible since γ_i^{st} is dependent on the radius of the strain memory surface q_{sr}; therefore, an explicit update of γ_i was used. In order to update γ_i the saturation value, , must be updated. This is governed by Eqns. 22 and 23 for the first and second hardening rules respectively. Once the updated value of γ_i^{st} has been calculated the $\gamma_{i,1}$ and $\gamma_{i,2}$ can be update using the discretized forms of Eqns. 20 and 21 given by Eqns. 65 and 76.

Once the new value for $\gamma_{i,1}$ and $\gamma_{i,2}$ are calculated the new value for γ_i can be calculated in accordance with Eqn. 19. With the update of γ_i now completed the next iteration can begin. The processes outlined in sections 3.1 and 3.2, 3.1 for the update of an elastic increment and 3.2 for the update of a plastic increment, can be used for each of the remaining iterations.

$$\gamma_{i,1}^{n+1} = \gamma_{i,1}^{n} + D_{\gamma,1}\left(\gamma_1^{st} - \gamma_{i,1}^{n}\right)\Delta p_{n+1} \quad \text{..... (75)}$$

$$\gamma_{i,2}^{n+1} = \gamma_{i,2}^{n} + D_{\gamma,2}\left(\gamma_2^{st} - \gamma_{i,2}^{n}\right)\Delta p_{n+1} \quad \text{..... (76)}$$

3.3 Precaution when using the Newton-Raphson update

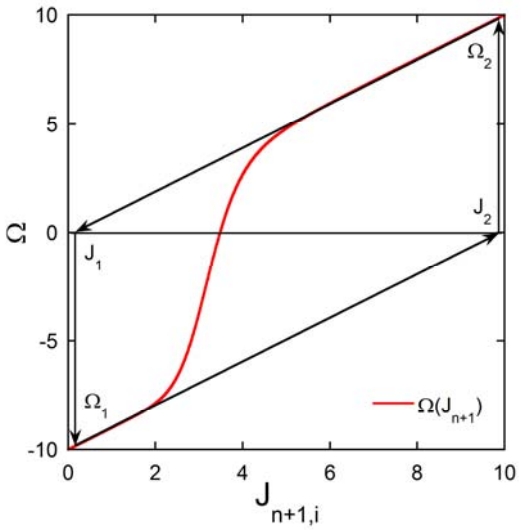

Fig. 2: Original zero-form function for J_{n+1} update.

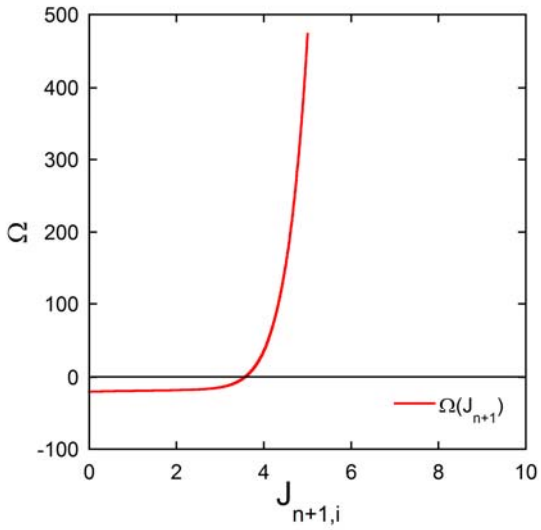

Fig. 3: Improved zero-form function for J_{n+1} update.

$$\Omega\left(J_{n+1,i}\right) = J_{n+1,i} - \frac{A}{1+\gamma_i\Delta p + b_i\Delta t J_{n+1,i}^{r_i-1}} = 0 \quad \text{..... (77)}$$

$$\Omega\left(J_{n+1,i}\right) = \left(1+\gamma_i\Delta p\right)J_{n+1,i} + b_i\Delta t J_{n+1,i}^{r_i} - A = 0 \quad \text{..... (78)}$$

While the Newton-Raphson method is often an excellent method to find the root of a nonlinear equation there are certain peculiarities that must be take into account to ensure proper convergence. In particular, the shape of the zero-form function plays a large role in determining whether a root can be found given a certain initial guess. In the course of this

research a particular example perfectly illustrates this point. Eqn. 45 shows the zero-form function for the update of $J_{n+1,i}$. With this form, however, convergence cannot be guaranteed using the Newton-Raphson method. This is illustrated clearly in Fig. 2. Equation 77 is a snapshot of the zero-form function. An initial guess of J_1 is made yielding $\Omega(J_1) = \Omega_1$. Graphically, the updated value of J_2 using the Newton-Raphson method can be found by tracing the tangent at Ω_1 until it intersects the J-axis. This evaluates to a value of Ω_2 which then yields J_1 again as the updated predicted root. Thus it has been shown that for the particular starting value of J_1, this zero-from function diverges by oscillation and will not converge under these conditions. To remedy this situation a small fix can be made, namely, multiplying through by the denominator of the second expression in the Eqn. 77. This yields Eqn. 78, which is plotted in Fig. 3. Thus it can be seen that this slight modification has led to a major improvement in the convergence properties of the function. It is therefore cautioned that the functional response of the zero-form function is of critical importance in determining whether the Newton-Raphson scheme is a suitable convergence algorithm. And that minor mathematical manipulations can lead to improved convergence properties of the function.

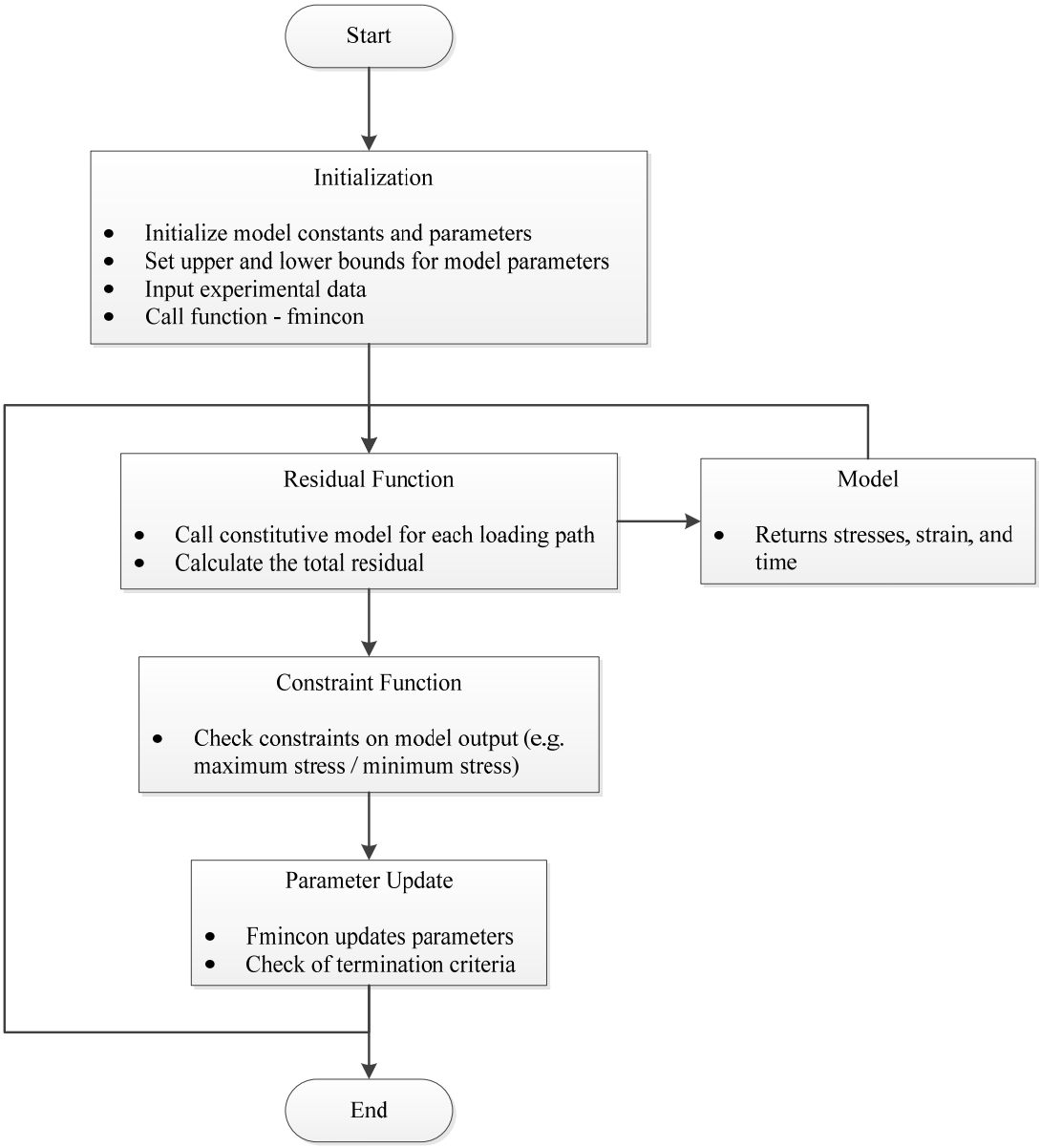

Fig. 4: Flow chart for parameter optimization routine.

4. Parameter determination

4.1 Optimization routine

As mentioned previously, a non-linear minimization routine was implemented in Matlab using the Matlab function fmincon at its core. This function has the benefit of allowing for the minimization of a nonlinear function, e.g. the constitutive model, to be constrained under various bounds. In the previous section the nonlinear optimization routine was mentioned only vaguely. It is the goal of this portion of the paper to outline how the

optimization routine was used and to share some useful experiences in terms of converging to useful set of parameters.

Fig. 4 depicts a flow chart of the logic behind the optimization scheme. The basis for this framework was to develop a code that could be flexibly expanded to accommodate multiple experimental responses. To begin with parameters to be optimized were chosen and appropriate upper and lower bounds were set. Next, pertinent experimental responses were imported. Then the optimization function fmincon was called.

In the optimization loop, the residual function in called first. Here for each experimental response the constitutive model is called to provide the simulated stress, strain and time responses. A stress residual is then calculated as the absolute value between the experimental and model response. Finally, the total residual can be calculated in a flexible fashion such that only the experiments for which the shape is important can be included.

Next, the constraint function is called. In this function inequalities can be set to control a wide variety of model responses. In this work the constraint function was used to restrict the stress at either the peak tensile or compressive strain to either a minimum or maximum value based on need, the initial and final relaxed stress in a fatigue-creep experiment to a minimum or maximum value, and finally to restrict the kinematic hardening parameters C_i and γ_i such that C_i is greater than C_{i+1} and similarly for γ_i and γ_{i+1}. This last constraint was implemented to keep a more consistent variation of these parameters.

4.2 Initial estimate of back stress parameters C_i and γ_i

The parameter determination process can be split into five main categories: first, the determination of the elastic modulus E; second, the determination of the hysteresis shape parameters, C_i and γ_i, and the initial yield surface size, σ_o; third, the determination of the cyclic hardening or softening parameters $D_{\gamma i}$, γ_i^{st} and R; fourth, the determination of the static recovery parameters b_i and r_i; and fifth, the determination of the rate dependence parameters K and n. For temperatures for which no stress relaxation data is available the determination of static recovery parameters can be neglected. For temperatures that do not show rate dependence the fifth category of parameter determination can be ignored.

For the first step, the elastic modulus was determined by first finding the linear slope of the monotonic curve for a representative test at a given temperature. Then, a short

investigation was performed in which the variation of the elastic modulus between tests and between cycles in a given tests was analyzed. However, no significant variation of the elastic modulus was seen in this investigation; therefore, the elastic modulus was taken as the elastic modulus found in the representative tests.

For both rate-independent and rate-dependent modeling the next step in the parameter determination process is the determination of the kinematic parameters C_i and γ_i as well as the initial yield surface size σ_o. It is noted here that there often exists a large discrepancy between the monotonic and cyclic behavior in strain-controlled fatigue responses. This can be seen clearly in Fig. 5 which shows the monotonic, first down-going path, and first up-going path of a fatigue test performed at 650°C. The difference between the monotonic and cyclic response manifests itself in two ways; first, in general, the monotonic path will have a greater σ_o in comparison to either the first down-going or first up-going cyclic paths; second, there does not exist one set of kinematic hardening parameters that can describe both the monotonic and cyclic responses. Therefore, in this study, initial model parameters were determined from the first cyclic hysteresis loop and not the monotonic response in order to keep a greater degree of continuity between the experimental responses and the model predictions.

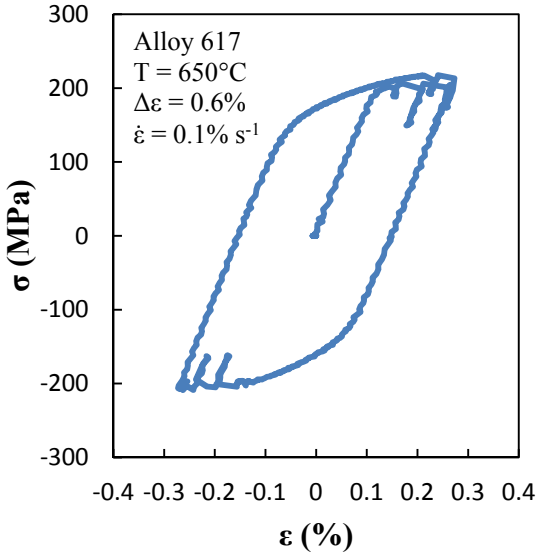

Fig. 5: Monotonic and first cycle hysteresis loop at 650°C

In order to establish a set of model parameters that best represents the material response, a code was developed based upon the Matlab function fmincon which utilizes nonlinear, gradient-based methods to minimize a prescribed residual function, in this case the residual between the simulated and experimental stress. However, in order for this routine to reach a reasonable solution initial estimates are required. These initial estimates were determined in two ways; first, σ_o was taken as half the linear region of the first down-going curve; second, the initial estimates for C_i and γ_i were made using the method outlined in Bari and Hassan [15]. In the rate dependent case without static recovery a closed form solution can be developed such that the peak stress can be related to the model by Eqns. 79 and 80 for the up-going and down-going paths respectively. Here ε_L^p is the minimum plastic strain of the up-going path and ε_H^p the maximum plastic strain of the down-going path. σ_x and ε_x^p are the experimental stress and plastic strain at the point in question. Equation 31 was adapted from Bari and Hassan [15]. Equation 31 is a modification of Eqn. 32 to account for the difference in integration limits for the down-going case.

$$\frac{C_1}{\gamma_1}+\frac{C_2}{\gamma_2}+\frac{C_3}{\gamma_3}+\frac{C_4}{2}\left(\varepsilon_x^p-\varepsilon_L^p\right)+\sigma_o=\sigma_x \quad \text{..... (79)}$$

$$\frac{C_1}{\gamma_1}+\frac{C_2}{\gamma_2}+\frac{C_3}{\gamma_3}+\frac{C_4}{2}\left(\varepsilon_H^p-\varepsilon_x^p\right)+\sigma_o=-\sigma_x \quad \text{..... (80)}$$

With these equations defined initial estimates can now be made. C_1 is assumed to be a large value, usually on the order of 10^7 with γ_1 approximately one order of magnitude lower such that this back stress saturates quickly. C_4 is taken as the slope of the experimental curve at the peak stress. The values of C_2 and C_3 are generally chosen as intermediate values between C_1 and C_4 with γ_2 and γ_3 found such that either Eqn. 31 or 32 is satisfied (whichever applies) and γ_2 is greater than γ_3. Once the initial estimates are completed the nonlinear solver is used to optimize the material parameters. This process was followed for the temperatures of 25°, 650°, and 750°C which were considered as rate independent as discussed in Chapter 2.

4.3 Initial estimate of rate dependence parameters K and n

For the temperatures of 850° and 950°C the parameter determination process becomes more complicated. At these temperatures it becomes necessary to include both the rate dependence and static recovery modeling features which allow for the simulation of a wider range of experimental responses. But, as will be shown, each of these features adds to the complexity of determining model parameters.

When considering only the rate dependence parameters K and n, two approaches can be taken for their determination. The first, based on a novel observation, will be explained first. To begin with, one starts with a typical hysteresis loop as shown in Fig. 6. Next the loop is converted into plastic strain space by removing the elastic strain component. This yields a hysteresis loop as shown in Fig. 7. Here is seen that, upon unloading, there is a period of time in which the plastic strain continues to increase despite decreasing total strain. This phenomenon is related to the creep experienced by the material at such a high temperature.

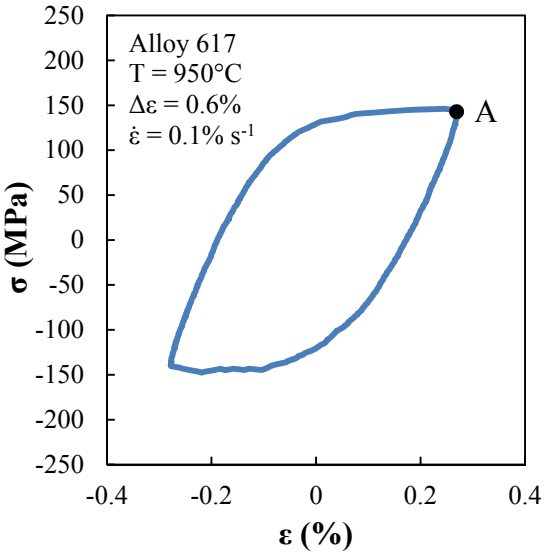

Fig. 6: Second cycle hysteresis loop at 950°C

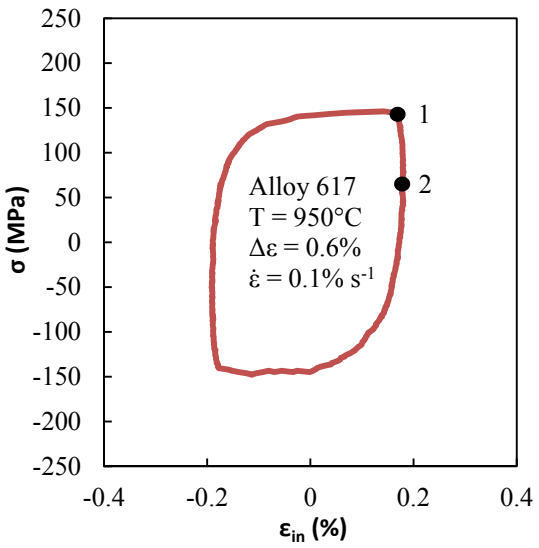

Fig. 7: Second cycle hysteresis loop at 950°C in plastic strain space

Excluding for the moment static recovery, a closed form expression of the model can be developed which includes the rate dependence terms K and n. This expression is shown in

Eqn. 81. In this case, saturation of all of the first three back stresses is assumed; however, it is possible to develop an expression without this assumption. At 950°C, no clear linear region was found in the experimental response, thus, σ_o was taken to be zero. This reduces Eqn. 81 to Eqn. 82. The expression σ_v in the subsequent equations represents the overstress or distance from the viscoplastic-potential surface during plastic loading to the Von-Mises yield surface. This quantity can also be expressed by equation 83 which is derived from Eqn. 6.

$$\frac{C_1}{\gamma_1}+\frac{C_2}{\gamma_2}+\frac{C_3}{\gamma_3}+\frac{C_4}{2}\left(\varepsilon_x^p-\varepsilon_L^p\right)+\sigma_v+\sigma_o=\sigma_x \quad \text{..... (81)}$$

$$\frac{C_1}{\gamma_1}+\frac{C_2}{\gamma_2}+\frac{C_3}{\gamma_3}+\frac{C_4}{2}\left(\varepsilon_x^p-\varepsilon_L^p\right)+\sigma_v=\sigma_x \quad \text{..... (82)}$$

$$\sigma_v=K\left(\frac{\Delta p}{\Delta t}\right)^{\frac{1}{n}} \quad \text{..... (83)}$$

With equations 82 and 83 now established a good estimate of the overstress can now be obtained from the experimental data. First, it is noted that at point 2, where plastic strain reaches a maximum, the plastic strain rate is zero. This yields that the overstress at this point will be zero. Second, it was previously assumed that the first three back stresses had saturated at point 1. It will be further assumed that a negligible increase will occur in the fourth linear back stress during unloading. It can now be shown that the overstress simply reduces to the difference between the stress at point 1 and the stress at point 2 as shown in Eqn. 84.

$$\sigma_v=\sigma_1-\sigma_2 \quad \text{..... (84)}$$

It is now recalled that the purpose of developing this approach is for the determination of the rate dependence parameters K and n. The next step in this approach it to find the overstress, σ_v, from a test performed at each experimental strain rate, in this case of the present work, at 0.1% s^{-1}, 0.04% s^{-1} and 0.01% s^{-1}. With the overstress determined for these rates only the plastic strain rate at point 1 for each strain rate test is left to be found. It is

cautioned that the plastic strain rate found directly from experimental data can often not be used directly in this regard due to noise. Thus the plastic strain rate can be approximated as the experimental strain rate for experiments with a relatively saturated response at point 1. With the overstress and corresponding plastic strain rate defined for each applicable strain rate, K and n can be found using a linear regression solver, such as solver in excel, which tries to reduce the residual between the overstress predicted by Eqn. 83 for a given plastic strain rate and the one found experimentally through the process outlined above.

Once K and n have been found, the back stress parameters C_i and γ_i can be found by using the hysteresis loop responses for one strain rate and the aforementioned nonlinear solve routine. In Figs. 8 and 9 the simulations that can be achieved using this approach are shown. In this case the higher strain rate test, performed at 0.1% s^{-1} was used for the determination of the C_i and γ_i parameters. Examining the figure one can see that this method of parameter determination can reasonably predict the range of responses for fatigue tests performed at different strain rates; however improvements can be made which will be outlined later.

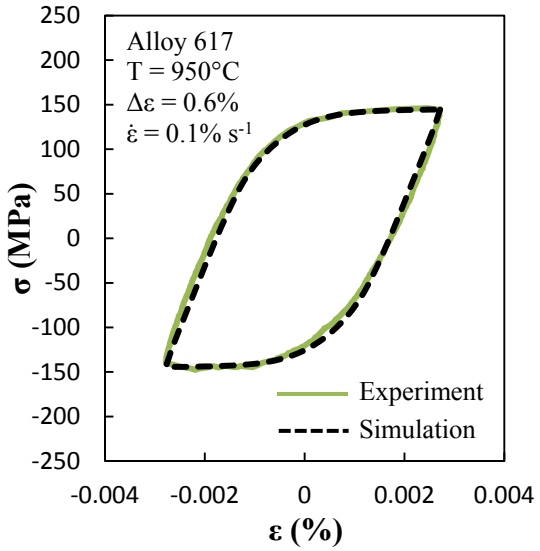

Fig 8: Simulation of second cycle hysteresis loop at 950°C at a strain rate of 0.1% s^{-1}

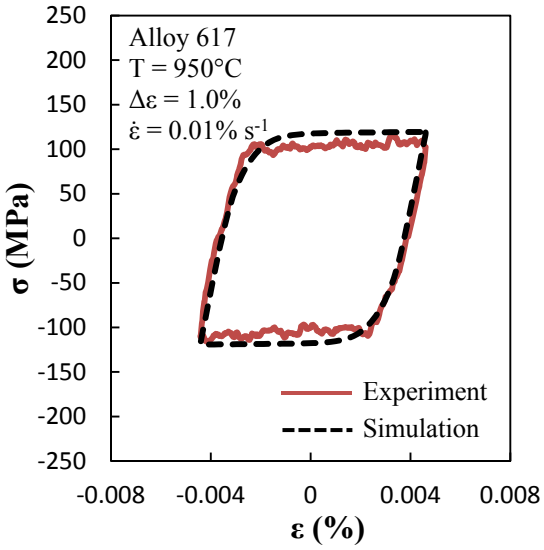

Fig 9: Simulation of second cycle hysteresis loop at 950°C at a strain rate of 0.01% s^{-1}

The small overprediction observed in Fig. 9 can be explained by a few facts. First, the precise location where the plastic strain rate changes direction is difficult to find from experimental data. As the plastic strain rate approaches zero the slope of the plastic strain versus stress curve approaches infinity. This coupled with experimental noise makes finding the exact inflection point of the plastic strain rate difficult to determine experimentally. This in turn can yield experimental predictions of the overstress that vary significantly. In addition, when determining the kinematic parameters C_i and γ_i it is assumed that for a given K and n there is an identical kinematic hardening behavior seen at all three rate; however, this is not the case. While this method of parameter determination is not precise enough for final model parameter determination it does give an initial estimate of K and n that can be used for an improved method which will be outlined subsequently.

4.4 Determination of static recovery parameters b_i and r_i / Finalization of 1st cycle parameters

For the determination of the static recovery parameters b_i and r_i a fatigue-creep test is needed in addition to the tests needed for the determination of C_i, γ_i, K, and n. In total then, for a given strain range, four experiments are required for the determination of model parameters: three fatigue tests performed at three separate rates, and one fatigue-creep test. It is noted that it is possible to reduce this number to three tests by using only two fatigue tests; however, the rate response would not be as well controlled.

In order to demonstrate the process an example case of 950°C will be used. Here the four experiments chosen are as follows: three fatigue tests performed at rates of 0.1% s^{-1}, 0.04 s^{-1}, and 0.01% s^{-1}, and one fatigue-creep test performed at a rate 0.1% s^{-1} with a 10 minute tensile strain hold. Each test was conducted at a strain range of 0.6% except for the fatigue test carried out at a strain rate of 0.01% s^{-1}. In general, it is suggested for the same strain range to be used in the parameter determination process; but, it has been observed that at 950°C no significant variation is seen in the hysteresis loop shape above a strain range of 0.6%. Therefore, since a fatigue test performed at the lowest strain rate was not available at a strain range of 0.6%, one conducted at a strain range of 1.0% was substituted in its place.

To begin with, an initial set of C_i and γ_i was determined from the highest-rate fatigue test treating the material as rate-independent for the time being. This gives an initial working

set of parameters for C_i and γ_i. Next, as was discussed in the previous section, K and n were determined using the overstress method utilizing the three fatigue experiments. Then, γ_i as well as K and n were re-optimized using the nonlinear optimization routine. In this case the residual was determined from only two tests, the fatigue tests performed at 0.1% s^{-1} and 0.04% s^{-1}, and not from the lower strain rate of 0.01% s^{-1}. This was chosen due to a discrepancy in hysteresis loop shape between the highest two rates and the lowest rate. However, to counteract the lack of information about the model fit in the residual function, the stress at the peak compressive strain of this experiment was constrained in the constraint function. As a side note, it is often a trial and error process to determine whether or not to constrain the amplitude to a maximum or minimum value. This depends on the tendency of the convergence algorithm to over or under predict the response when no constraint is applied.

Finally, a fatigue-creep test was added. Similar to the fatigue test performed at 0.01% s^{-1} a significant discrepancy in the hysteresis shape is seen between the fatigue and fatigue-creep tests; in this case due to the stress overshoot during strain reversal immediately after a peak strain hold. For this reason the residual was only calculated for the stresses during relaxation which is the most pertinent information for the static recovery terms. With this information in place, the optimization routine was run again to find an initial set of static recovery parameters. This initial set was found such that b_i and r_i are the same for each back stress. Note that in addition to optimizing for the static recovery terms γ_i, K, and n were also re-optimized. This step is important as the addition of the static recovery parameters can drastically change the hysteresis loop shape simulation. Thus, by reducing the number of parameters to optimize, a greater chance of success in finding an appropriate parameter set is found. Lastly, the optimization routine was run a final time, this time allowing for the static recovery parameters to vary for each back stress. This last run yields the full set of kinematic and rate dependent parameters for a given temperature at the initial cycle.

4.5 Determination of cyclic hardening parameters

When materials harden or soften two effects can be seen in the experimental response; first, either an increase or reduction in the yield surface is observed; second, shape change of hysteresis curves. For many years the shape change of hysteresis curves was

ignored and the cyclic hardening/softening responses of materials were only modeled through an increase or decrease in yield surface size. However, as discussed in Krishna and Hassan [12], this leads to poor predictions of the hysteresis loop shape in later cycles. To overcome this difficulty and improve cyclic hardening and softening simulations, the evolution of the kinematic hardening rule parameters γ_i suggested by Krishna and Hassan [12] was implemented in this work as presented in Section 2.

In terms of parameter determination, a relatively easy procedure can be followed for the determination of both the isotropic and kinematic hardening parameter evolutions. In the previous section the way in which the initial model parameters were determined was discussed in detail. Here model parameters were found from the first down-going and up-going curve after the monotonic cycle for every temperature except 950°C. At 950° the first stable cycle after the initial rapid softening seen was used. To find the cyclic hardening parameters a minimum of two additional cycles are needed when one cyclic hardening rule is used and four additional cycles are needed when two cyclic hardening rules are used. The last cycle chosen should be a cycle that captures the peak cyclic hardening i.e. a cycle before late stage cyclic softening is observed, such as for 750° and 850°C (see Chapter 2). The intermediate cycles should be cycles that well represent the shape of the stress amplitude response.

Once the representative cycles have been determined for a given experimental response a brief investigation should be conducted on whether or not cyclic hardening takes the form of isotropic yield surface expansion, an increase in the plastic modulus, or, likely, a combination of the two. In this investigation the latter always applied. With this ascertained the next step in the parameter determination process is to determine, for each cycle, a new set of σ_o, γ_i, or a combination of the two which best reflects the material response for each cycle. It should be noted at this point that these parameters are found as if the current cycle were an initial cycle.

Next a preliminary estimate of the accumulated plastic strain at each cycle needs to be found. As often one does have every hysteresis cycle recorded, a good way to accomplish this is to use the stress amplitude response data. The accumulated plastic strain for each cycle can be taken approximately as the twice hysteresis loop width. Note that the hysteresis loop width is a measure of the accumulated plastic strain for each half-cycle. Thus the total plastic

strain accumulation for one cycle would be twice the loop width. The hysteresis loop width can in turn be approximated by Eqn. 85.

$$\Delta p = \Delta\varepsilon - \frac{2\sigma_a}{E} \quad \text{..... (85)}$$

With σ_o, γ_i, and the accumulated plastic strain for each cycle now known the rates for the isotropic and kinematic hardening parameter evolutions as well as $\gamma_{i,\text{ini}}$ and R^{st} can be determined. For the determination of R^{st} and its rate b_r, first the R at each cycle needs to be determined; this is simply the σ_o for a given cycle minus the σ_o of the first cycle. With R determined for each cycle, the closed form solution for the isotropic hardening rule shown in Eqn. 86 can be used to fit the experimental data. With this equation, a regression solver such a solver in excel can be used to reduce the residual between to the experimental and simulated value or R to find both R^{st} and b_r for both rules. Since after the first monotonic path some plastic strain will have accumulated, in order to have a yield surface size equivalent to σ_o at the start of the first down-going path it is necessary to use σ_o as a parameter in addition to R_{st} and b_r. In this case the initial state of the σ_o parameter will be slightly lower than that of the σ_o found experimentally from the first cycle.

$$R = R_1^{st}\left(1 - e^{-b_{r1}p}\right) + R_2^{st}\left(1 - e^{-b_{r2}p}\right) \quad \text{..... (86)}$$

In a similar fashion, a generalized closed from solution can be found for γ_i as a function of accumulated plastic strain as depicted in Eqn. 87. This can then be used to compare the experimental variation of γ_i versus the current model and used a regression solver to find the parameter of $\gamma_{i,\text{ini}}$ as wells as γ^{st}, and D_γ for both rules. Again, $\gamma_{i,\text{ini}}$ will be slightly higher than the γ_i found for the first cycle as there will be a small degree of plastic strain accumulation during the monotonic path.

$$\gamma_i = \gamma_{i,ini} + \gamma_{i,1}^{st}\left(1 - e^{-D_{\gamma_{i,1}}p}\right) + \gamma_{i,2}^{st}\left(1 - e^{-D_{\gamma_{i,2}}p}\right) \quad \text{..... (87)}$$

Recalling that the initial values for accumulated plastic strain were only estimates, it is now necessary to recalculate these values using the model. Thus for each cycle of interest the accumulated plastic strain is found using the constitutive model with the isotropic hardening and cyclic kinematic hardening parameters just acquired. It is necessary to now use the updated values of accumulated plastic strain to re-converge to a refined set of cyclic hardening parameters. This process is repeated until there is a negligible variation between the new predicted accumulated plastic strain and its previous value. Upon completing this process a complete set of model parameters will have been found for a given temperature and strain range.

As an aside, it is noted that a useful rule when determining rate parameters for exponential functions is to know the point at which one wants the function to saturate. Therefore, in the case of cyclic hardening previously discussed, the product of the accumulated plastic strain and the evolution rate should be greater than or equal to 5. It is important to take this into consideration when performing parameter optimization as parameters that do not meet this criterion will not saturate at the desired point.

4.6 Determination of strain-range dependent parameters

Ideally the fashion by which strain-range dependent parameters would be determined would be by first finding the cyclic hardening parameters for each strain-range of interest. This requires that a full fatigue test be performed for each strain-range under consideration; however, in this investigation, to limit the number of tests, 8 multiple strain-range (MSR) tests were performed instead. This reduces the total number of tests by 16. The benefit of a reduced number of tests is contrasted though with a loss of information in regards to cyclic hardening. Taking for example Fig. 10, which shows a typical MSR response at 25°C, and comparing it to Fig. 11, which shows the cyclic hardening response at 25°C for the single strain-range of 0.6%, one can see that the hardening response at a strain-range of 0.6% in the MRS test has not fully saturated before the strain-range is increased to 0.8%. Similarly, a lack of saturation is observed at the two higher rates of 0.8% and 1.0%. This is an issue since when determining strain-range dependent parameters the value of interest is the saturated value of γ_i. Therefore, because γ_i cannot be determined directly for each strain range it must

be determined indirectly for strain-ranges for which no complete cyclic hardening response exists.

To begin this process, one starts with Eqns. 20 and 21 which describe the variation of the saturated value of the kinematic back stress parameter γ_i as a function of strain-range. Here one can see that three parameters of interest are a_{γ_i}, b_{γ_i}, and c_{γ_i} for each hardening rule. This function can either represent an exponentially increasing function followed by saturation or an exponentially decreasing function followed by saturation. In the case of cyclic hardening, this function will be of the exponentially decreasing nature as a smaller γ_i increases the stress at which the back stress saturates. Therefore initials limit on the parameters on the strain range dependent parameters can be set a follows: a_{γ_i} will be negative and approximately equal to γ_i^o; b_{γ_i} will be positive and will be equal to what γ_i^o would be for the highest strain range; c_{γ_i} will be in the range of 100-1000 due to the values of plastic strain ranges found in this investigation.

With these estimates made for a_{γ_i}, b_{γ_i}, and c_{γ_i} the optimization routine can be utilized. Here the residual will not be based on the fit of an individual hysteresis curve but rather on the stress amplitude response found in the MSR test. Taking the example case of 25°C, noting that only one hardening rule was used at this temperature, a_{γ_i}, b_{γ_i}, and c_{γ_i} were optimized such that the peak stress at the 200th cycle in the MSR response was matched by the simulated response and so that the γ_i^o, as predicted by Eqn. 20, remained as close as possible to the value found during the cyclic hardening parameter determination process for the strain range at 25°C. The results from this optimization can be seen by contrasting Fig. 10 and 11. Figure 10 depicts the simulated MSR response without strain range dependence and Fig. 11 depicts the simulated response with strain range dependence. With strain range dependence implemented there is a marked improvement in the simulation of this response. This completes parameter determination process for this model.

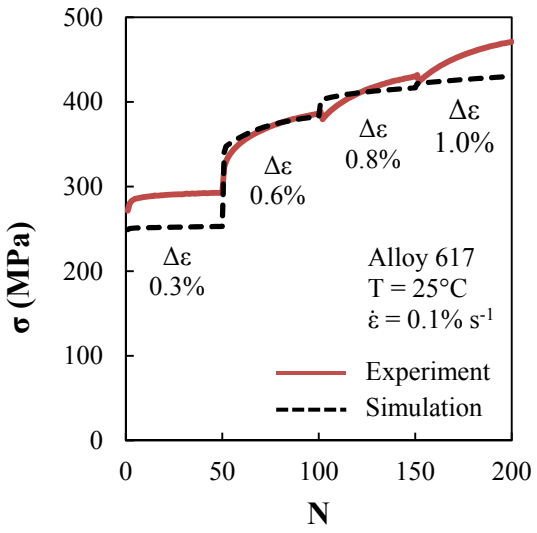

Fig 10: Multi-strain range fatigue response at 25°C simulated without strain range dependence parameters

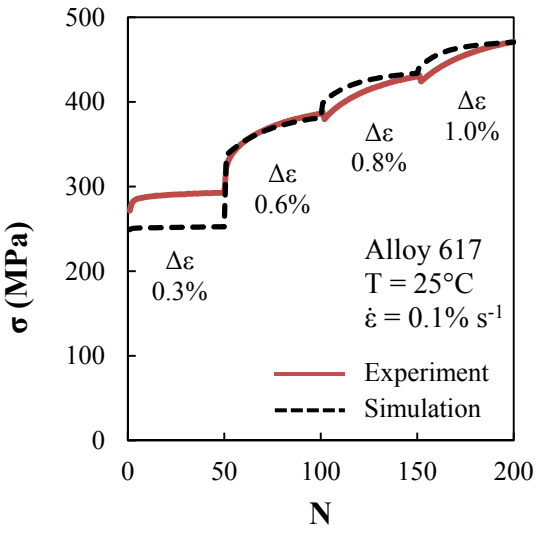

Fig 11: Multi-strain range fatigue response at 25°C simulated without strain range dependence parameters

5. Model Parameters

In Table 1a-e the model parameters determined in this investigation are given. They are split into five categories: the elastic parameters, the kinematic hardening parameters, the isotropic hardening parameters, the kinematic hardening evolution parameters for the strain range of 0.6%, and finally the strain-range dependent parameters. As will be discussed in the simulation portion of this work there are some downsides to implementing the strain-range dependent parameters. For this reason both the kinematic hardening evolution parameters determined at a strain range of 0.6% and the strain range dependent parameters are given. Note that by using Eqns. 20 and 21 the strain-range dependent parameters can be reduced down to approximately the values given in Table 1d. Note that no parameters have been determined yet for the temperature of 850°C as there was a delay in the delivery of the experimental data for this temperature.

Table 1a — Elastic Parameters

Parameter	Units	25°C	650°C	750°C	850°C	950°C
E	MPa	210,000	173,000	158,000	-	140,000
σ_o	MPa	150.4	100.4	122	-	0

Table 1b — Kinematic Hardening Parameters

Parameter	Units	25°C	650°C	750°C	850°C	950°C
C_1	MPa	15,000,000	1,135,600	1,135,500	-	1,134,171
C_2	MPa	738,880	135,673	134,367	-	113,897
C_3	MPa	309,392	113,062	113,140	-	32,497
C_4	MPa	2,500	2,500	500	-	1750
γ_1	-	990,698	35,288	23,000	-	2675.2
γ_2	-	363,491	16,348	20,000	-	2407.7
γ_3	-	2,046.3	1,859.3	1,973.7	-	2166.9
γ_4	-	0	0		-	0
b_1	MPa^(1-r_1)	0	0	0	-	6.041 E-03
b_2	MPa^(1-r_2)	0	0	0	-	1.046 E-01
b_3	MPa^(1-r_3)	0	0	0	-	3.320 E-04
b_4	MPa^(1-r_4)	0	0	0	-	9.668 E-03
r_1	-	1	1	1	-	9
r_2	-	1	1	1	-	1.5
r_3	-	1	1	1	-	9
r_4	-	1	1	1	-	1.5

Table 1c — Isotropic Hardening Parameters

Rule	Parameter	Units	25°C	650°C	750°C	850°C	950°C
Hardening Rule 1	R^{st}	MPa	39.44	37.61	14.96	-	-
	b_r	-	0.8044	61.33	76.22	-	-
Hardening Rule 2	R^{st}	MPa	0	10.90	108.7	-	-
	b_r	-	1	0.2272	1.352	-	-

Table 1d —Kinematic Hardening Parameter Evolution ($\Delta\varepsilon = 0.6\%$)

Rule	Parameter	Units	25°C	650°C	750°C	850°C	950°C
Hardening Rule 1	γ^{st}_1	-	0	-12,800	0	-	-
	γ^{st}_2	-	0	-4,875.7	0	-	-
	γ^{st}_3	-	-700.5	-634.4	-266.0	-	-
	γ^{st}_4	-	0	0	0	-	-
	$D_{\gamma 1}$	-	1	7.496	1	-	-
	$D_{\gamma 2}$	-	1	10.07	1	-	-
	$D_{\gamma 3}$	-	8.983	18.57	127.6	-	-
	$D_{\gamma 4}$	-	0	1	1	-	-
Hardening Rule 2	γ^{st}_1	-	0	-15,076	0	-	-
	γ^{st}_2	-	0	-8228.9	0	-	-
	γ^{st}_3	-	0	-836.1	-491.7	-	-
	γ^{st}_4	-	0	0	0	-	-
	$D_{\gamma 1}$	-	1	0.2923	1	-	-
	$D_{\gamma 2}$	-	1	0.3696	1	-	-
	$D_{\gamma 3}$	-	1	0.3290	3.035	-	-
	$D_{\gamma 4}$	-	1	1	1	-	-

Table 1e — Strain Range Dependence Parameters

Rule	Parameter	Units	25°C	650°C	750°C	850°C	950°C
Hardening Rule 1	$a_{\gamma 1}$	-	0	-12800	0	-	-
	$a_{\gamma 2}$	-	0	-4,875.7	0	-	-
	$a_{\gamma 3}$	-	-1,200	-719	-413.6	-	-
	$a_{\gamma 4}$	-	0	0	0	-	-
	$b_{\gamma 1}$	-	0	0	0	-	-
	$b_{\gamma 2}$	-	0	0	0	-	-
	$b_{\gamma 3}$	-	833.6	194	352.3	-	-
	$b_{\gamma 4}$	-	1	10	0	-	-
	$c_{\gamma 1}$	-	1	1	0	-	-
	$c_{\gamma 2}$	-	1	1	0	-	-
	$c_{\gamma 3}$	-	366.3	614	713.8	-	-
	$c_{\gamma 4}$	-	1	1	0	-	-
Hardening Rule 2	$a_{\gamma 1}$	-	0	-15,076	0	-	-
	$a_{\gamma 2}$	-	0	-8,228.9	0	-	-
	$a_{\gamma 3}$	-	0	-950	-710.6	-	-
	$a_{\gamma 4}$	-	0	0	0	-	-
	$b_{\gamma 1}$	-	0	0	0	-	-
	$b_{\gamma 2}$	-	0	0	0	-	-
	$b_{\gamma 3}$	-	0	75	502.3	-	-
	$b_{\gamma 4}$	-	0	0	0	-	-
	$c_{\gamma 1}$	-	1	1	0	-	-
	$c_{\gamma 2}$	-	1	1	0	-	-
	$c_{\gamma 3}$	-	1	75	669.9	-	-
	$c_{\gamma 4}$	-	1	1	0	-	-

6. Model Simulations

6.1 Simulations of cyclic hardening responses

Cyclic hardening was seen at temperatures ranging from 25°C – 850°C. However, as was mentioned previously, due to a delay in the delivery of data at 850°C no parameters have been able to be determined yet at this temperature. Therefore the following figures will show the simulation of the cyclic hardening response from 25°C to 750°C.

In Fig. 12a-e the cyclic hardening response at 25°C is depicted for a strain range of 0.6% and a strain rate of 0.1% s^{-1}. The first four figures compare the experimental hysteresis response to that of the model for cycles 1, 20, 200, and 10,000. The fifth figure compares the experimental stress amplitude response to that of the simulated response for the first 5800 cycles. It should be mentioned at this temperature the fatigue life is in excess of 20,000 cycles, the number of cycles at which the test was terminated, but in order to better present the hardening response only a reduced number of cycles are shown. From these five figures it can be seen that the cyclic hardening response can be simulated well by the model. Currently, the only area where a large discrepancy between the experimental and simulated response exists is during the first monotonic path. The reason for this being, as discussed in the parameter determination section, there does not exist one set of parameters that can simulate well both the monotonic and cyclic responses.

Similar to above, Fig. 13a-f shows the cyclic hardening response at 650°C at a strain range of 0.6% and a strain rate of 0.1% s^{-1}. In the first five figures the simulated response of cycles 1, 20, 200, 1000, and 5000 are shown against the experimental response. The sixth figure presents the comparison of the experimental and simulated hardening stress amplitude response. Again the model is able to simulate well the hysteresis loops for each cycle as wells and the stress amplitude response. The only shortcoming in this case is a slightly worse prediction of the monotonic response.

Fig. 14a-f shows the cyclic hardening response for 750°C at a strain range of 0.6% and a strain rate of 0.1% s^{-1}. Figures 14a-e show the comparison between the simulated and experimental hysteresis loops for cycles 1, 20, 200, 1000 and 2000. Figure 14f depicts the simulation of the stress amplitude response. The same conclusions are drawn as explains in the above to examples. Note however that the late term cyclic softening is not simulated.

Fig. 15 shows the compilation of the stress amplitude responses for each of the above temperatures investigated. Here we can see that the model is quite capable of simulating the range of responses seen.

While the cyclic hardening response is simulated quite well at a strain range of 0.6% at 650°C when predicting the cyclic hardening response at higher strain ranges some concerns arise. Fig. 16 presents the simulated cyclic hardening responses for the strain ranges of 0.6%, 0.8%, and 1.0% at 650°C. Note that upon increasing the strain range to 0.8% from 0.6% the saturated stress increases by approximately 75 MPa. That saturated stress increased again by approximately 65 MPa upon further increasing the strain range to 1.0%. This does not match with the response found in the multi-strain-response seen in Figs. 10 or 11. Here, while there is an increased degree of hardening observed at the higher strain ranges of 0.8% and 1.0%, the magnitude of the increased hardening does not seem to indicate the significant degree of increased hardening that was simulated. Is should be noted that no definitive conclusion can be made regarding this issue at this point as no fatigue tests were carried out to failure at the strain ranges of 0.8 and 1.0%.

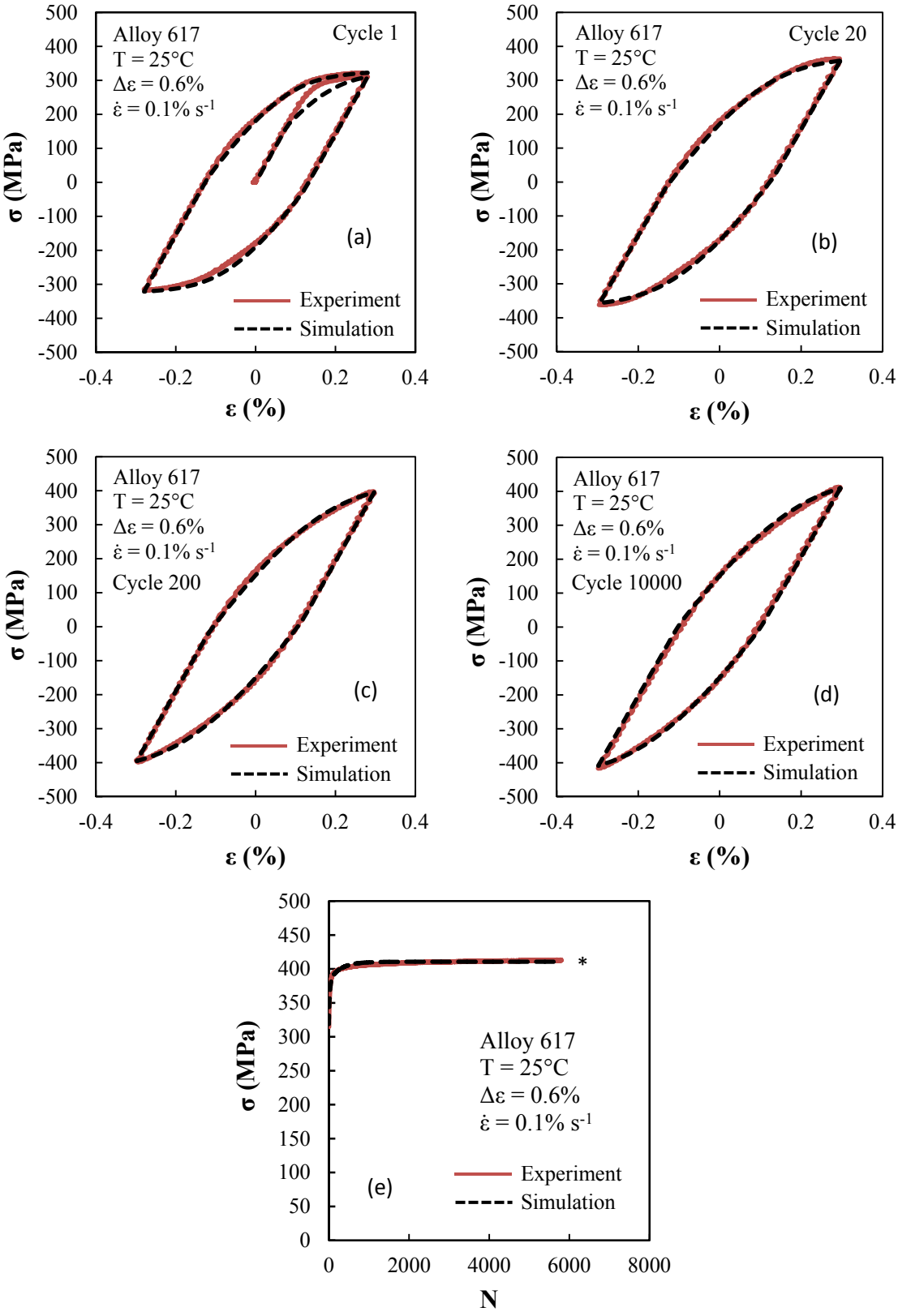

Fig. 12: Simulation of hysteresis loop responses at 25°C and a strain rate of 0.1% s^{-1} (a) Cycle 1 (b) Cycle 20 (c) Cycle 200 (d) Cycle 10000 (e) Simulation of stress amplitude response. *Does not indicate failure; test was stopped at 20000 cycles without fracture

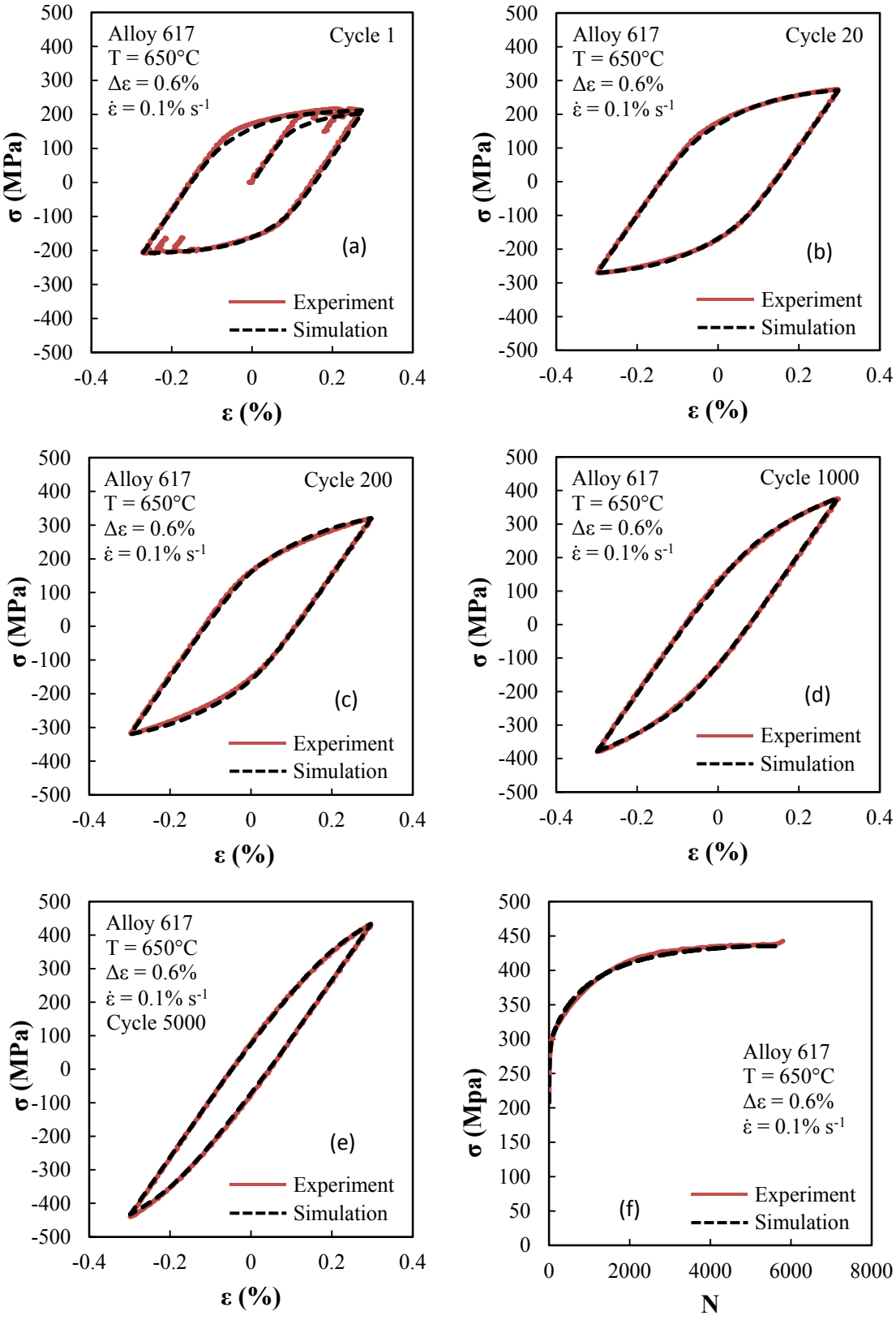

Fig. 13: Simulation of hysteresis loop responses at 650°C and a strain rate of 0.1% s^{-1} (a) Cycle 1 (b) Cycle 20 (c) Cycle 200 (d) Cycle 1000 (e) Cycle 5000 (f) Simulation of stress amplitude response.

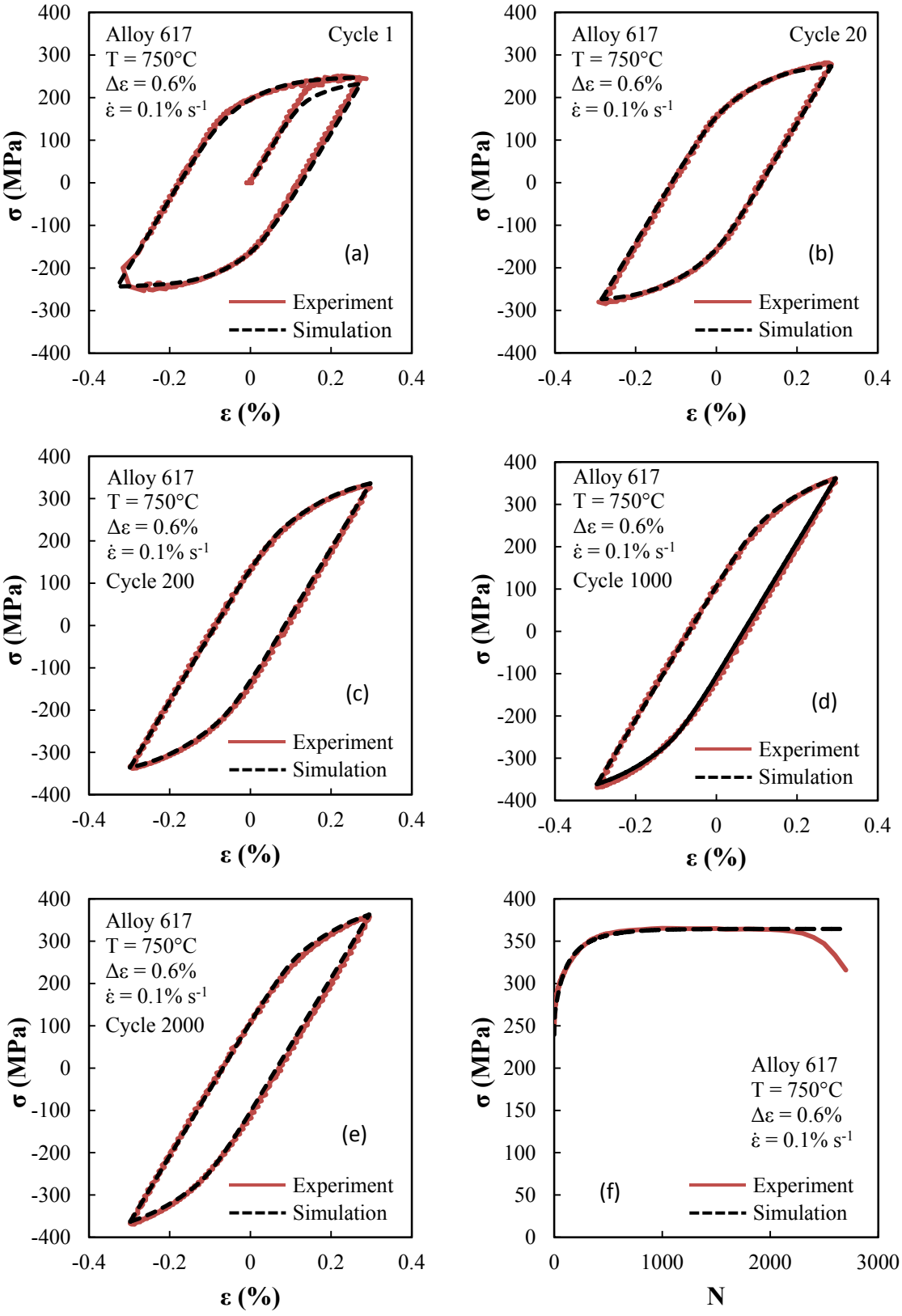

Fig. 14: Simulation of hysteresis loop responses at 750°C and a strain rate of 0.1% s^{-1} (a) Cycle 1 (b) Cycle 20 (c) Cycle 200 (d) Cycle 1000 (e) Cycle 2000 (f) Simulation of stress amplitude response.

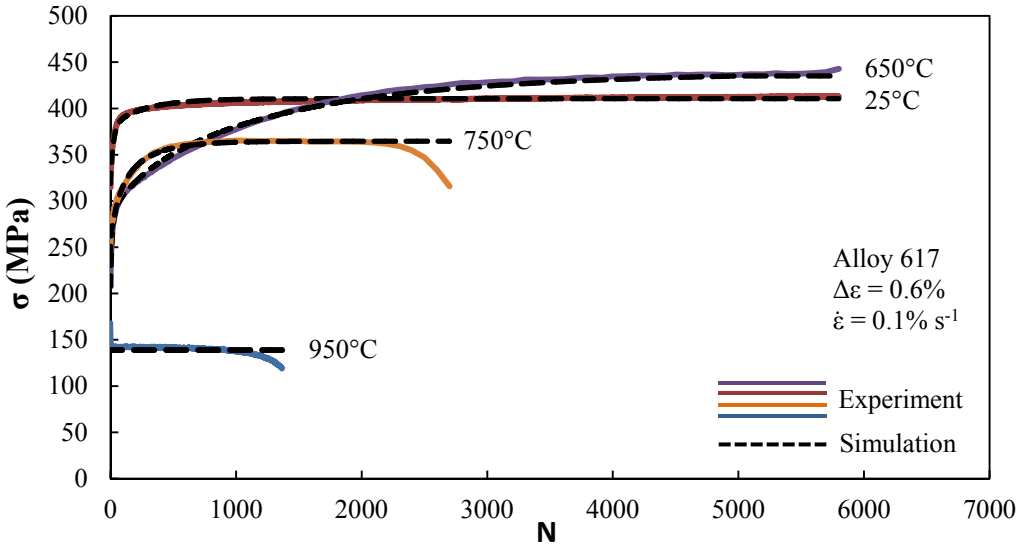

Fig. 15: Stress amplitude response compilation for temperatures 25°C – 950°C

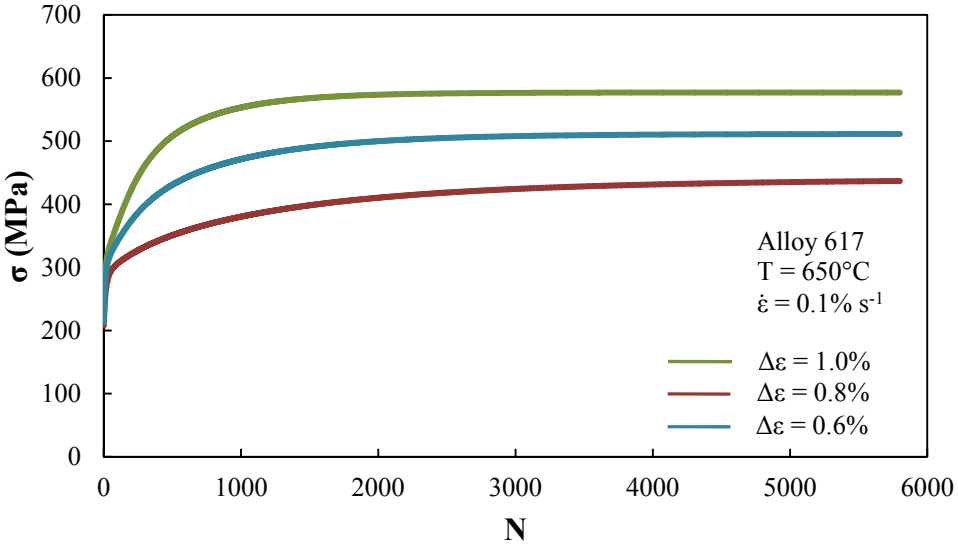

Fig. 16: Simulated stress amplitude response at 650°C for three strain ranges

6.2 Simulation of low temperature multi-strain-range responses

In this experimental program multi-strain-range tests were performed over five temperatures (25°C, 650°C, 750°C, 850°C, and 950°C) and two strain rates (0.1% s^{-1} and 0.04% s^{-1}) for a total of 10 tests. For this discussion it is useful to discuss the temperatures considered as rate-independent first, 25-750°C, followed by the rate-dependent temperature of 950°C. In Fig. 17a-f two sets of results are given. First, the simulated stress amplitude response without strain range dependence is shown in the left column for each temperature. Second, the simulated stress amplitude response with strain range dependence is shown on the right. Here all experimental responses are shown at the higher strain rate of 0.1% s^{-1} since a negligible variation in response exists between these two rates. Comparing the two responses it is clear that with the implementation of the strain range dependence parameters a marked improvement in the simulated response is seen, especially at 25°C. At the 650° and 750°C this improvement is mostly seen at the highest strain range.

Overall, with the current model implementation, the higher strain ranges of 0.6%, 0.8%, and 1.0% were able to be simulated very well; however a larger discrepancy between the simulated and experimental responses is seen at the lowest strain range of 0.3% at all temperatures. This discrepancy is most prominent at 25°C. The reason for this can be explained as follows: In a hardening material one usually expects for the kinematic hardening parameter γ_i to decrease with increasing strain range as a lower γ_i results in an increased saturation stress for the respective back stress rule. Contrary to this expectation, in this specific case it was found that at a strain range of 0.3% and for temperatures in the range of 25-750°C the model parameters γ_i required to accurately simulate this strain range was lower than was required at the higher strain range of 0.6%. Thus, since the strain range dependence function can only be an increasing or decreasing function as a function of strain range it is not possible to simulate both a lower γ_i at a strain range of 0.3% and a lower γ_i at a strain range of 0.8%. Therefore to best simulate a broader range of experimental responses, a decreasing strain-range dependence function was used with the understanding that some degree of error would be seen in the prediction of the lower strain range responses.

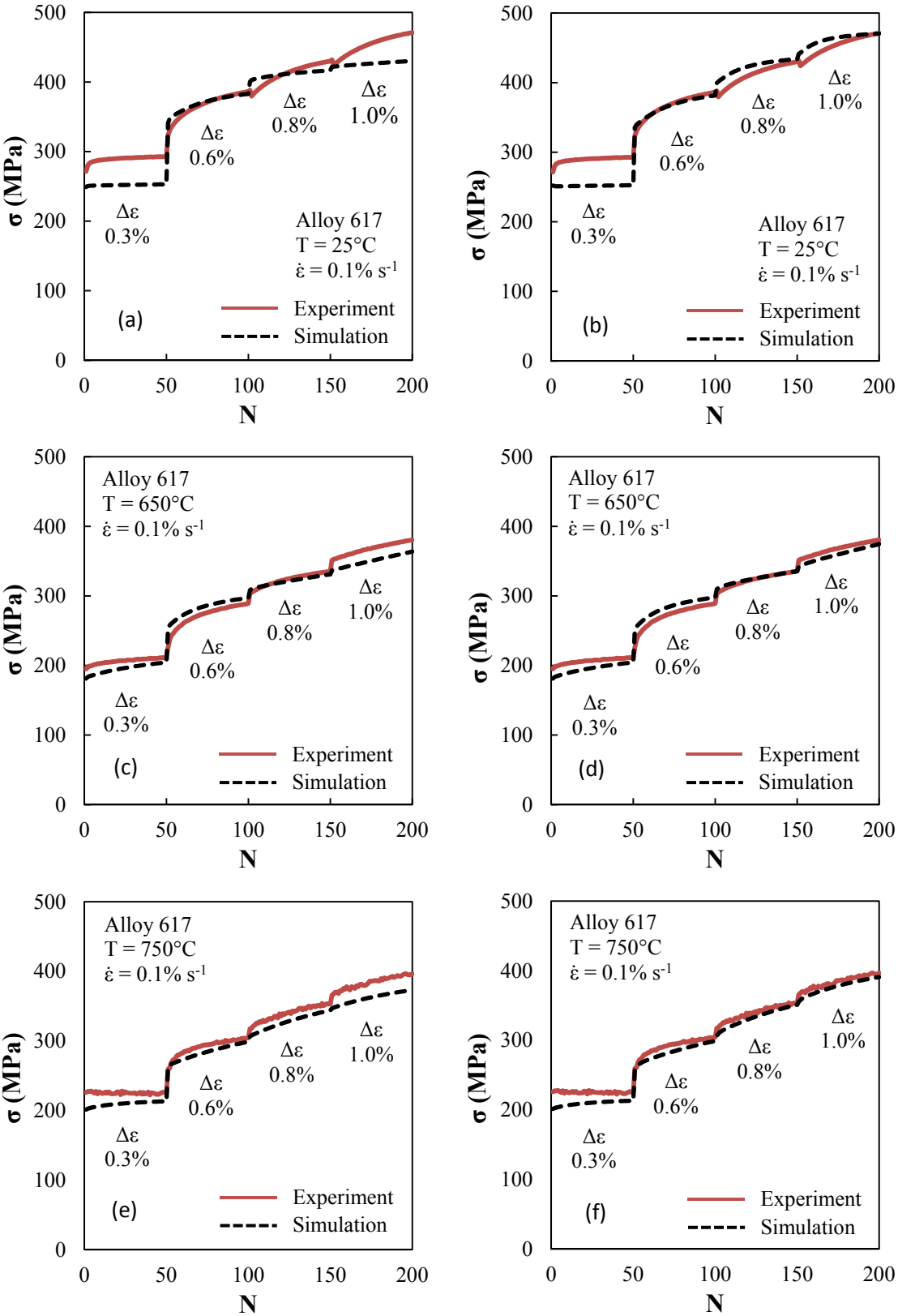

Fig. 17: Simulated stress amplitude response for multi-strain range responses with and without strain range dependence. 25°C: (a) w/o SRD (b) w/ SRD, 650°C: (c) w/o SRD (d) w/SRD, 750°C: (e) w/o SRD (f) w/ SRD

6.3 Simulation of strain-rate dependence

At 950°C fatigue and fatigue-creep tests were conducted at two strain rates by this investigation, 0.1% s^{-1} and 0.04% s^{-1}. In addition to the data collected by this study, data garnered by the Idaho National Lab (INL) has been utilized [1-4]. The INL conducted a similar program on the fatigue and fatigue-creep responses of Alloy 617 at high temperatures [1-4]; however the tests were done using different testing parameters. Note that the same stock material was used by both this and the INL investigations. Incorporating the INL data set allows, in the case of strain-rate dependence, for the use of the additional strain rate of 0.01% s^{-1}.

As discussed in Sections 4.3 and 4.4 model parameters were determined, in part, by using they hysteretic responses from the first saturated cycle of three fatigue tests; on of each test being performed at each of the aforementioned strain-rates. The simulation of these responses is shown in Fig. 18. Here the two fatigue tests conducted at strain-rates of 0.1% s^{-1} and 0.04% s^{-1} were performed at a strain range of 0.6% whereas the lower strain-rate fatigue test was performed at a strain range of 0.01% s^{-1}. While one typically does not compare directly the material responses across separate strain ranges, and as will be discussed subsequently, a significant strain range response was not seen at strain range above 0.6% and therefore a comparison between the two strain ranges is possible.

Returning to Fig. 18 one can see that the current model can simulate well the material response at each strain-rate. In the next figure, Fig. 19, the stress amplitude response is shown against number of cycles for each of the three strain-rates. Note that with increasing strain-rate that there is an increasing degree of cyclic softening seen in the material response. Currently the model is not able to simulate cyclic softening as a function of strain-rate and hence only one kind of softening response can be simulated. At the present moment, no softening has been implement at 950°C, thus, the model is able to simulate quite well the material response at the highest strain-rate of 0.1% s^{-1} but only the initial response at the lower two strain rates. It is important to note that the experimental stress amplitude response for the lower strain rate can be somewhat misleading. In Fig. 19 it looks as if the model is significantly underpredicting the initial stress amplitude response at this strain rate; however, why this is not the case can be explained by examining the 2^{nd} cycle hysteresis loop shown in Fig. 19. Remark that there is a significant degree of noise in the stress response for this strain

ranges. The controller that was recording the stress amplitude response for this experiment recorded the peak stress that occurred during each half-cycle. This peak stress does not represent the mean stress of which the model simulates. Hence, the appearance of underprediction in the stress amplitude response is actually a more representative prediction of the overall hysteresis behavior.

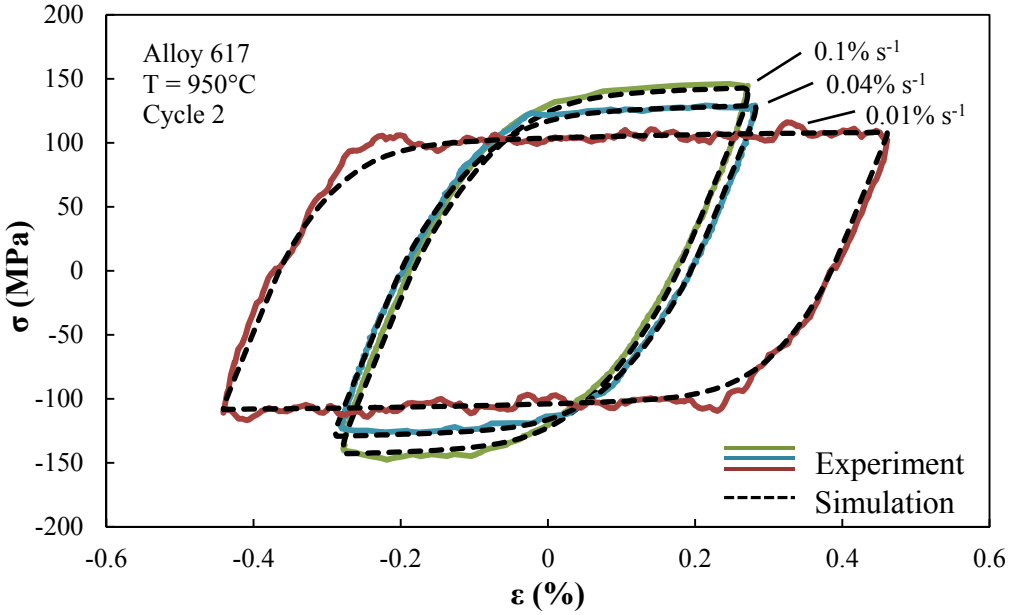

Fig. 18: Simulation of hysteresis loops for fatigue tests performed at three strain rates at 950°C

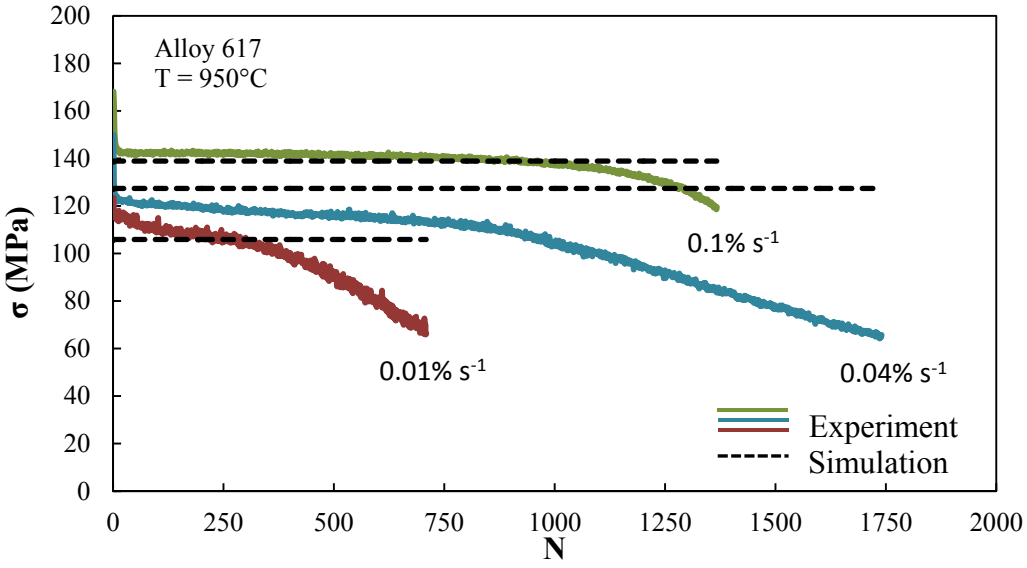

Fig. 19: Simulation of stress amplitude response for fatigue tests performed at three strain rates at 950°C

6.3 Simulation of the relaxation response

At 950°C, fatigue-creeps tests have been performed at two strain ranges in this study, 0.4% and 0.6%, as well as four additional strain ranges, 0.3%, 0.8%, 1.0%, and 2.0%, when including the data set made available through the INL. When fatigue-creep tests were performed at high temperatures, for strain controlled tests, relaxation was seen during periods of peak strain hold. To simulate relaxation well both the magnitude and the rate of relaxation must captured.

In Fig. 20 the simulation of a typical fatigue test is shown at a strain range of 0.6% and a strain rate of 0.1% s^{-1}. Here one can see, as shown previously, that the model simulated the fatigue response well. To the right of the previous figure is Fig. 21 which shows the simulation of the fatigue-creep response performed at the same strain range and strain rate at the fatigue test except with an applied one minute peak tensile strain hold. From this figure one can see that the model is quite capable of simulating both the magnitude of the relaxed stress in addition to the overall shape of the hysteresis curve. One area that the model cannot simulate well is what is termed the stress overshoot during strain reversal immediately after strain hold period [3]. This manifests itself as a peak in the hysteresis loop following the peak tensile strain hold. This is visible to some extent in Fig. 21 but will be more visible in later plots. Currently, the model is unable so simulate this stress overshoot.

In addition to hysteresis response, it is necessary to investigation the relaxation curve or the rate of relaxation against time. The simulation of this response for the previously mentioned fatigue-creep test can be seen in Fig. 22. Here it can be seen that a relatively good simulation of the relaxation response can be obtained; however, the model cannot simulate perfectly the initial response. This is primarily due to the dependence of the hysteresis loop shape and the static recovery parameters b_i and r_i. This makes it difficult to simulate well the hysteresis loop shape, the strain-rate effect, and the relaxation response. Therefore, to better simulate the shape and hysteresis loops and the strain-rate response the simulation of the relaxation rate was sacrificed to a small degree. Overall the simulation of the relaxation response is worse during the initial period of relaxation. When the duration of the tensile strain hold is increased the model is more capable of predicting the relaxation response. This can be seen clearly in Figs. 23 and 24.

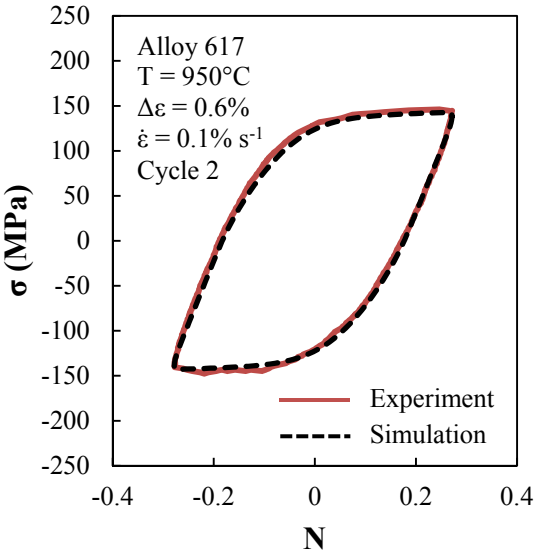

Fig. 20: Simulation of fatigue hysteresis response at 950°C.

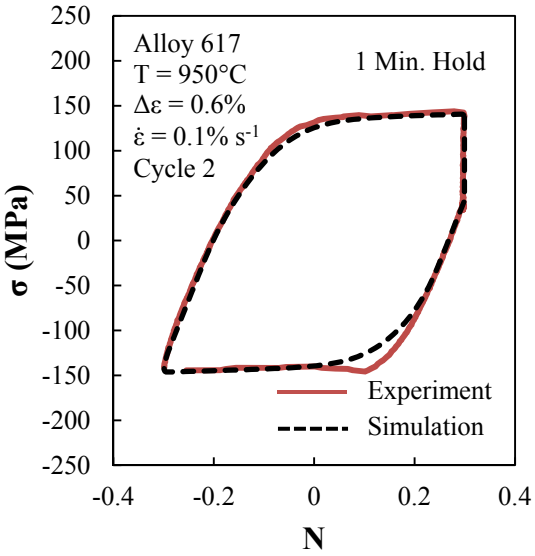

Fig. 21: Simulation of fatigue-creep hysteresis response at 950°C.

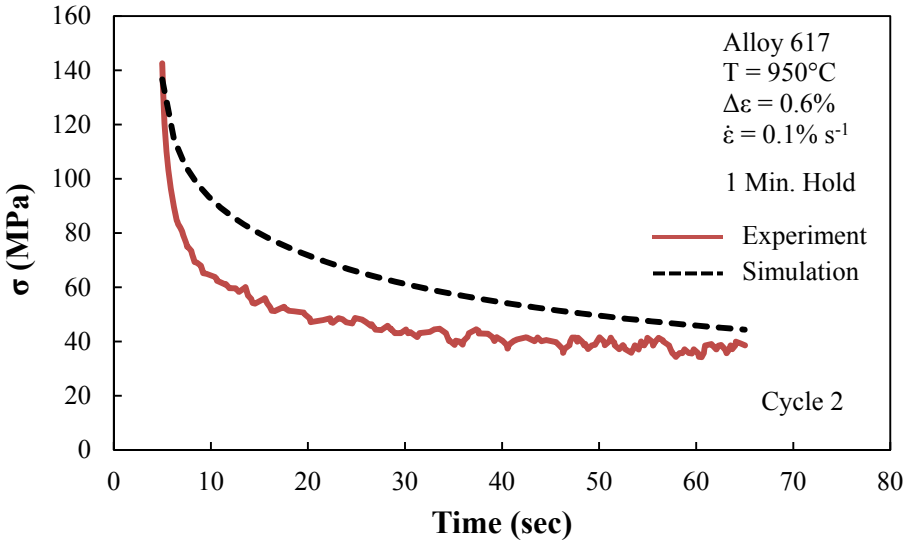

Fig. 22: Simulation of relaxation response for a fatigue-creep test w/ 1 min. hold

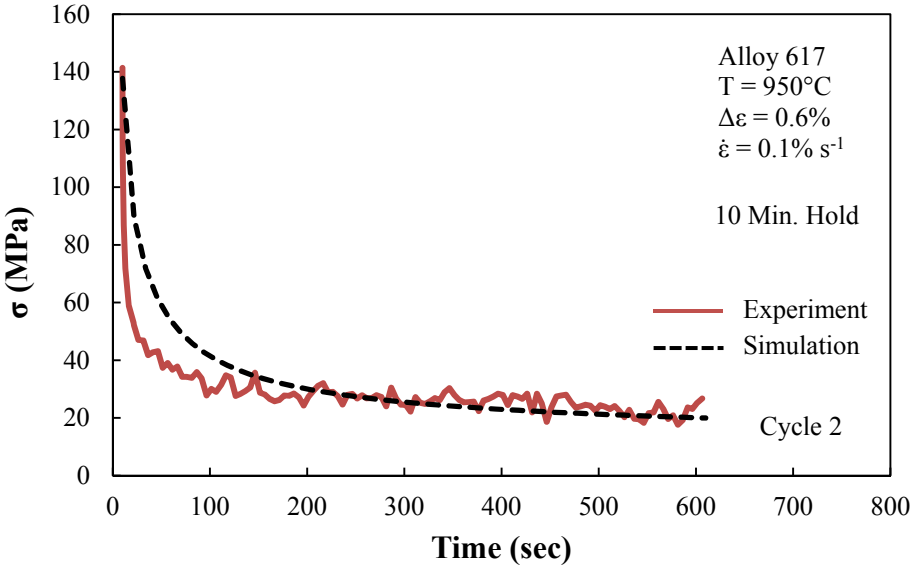

Fig. 23: Simulation of relaxation response for a fatigue-creep test w/ 10 min. hold

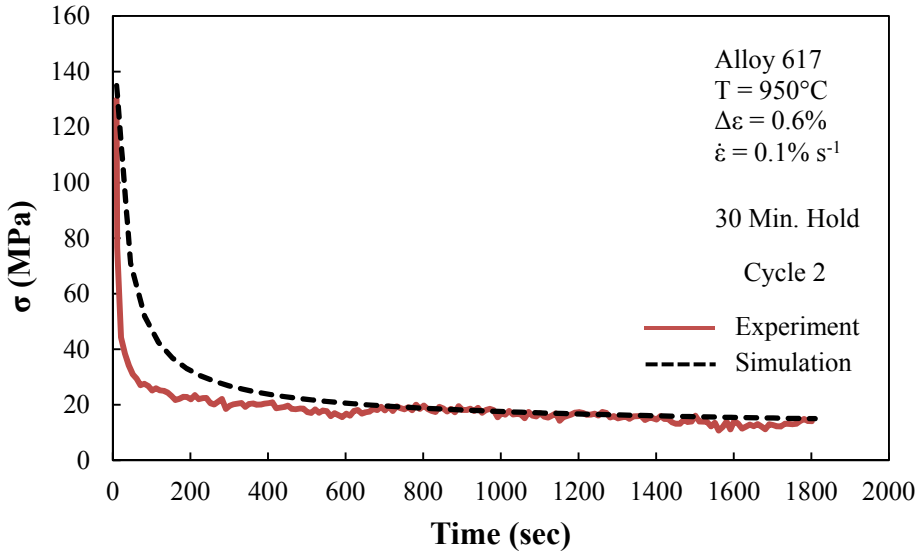

Fig. 24: Simulation of relaxation response for a fatigue-creep test w/ 30 min. hold

6.5 Simulation of 950°C strain-range response

The strain range response at 950°C can be seen as a piecewise function in that the lower strain ranges of 0.3% and 0.4% display a similar stress amplitude response whereas the higher strain ranges of 0.6% - 1.0% show another. This behavior can be seen by examining Fig. 25, which shows the MSR response at a strain rate of 0.1% s^{-1}. Here one can see that upon increasing the strain range from 0.3% to 0.6% there is rapid softening to a stable response at 0.6%. Upon further increase in the applied strain range no significant degree of softening or hardening was seen during this limited set of loading cycles. For the MSR test performed at the higher strain rate of 0.1% s^{-1} one will remark that the simulation underpredicts the material response; this is due to both the variability of the material response and the fact that model parameters were determined from the mean response. The MSR response for the lower rate of 0.04% is shown in Fig. 26. Note here that the same piecewise stress amplitude behavior is seen as mentioned previously. For this test the material response was more in line with the mean response therefore a better prediction of the stress amplitude response was seen overall. Since cyclic softening was not implemented, note that the cyclic softening response varies according to applied strain range, strain rate, and fatigue-creep hold time and can be better seen at the full fatigue life.

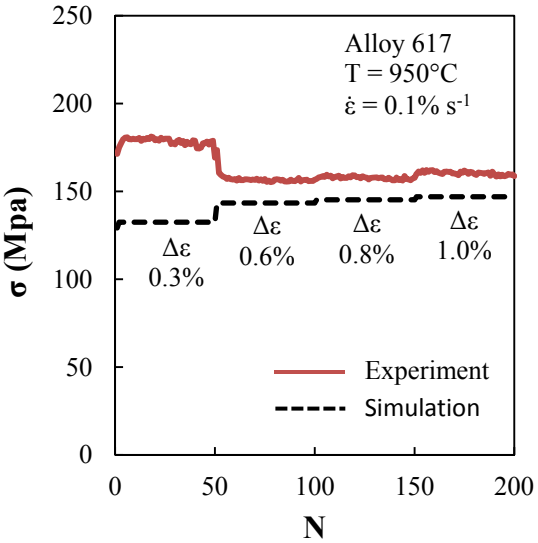

Fig. 25: Simulation of fatigue hysteresis response at 950°C.

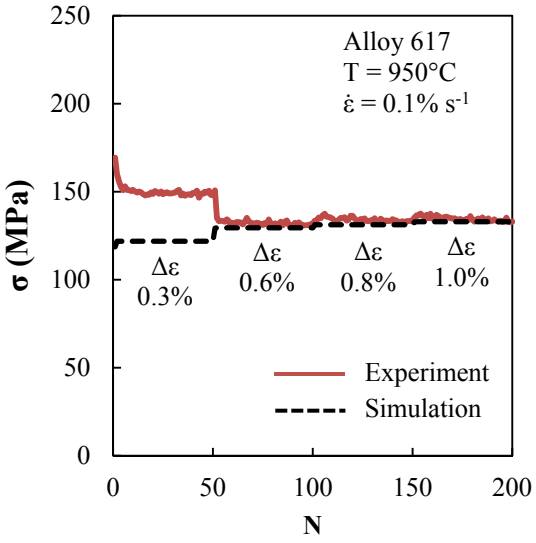

Fig. 26: Simulation of fatigue hysteresis response at 950°C.

The ability of the model to simulate the lower strain range hysteresis response is depicted in Fig. 27. Here one can see that the model is not able to predict the stiffer response found at this strain range; note that parameters were determined from response conducted at a strain range of 0.6% and that no strain range dependence parameters were utilized at 950°C. However when the loading wave form is changed from fatigue to fatigue-creep the hysteresis response of the material changes significantly, see Fig. 28. Here the material response is simulated much more closely the response at a strain range of 0.6%. Remark that the model does not capture the stress overshoot response mentioned in section 6.3.

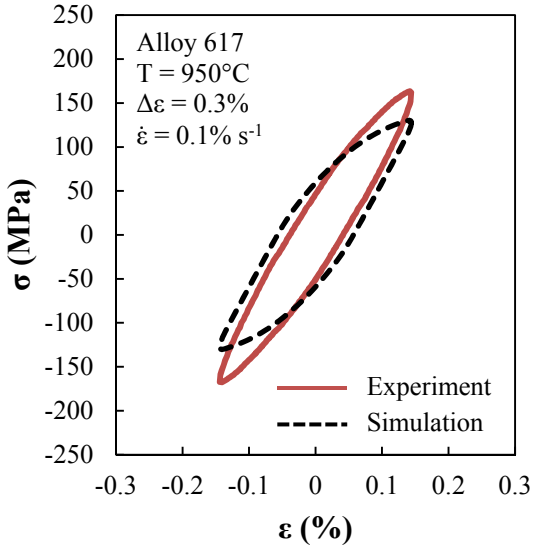

Fig. 27: Simulation of fatigue hysteresis response at strain range of 0.3% and 950°C.

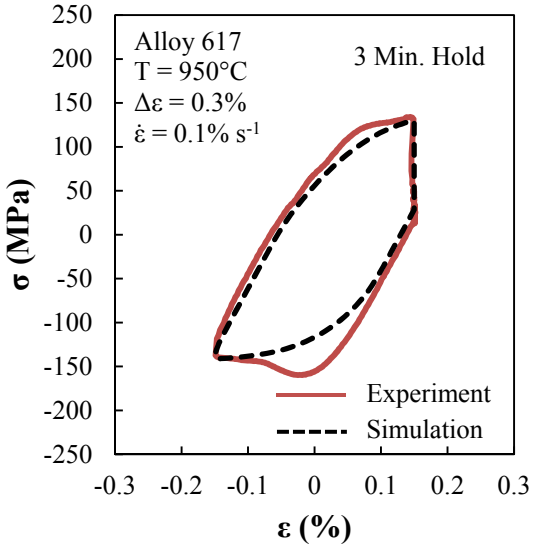

Fig. 28: Simulation of fatigue-creep hysteresis response at a strain range of 0.3% hysteresis response and 950°C.

At a strain range of 0.4% the material exhibits, albeit to a lesser degree, the same phenomenon just mentioned. That is under fatigue loading the material response is stiffer than under fatigue-creep loading during the initial cycles. In Fig. 29 the second cycle from a fatigue tests performed at a strain range of 0.4% and a strain rate of 0.1% s^{-1} is shown. In Fig. 30 the second cycle form a fatigue-creep with the same strain range and strain rate as just mentioned is depicted. Comparing these two responses one can see that the model is able to better simulate the material response under fatigue-creep loading as opposed to fatigue loading at this strain range.

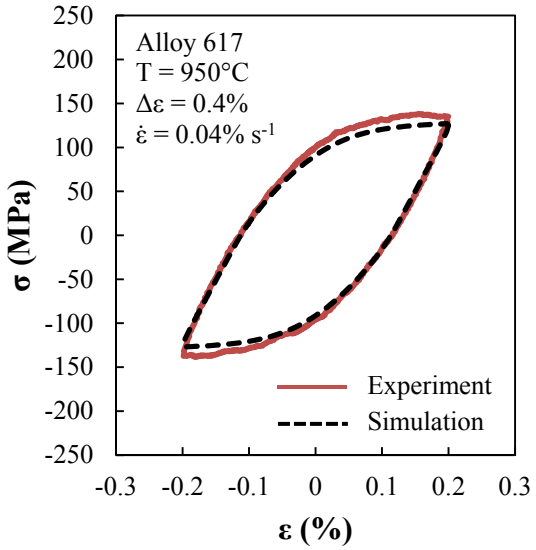

Fig. 29: Simulation of fatigue hysteresis response at strain range of 0.4% and 950°C.

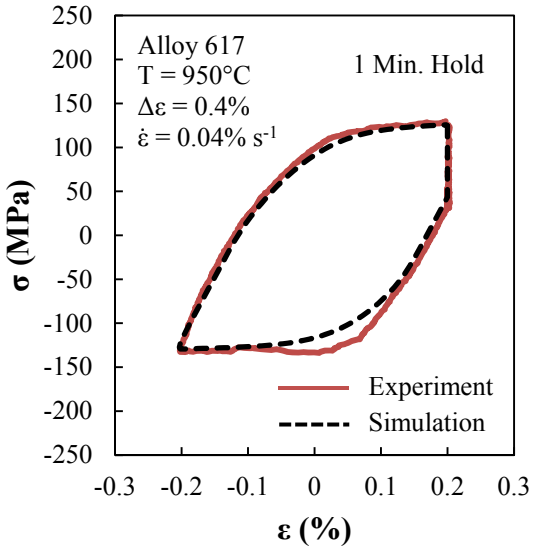

Fig. 30: Simulation of fatigue-creep hysteresis response at a strain range of 0.4% hysteresis response and 950°C.

6.6 *Current model deficiencies*

At a temperature of 750°C there exists a degree of strain rate dependence which can be seen from the three experiments plotted in Fig. 31; however, in this case the amplitude of the initial cycles are the same with rate dependence manifesting itself as a reduction in the degree of cyclic hardening. Note that the stress amplitude response for the fatigue tests performed at the lowest rate was digitized from data presented in Rao et al. [16]. Under these circumstances it is not possible, with the current state of modeling, to simulate this type of rate response and thus certain compromises must be made. In this specific case it was decided to determine parameters from the material response at a rate of 0.1% s^{-1} to be consistent with the parameters determined at other temperatures; hence, the simulated response at this temperature and strain range is able to match the experimental response at the highest strain range and not the others.

At 950°C a similar compromise must be made with respect to a different modeling variable. As discussed in Chapter 2, a large degree of variation was seen in the material response under identical loading conditions (i.e. tests having the same strain-range, strain-

rate, and tensile-strain hold time). Moreover, it was found that, for a given strain-rate and strain-range, when a tensile-strain hold was applied increased cyclic softening was observed. Currently, however, the model cannot predict differing degrees of cyclic softening based on the presence or absence of an applied strain-hold.

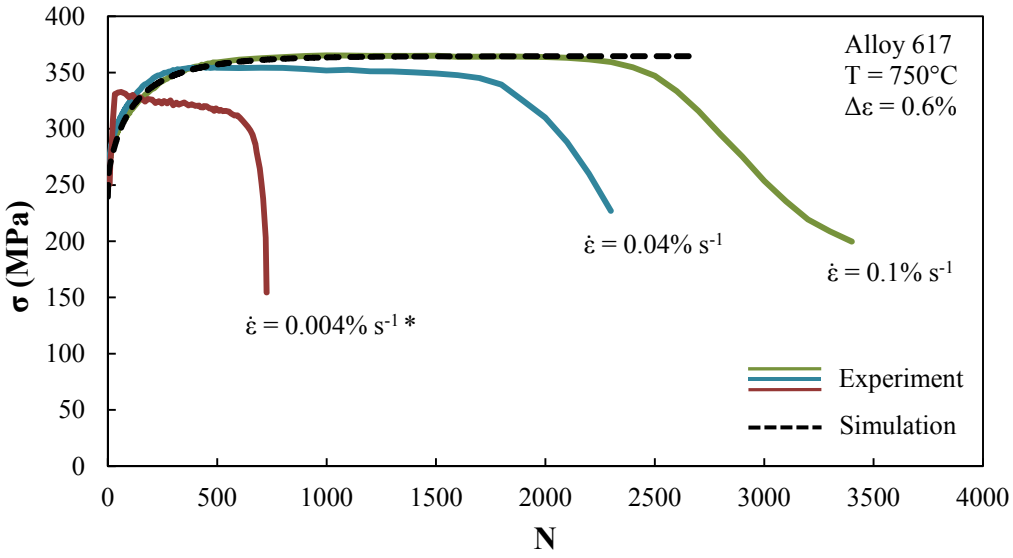

Fig. 31: Simulation of stress amplitude response for fatigue tests performed at three rates at 750°C

7. Conclusions

An advanced unified viscoplastic constitutive model developed at North Carolina State University was presented for the use in NGNP design, specifically the design of the intermediate heat exchanger. The numerical implementation based on the radial return method was described in detail. A novel parameter determination process for the determination of both rate-independent and rate-dependent parameter was given. This process has the benefit of allowing for materially based initial parameters for the rate-dependent parameters K and n seen in the flow rule. Lastly, a wide variety of simulations were shown for a broad set of fatigue and fatigue-creep responses of alloy 617 for temperature ranging from 25°C to 950°C. These simulations demonstrate that the current constitutive model is capable of simulating well a multitude of rate-dependent low cycle fatigue and fatigue-creep responses at high temperatures.

8. Recommendations

8.1 Cyclic softening as a function of fatigue-creep hold-time

At 950°C the cyclic softening response was seen to be a complex function of loading waveform, fatigue or fatigue-creep, as well as strain range. The current UCM cannot predict differing degrees of cyclic softening as a function of the loading waveform. Since the cyclic softening behavior is a critical response it is recommended that this behavior be investigated further and the UCM be further modified to predict these responses.

8.2 Material strength as a function of fatigue-creep hold-time

As discussed in Chapter 2, at strain ranges of 0.3% and 0.4% the strength of alloy 617 is shown to vary significantly as a function of loading wave form. Currently the UCM is not able to simulate both the fatigue and fatigue-creep response reasonably at these strain ranges. It is therefore recommended that this response be studied further.

8.3 Stress overshoot response

The addition of a strain hold, either tensile or compressive, was shown to induce a stress overshoot upon reversal loading immediately after a peak strain hold [5] As can be seen in Chapter 2, at the lower strain range of 0.3% this response greatly affects the hysteresis response. As such it is recommended that this phenomenon be studied further so that the UCM can be modified to simulate this response.

8.4 *Rapid initial softening / improved monotonic predictions*

In general, the monotonic material response will have a significantly different yield strength and plastic modulus in comparison to the cyclic response. Furthermore, as was shown at 950°C, alloy 617 shows initial rapid cyclic softening after the monotonic response. Since both of the above behaviors are significantly different from the cyclic responses at other temperatures it is not possible for the current UCM to simulate both initial monotonic response and the cyclic responses at temperatures with reasonable accuracy. Thus it is recommended that the initial monotonic response and the rapid cyclic softening response at 950^{o}C be further investigated in modifying the UCM towards safe and economic design of the Intermediate Heat Exchanger of the Next Generation Nuclear Power Plants.

9. Acknowledgements

This research is being performed using funding received from the DOE Office of Nuclear Energy's Nuclear Energy University Programs.

10. References

[1] Carroll, L.J., Cabet, C., Madland, R., Wright, R.N. (2011) Creep and Environmental Effect on the High Temperature Creep-Fatigue Behavior of Alloy 617. *J. of ASTM Intl,* Vol. 8, No. 6.

[2] Carroll, L.J., Cabet, C., Wright, R.N. (2010) The Role of Environment on High Temperature Creep-Fatigue Behavior of Alloy 617. *ASME PVP Conf. 2010*, PVP2010-26126

[3] Carroll M.C., Carroll, L.J. (2013) Developing Dislocation Subgrain Structures and Cyclic Softening During High-Temperature Creep-Fatigue of a Nickel Alloy. *Metallurgical and Materials Transactions A,* Vol. 44A, pp. 3592-3607

[4] Wright, J.K., Carroll, L.J., Simpson, J.A., Wright, R.N. (2013) Low Cycle Fatigue of Alloy 617 at 850°C and 950°C. *J. of Engineering Materials and Technology,* Vol. 135.

[5] Chaboche J.L. (1989) Constitutive Equations for Cyclic Plasticity and Cyclic Viscoplasticity. *Int'l Journal of Plasticity,* Vol. 5, pp. 247-302.

[6] Armstrong, P.J., Frederick, C.O., (1966). A Mathematical Representation of the Multiaxial Bauschinger Effect. *Report RD/B/N731, CEGB, Central Electricity Generating Board*, *Berkeley, UK*

[7] Chaboche J.L. (1977) Viscoplastic Constitutive Equations for the Description of Cyclic and Anisotropic Behavior of Metals. *Bulletin de L'Académie Polonaise des Sciences, Série des Science Tecnique*, Vol. XXV, No. 1.

[8] Chaboche, J. L., Dang Van, K. and Cordier, G., (1979). Modelization of the strain memory effect on the cyclic hardening of 316 stainless steel. *ONERA, TP no. 1979-109, L 11/3.*

[9] Bari, S., Hassan, T., (2002). An Advancement in Cyclic Plasticity Modeling for Multiaxial Ratcheting Simulation. *Int. J. Plast. 18* (7), 873–894.

[10] Chaboche, J.L., (2008). A Review of Some Plasticity and Viscoplasticity Constitutive Theories. *Int. J. Plasticity 24*, 1642–1693.

[11] Nouailhas, D., Cailletaud, G., Policella, H., Marquis, D., Dufaily, J., Lieurade, H.P., Ribes, A., Bollinger, E., 1985. On the description of cyclic hardening and initial cold working. Eng. Fract. Mech. 21, 887–895.

[12] Krishna, S., Hassan, T., Ben Naceur, I., Saï, K., Cailletaud, G., (2009). Macro versus micro-scale constitutive models in simulating proportional and nonproportional cyclic and ratcheting responses of stainless steel 304. *Int. J. Plast. 25*, 1910–1949.

[13] Kullig, E., & Wippler, S. (2006). Numerical integration and FEM-implementation of a viscoplastic Chaboche-model with static recovery. *Computational Mechanics*, *38*(6), 491-503.

[14] Ahmed R. (2013) Constitutive Modeling for Very High Temperature Thermo-Mechanical Fatigue Responses. PhD Dissertation, North Carolina State University, Raleigh, N.C.

[15] Bari, S., Hassan, T., (2000). Anatomy of coupled constitutive models for ratcheting simulation. *International Journal of Plasticity, 16*, 381–409.

[16] Rao, K.B.S, Schiffers, H., Schuster, H., and Nickel, H. (1988) Influence of Time and Temperature Dependent Processes on Strain Controlled Low Cycle Fatigue Behavior of Alloy 617. *Metallurgical Transactions A*, 19A, pp. 359-371.

[17] Rahman, S.M. (2006) Finite Element Analysis and Related Numerical Schemes for Ratcheting Simulations. Phd Dissertation, North Carolina State University, Raleigh, N.C.

Appendix

A.1 – *Definition of Stiffness Matrix*

The constitutive model code was developed based upon the use of the vectorized forms of the stress and strain tensors. Thus the generalized Hooke's Law is expressed as shown in Eqn. A1-1. Isotropic behavior was assumed yielding a stiffness matrix that can be expressed in terms of the bulk and shear moduli as shown in Eqn. A1-2.

$$\underline{\sigma} = \underline{\underline{E}}\,\underline{\varepsilon}^{e}\text{, where } \underline{\sigma} = \begin{bmatrix} \sigma_{11} \\ \sigma_{22} \\ \sigma_{33} \\ \sigma_{12} \\ \sigma_{13} \\ \sigma_{23} \end{bmatrix} \text{ and } \underline{\varepsilon}^{e} = \begin{bmatrix} \varepsilon^{e}_{11} \\ \varepsilon^{e}_{22} \\ \varepsilon^{e}_{33} \\ \varepsilon^{e}_{12} \\ \varepsilon^{e}_{13} \\ \varepsilon^{e}_{23} \end{bmatrix} \quad \text{..... (A1-1)}$$

$$\underline{\underline{E}} = \begin{bmatrix} K+\frac{4G}{3} & K-\frac{2G}{3} & K-\frac{2G}{3} & 0 & 0 & 0 \\ K-\frac{2G}{3} & K+\frac{4G}{3} & K-\frac{2G}{3} & 0 & 0 & 0 \\ K-\frac{2G}{3} & K-\frac{2G}{3} & K+\frac{4G}{3} & 0 & 0 & 0 \\ 0 & 0 & 0 & 2G & 0 & 0 \\ 0 & 0 & 0 & 0 & 2G & 0 \\ 0 & 0 & 0 & 0 & 0 & 2G \end{bmatrix} \quad \text{..... (A1-2)}$$

A.2 – *Simplification of* $\underline{\underline{E}}\,\underline{\varepsilon}^{p}$ *to* $2G\underline{\varepsilon}^{p}$

Starting with Eqns. A1-1 and A1-2, one can see by inspection that the torsional strains are already proportional to 2G and that they are independent from the normal strains

thus they can be excluded from this derivation. Eliminating the torsional strain and expanding Eqn. A1-1 yields three linear equations, Eqns. A2-1a-c. Next two assumptions must be made: First, that there is no volume change due to plastic strain and second, that strains are sufficiently small. These two assumptions yield Eqn. A2-2. Rearranging equation A2-1 yields equation A2-3. Rearranging equation A2-2 yields equation A2-4. Combining equations A2-3 and A2-4 yields A2-5. Finally, simplifying equations A2-5 yields Eqn. A2-6. This process can be repeated in a similar fashion for equations A2-1b and A2-1c resulting in the diagonal of the stiffness matrix being composed solely by 2G or what is identical, $2G\boldsymbol{\varepsilon}^p$, validating the initial proposition.

$$\sigma_{11} = \left(K + \frac{4G}{3}\right)\varepsilon_{11}^p + \left(K - \frac{2G}{3}\right)\varepsilon_{22}^p + \left(K - \frac{2G}{3}\right)\varepsilon_{33}^p \quad \text{..... (A2-1a)}$$

$$\sigma_{22} = \left(K - \frac{2G}{3}\right)\varepsilon_{11}^p + \left(K + \frac{4G}{3}\right)\varepsilon_{22}^p + \left(K - \frac{2G}{3}\right)\varepsilon_{33}^p \quad \text{..... (A2-1b)}$$

$$\sigma_{33} = \left(K - \frac{2G}{3}\right)\varepsilon_{11}^p + \left(K - \frac{2G}{3}\right)\varepsilon_{22}^p + \left(K + \frac{4G}{3}\right)\varepsilon_{33}^p \quad \text{..... (A2-1c)}$$

$$\varepsilon_{11}^p + \varepsilon_{22}^p + \varepsilon_{33}^p = 0 \quad \text{..... (A2-2)}$$

$$\sigma_{11} = \left(K + \frac{4G}{3}\right)\varepsilon_{11}^p + \left(K - \frac{2G}{3}\right)\left(\varepsilon_{22}^p + \varepsilon_{33}^p\right) \quad \text{..... (A2-3)}$$

$$\varepsilon_{22}^p + \varepsilon_{33}^p = -\varepsilon_{11}^p \quad \text{..... (A2-4)}$$

$$\sigma_{11} = \left(K + \frac{4G}{3}\right)\varepsilon_{11}^p + \left(K - \frac{2G}{3}\right)\left(-\varepsilon_{11}^p\right) \quad \text{..... (A2-5)}$$

$$\sigma_{11} = 2G\varepsilon_{11}^p \quad \text{..... (A2-5)}$$

A.3 – *Evaluation of tensor dot product*

In the course of the derivation one will often find the dot product expressed such as is shown in Eqn. A3-1. However, in reality this expression is based upon the tensor dot product depicted in Eqn. A3-2 and not the vector dot product. When evaluated, the tensor dot product can be expressed in terms of its components as shown in Eqn. A3-3. Therefore, when calculating the expression A3-1 it should be determined from Eqn. A3-3.

$$\underline{A} : \underline{B} \quad \text{..... (A3-1)}$$

$$\underline{\underline{A}} : \underline{\underline{B}} = \begin{bmatrix} A_{11} & A_{12} & A_{13} \\ A_{12} & A_{22} & A_{23} \\ A_{13} & A_{23} & A_{33} \end{bmatrix} : \begin{bmatrix} B_{11} & B_{12} & B_{13} \\ B_{12} & B_{22} & B_{23} \\ B_{13} & B_{23} & B_{33} \end{bmatrix} = \sum_{1}^{3}\sum_{1}^{3} A_{ij}B_{ij} \quad \text{..... (A3-2)}$$

$$\underline{\underline{A}} : \underline{\underline{B}} = A_{11}B_{11} + A_{22}B_{22} + A_{33}B_{33} + 2A_{12}B_{12} + 2A_{13}B_{13} + 2A_{23}B_{23} \quad \text{..... (A3-3)}$$

A.4 – *Correction Terms*

The radial return method is a strain driven approach and as such all total strain increments must be defined in order to find the updated stress and plastic strain increments; however, in many loading cases not all of the strain components are known. Therefore, in order to use the radial return method a set of correction terms must be defined such that the total strain increment is known for each loading step [17]. This process will be outlined subsequently.

First one starts with the assumption that the total strain is fully elastic for all strain components and as such follows the three dimensional Hooke's law as shown in Eqn. A4-1. Note that this initially assumed strain increment will be termed the trial strain increment as is defined by Eqn. A4-2; also, the n+1 subscript will be implied henceforth. Remark that the known uniaxial strain increment does not have a trail superscript as it is already known. With the previous two equations defined it is now possible to solve for the as of yet unknown trial strain increments. To begin this process last five equations defined by Eqn. A4-1 are written out explicitly in Eqns. A4-3 – A4-7. Next Eqn. A4-3 and A4-4 are solved for $\Delta\varepsilon_{22}^{tr}$ and $\Delta\varepsilon_{33}^{tr}$ respectively yielding Eqns. A4-8 and A4-9. Note that in the uniaxial case all of the stress increments not in the uniaxial direction are zero. Therefore, in addition to eliminating $\Delta\sigma_{11}$ and $\Delta\sigma_{22}$ from Eqns. A4-3 and A4-4, it is known that the torsional trial strain increment will be equal to zero ad defined by Eqns. A4-10,11,12. Lastly $\Delta\varepsilon_{22}^{tr}$ and $\Delta\varepsilon_{33}^{tr}$ can be found by solving the simultaneous systems of equations Eqns. A4-8 and A4-9 which leads to Eqn. A4-13.

$$\Delta\underline{\sigma}_{n+1} = \underline{\underline{E}}\Delta\underline{\varepsilon}_{n+1}^{tr} \quad \text{..... (A4-1)}$$

$$\Delta\underline{\varepsilon}^{tr} = \begin{bmatrix} \Delta\varepsilon_{11} & \Delta\varepsilon_{22}^{tr} & \Delta\varepsilon_{33}^{tr} & \Delta\varepsilon_{12}^{tr} & \Delta\varepsilon_{13}^{tr} & \Delta\varepsilon_{23}^{tr} \end{bmatrix}^{T} \quad \text{..... (A4-2)}$$

$$\Delta\sigma_{22} = k_2\left(\Delta\varepsilon_{11} + \Delta\varepsilon_{33}^{tr}\right) + k_1\Delta\varepsilon_{22}^{tr} \quad \text{(A4-3)}$$

$$\Delta\sigma_{33} = k_2\left(\Delta\varepsilon_{11} + \Delta\varepsilon_{22}^{tr}\right) + k_1\Delta\varepsilon_{33}^{tr} \quad \text{(A4-4)}$$

$$\Delta\sigma_{12} = 2G\Delta\varepsilon_{12}^{tr} \quad \text{(A4-5)}$$

$$\Delta\sigma_{13} = 2G\Delta\varepsilon_{13}^{tr} \quad \text{(A4-6)}$$

$$\Delta\sigma_{23} = 2G\Delta\varepsilon_{23}^{tr} \quad \text{(A4-7)}$$

$$\Delta\varepsilon_{22}^{tr} = -\frac{k_2}{k_1}\left(\Delta\varepsilon_{11} + \Delta\varepsilon_{33}^{tr}\right) \quad \text{(A4-8)}$$

$$\Delta\varepsilon_{33}^{tr} = -\frac{k_2}{k_1}\left(\Delta\varepsilon_{11} + \Delta\varepsilon_{22}^{tr}\right) \quad \text{(A4-9)}$$

$$\Delta\varepsilon_{12}^{tr} = 0 \quad \text{(A4-10)}$$

$$\Delta\varepsilon_{13}^{tr} = 0 \quad \text{(A4-11)}$$

$$\Delta\varepsilon_{23}^{tr} = 0 \quad \text{(A4-12)}$$

$$\Delta\varepsilon_{22}^{tr} = \Delta\varepsilon_{33}^{tr} = \frac{-1}{k_1^2 - k_2^2}\left(k_1k_2 - k_2^2\right)\Delta\varepsilon_1 \quad \text{(A4-13)}$$

Now a trial set of total strain increments have been developed such that all strain increments are known. This set of total strain increments is only valid however for elastic increments. Therefore it is now necessary to derive a set of correction terms such that the previously derived strain increments can be used during plastic loading.

Again one begins with the 3-D Hooke's Law as shown in Eqn. A4-14. The n+1 will also henceforth be implied. The trial stain increment previously developed will be incorporated as shown in Eqn. A4-15. With some rearranging Eqn. A4-15 can be rewritten at Eqn. A4-16. Next the terms such as $\Delta\varepsilon_{22}$- $\Delta\varepsilon_{22}^{tr}$ need to be evaluated. This is accomplished by developing a set of equations similar to that of A4-3 through A4-7 except now in accordance with A4-14. This yields Eqns. A4-17 through A4-21. These equations can then be found in terms of total strain as shown in Eqns. A4-22 through A4-26; note that like before all of the stress increments are zero except σ_{11}. The difference between the each unknown total strain increment and the trial stress can now be found, for example, as the difference between A4-22 and A4-8. Taking all five differences yields Eqns. A4-27 through

A4-31. At this point all of the torsional differences are defined as solely a function of the plastic strain increment. However equations A4-27 and A4-28 are still not sole functions of the plastic strain. To accomplish this two simplifying constants are define by Eqns. A4-32 and A4-44. After this, from Eqns. A4-27 and A4-28, the differences between $\Delta\varepsilon_{22}$- $\Delta\varepsilon_{22}^{tr}$ and $\Delta\varepsilon_{33}$- $\Delta\varepsilon_{33}^{tr}$ can be found to be equal to Eqns. A4-34 and A4-35. Now that all the differences found in A4-16 have been defined as a function of the inelastic strain they can be substituted back into Eqn. A4-16 yielding Eqn. A-36. Note that some of the constants used in this expression are defined in subsequent expressions. As is will be required, Eqn. A-36 can be converted into deviatoric space yielding A-37. The definition of the elastic strain, Eqn. 5, can be inserted into Eqns. A-36 and A-37 which after some manipulation yield Eqns. A-44 and A-45 which are the same equations 33 and 34. Finally note that $\underline{x}$ and $\underline{y}$ are defined by Eqns. A-46 and A-47.

$$\Delta\underline{\sigma}_{n+1} = \underline{\underline{E}}\Delta\underline{\varepsilon}_{n+1} - 2G\Delta\underline{\varepsilon}_{n+1}^{in} \quad \text{..... (A4-14)}$$

$$\Delta\underline{\sigma} = \underline{\underline{E}}\Delta\underline{\varepsilon} - 2G\Delta\underline{\varepsilon}^{in} + \underline{\underline{E}}\Delta\underline{\varepsilon}^{tr} - \underline{\underline{E}}\Delta\underline{\varepsilon}^{tr} \quad \text{..... (A4-15)}$$

$$\begin{bmatrix}\Delta\sigma_{11}\\ \Delta\sigma_{22}\\ \Delta\sigma_{33}\\ \Delta\sigma_{12}\\ \Delta\sigma_{13}\\ \Delta\sigma_{23}\end{bmatrix} = \underline{\underline{E}}\begin{bmatrix}\Delta\varepsilon_{11}\\ \Delta\varepsilon_{22}^{tr}\\ \Delta\varepsilon_{33}^{tr}\\ \Delta\varepsilon_{12}^{tr}\\ \Delta\varepsilon_{13}^{tr}\\ \Delta\varepsilon_{23}^{tr}\end{bmatrix} - 2G\Delta\underline{\varepsilon}_{n+1}^{in} + \begin{bmatrix}k_2\\ k_1\\ k_2\\ 0\\ 0\\ 0\end{bmatrix}\left(\Delta\varepsilon_{22} - \Delta\varepsilon_{22}^{tr}\right) + \begin{bmatrix}k_2\\ k_2\\ k_1\\ 0\\ 0\\ 0\end{bmatrix}\left(\Delta\varepsilon_{33} - \Delta\varepsilon_{33}^{tr}\right)$$
$$+2G\begin{bmatrix}0\\ 0\\ 0\\ 1\\ 0\\ 0\end{bmatrix}\left(\Delta\varepsilon_{12} - \Delta\varepsilon_{12}^{tr}\right) + 2G\begin{bmatrix}0\\ 0\\ 0\\ 0\\ 1\\ 0\end{bmatrix}\left(\Delta\varepsilon_{13} - \Delta\varepsilon_{13}^{tr}\right) + 2G\begin{bmatrix}0\\ 0\\ 0\\ 0\\ 0\\ 1\end{bmatrix}\left(\Delta\varepsilon_{23} - \Delta\varepsilon_{23}^{tr}\right) \quad \text{.. (A4-16)}$$

$$\Delta\sigma_{22} = k_2\Delta\varepsilon_{11} + k_1\Delta\varepsilon_{22} + k_2\Delta\varepsilon_{33} - 2G\Delta\varepsilon_{22}^{in} \quad \text{..... (A4-17)}$$

$$\Delta\sigma_{33} = k_2\Delta\varepsilon_{11} + k_2\Delta\varepsilon_{22} + k_1\Delta\varepsilon_{33} - 2G\Delta\varepsilon_{33}^{in} \quad \text{..... (A4-18)}$$

$$\Delta\sigma_{12} = 2G\Delta\varepsilon_{12} - 2G\Delta\varepsilon_{12}^{in} \quad \text{..... (A4-19)}$$

$$\Delta\sigma_{13} = 2G\Delta\varepsilon_{13} - 2G\Delta\varepsilon_{13}^{in} \quad \text{..... (A4-20)}$$

$$\Delta\sigma_{23} = 2G\Delta\varepsilon_{23} - 2G\Delta\varepsilon_{23}^{in} \quad \text{..... (A4-21)}$$

$$\Delta\varepsilon_{22} = -\frac{k_2}{k_1}\left(\Delta\varepsilon_{11} + \Delta\varepsilon_{33}\right) + \frac{2G}{k_1}\Delta\varepsilon_{22}^{in} \quad \text{..... (A4-22)}$$

$$\Delta\varepsilon_{33} = -\frac{k_2}{k_1}\left(\Delta\varepsilon_{11} + \Delta\varepsilon_{22}\right) + \frac{2G}{k_1}\Delta\varepsilon_{33}^{in} \quad \text{..... (A4-23)}$$

$$\Delta\varepsilon_{12} = \Delta\varepsilon_{12}^{in} \quad \text{..... (A4-24)}$$

$$\Delta\varepsilon_{13} = \Delta\varepsilon_{13}^{in} \quad \text{..... (A4-25)}$$

$$\Delta\varepsilon_{23} = \Delta\varepsilon_{23}^{in} \quad \text{..... (A4-26)}$$

$$\Delta\varepsilon_{22} - \Delta\varepsilon_{22}^{tr} = -\frac{k_2}{k_1}\left(\Delta\varepsilon_{33} - \Delta\varepsilon_{33}^{tr}\right) + \frac{2G}{k_1}\Delta\varepsilon_{22}^{in} \quad \text{..... (A4-27)}$$

$$\Delta\varepsilon_{33} - \Delta\varepsilon_{33}^{tr} = -\frac{k_2}{k_1}\left(\Delta\varepsilon_{22} - \Delta\varepsilon_{22}^{tr}\right) + \frac{2G}{k_1}\Delta\varepsilon_{33}^{in} \quad \text{..... (A4-28)}$$

$$\Delta\varepsilon_{12} - \Delta\varepsilon_{12}^{tr} = \Delta\varepsilon_{12}^{in} \quad \text{..... (A-29)}$$

$$\Delta\varepsilon_{13} - \Delta\varepsilon_{13}^{tr} = \Delta\varepsilon_{13}^{in} \quad \text{..... (A-30)}$$

$$\Delta\varepsilon_{23} - \Delta\varepsilon_{23}^{tr} = \Delta\varepsilon_{23}^{in} \quad \text{..... (A-31)}$$

$$C_1 = \frac{k_2}{k_1} \quad \text{..... (A4-32)}$$

$$C_2 = \frac{2G}{k_1} \quad \text{..... (A4-33)}$$

$$\Delta\varepsilon_{22} - \Delta\varepsilon_{22}^{tr} = \frac{C_2}{1 - C_1^2}\left(\Delta\varepsilon_{22}^{in} - C_1\Delta\varepsilon_{33}^{in}\right) \quad \text{..... (A-34)}$$

$$\Delta\varepsilon_{33} - \Delta\varepsilon_{33}^{tr} = \frac{C_2}{1 - C_1^2}\left(\Delta\varepsilon_{33}^{in} - C_1\Delta\varepsilon_{22}^{in}\right) \quad \text{..... (A-35)}$$

$$\begin{aligned}\Delta\underline{\sigma} = \underline{\underline{E}}\Delta\underline{\varepsilon} - 2G\Delta\underline{\varepsilon}^{in} &+ \left(K\underline{1} + \underline{G}_2\right)\frac{C_2}{1 - C_1^2}\left(\Delta\varepsilon_{22}^{in} - C_1\Delta\varepsilon_{33}^{in}\right) \\ &+ \left(K\underline{1} + \underline{G}_3\right)\frac{C_2}{1 - C_1^2}\left(\Delta\varepsilon_{33}^{in} - C_1\Delta\varepsilon_{22}^{in}\right) \\ &+ 2G\underline{I}_4\left(\Delta\varepsilon_{12}^{in}\right) + 2G\underline{I}_5\left(\Delta\varepsilon_{13}^{in}\right) + 2G\underline{I}_6\left(\Delta\varepsilon_{23}^{in}\right)\end{aligned} \quad \text{..... (A-36)}$$

$$\Delta\underline{S} = \underline{\underline{E}}\Delta\underline{\varepsilon} - 2G\Delta\underline{\varepsilon}^{in} + \underline{G}_2\frac{C_2}{1-C_1^2}\left(\Delta\varepsilon_{22}^{in} - C_1\Delta\varepsilon_{33}^{in}\right)$$
$$+ \underline{G}_3\frac{C_2}{1-C_1^2}\left(\Delta\varepsilon_{33}^{in} - C_1\Delta\varepsilon_{22}^{in}\right) \quad \text{..... (A-37)}$$
$$+ 2G\underline{I}_4\left(\Delta\varepsilon_{12}^{in}\right) + 2G\underline{I}_5\left(\Delta\varepsilon_{13}^{in}\right) + 2G\underline{I}_6\left(\Delta\varepsilon_{23}^{in}\right)$$

$$\underline{1} = \begin{bmatrix}1 & 1 & 1 & 0 & 0 & 0\end{bmatrix}^T \quad \text{..... (A-38)}$$

$$\underline{G}_2 = \begin{bmatrix}\frac{-2G}{3} & \frac{4G}{3} & \frac{-2G}{3} & 0 & 0 & 0\end{bmatrix}^T \quad \text{..... (A-39)}$$

$$\underline{G}_3 = \begin{bmatrix}\frac{-2G}{3} & \frac{-2G}{3} & \frac{4G}{3} & 0 & 0 & 0\end{bmatrix}^T \quad \text{..... (A-40)}$$

$$\underline{I}_4 = \begin{bmatrix}0 & 0 & 0 & 1 & 0 & 0\end{bmatrix}^T \quad \text{..... (A-41)}$$

$$\underline{I}_4 = \begin{bmatrix}0 & 0 & 0 & 0 & 1 & 0\end{bmatrix}^T \quad \text{..... (A-42)}$$

$$\underline{I}_4 = \begin{bmatrix}0 & 0 & 0 & 0 & 0 & 1\end{bmatrix}^T \quad \text{..... (A-43)}$$

$$\Delta\underline{\sigma} = \underline{\underline{E}}\Delta\underline{\varepsilon} - 2G\Delta\underline{\varepsilon}^{in} + \Delta p\,\underline{y} \quad \text{..... (A-44)}$$

$$\Delta\underline{S} = \underline{\underline{E}}\Delta\underline{\varepsilon} - 2G\Delta\underline{\varepsilon}^{in} + \Delta p\,\underline{x} \quad \text{..... (A-45)}$$

$$\underline{x} = \frac{3}{2J\left(q_{n+1}\right)}\begin{bmatrix}(K\underline{1} + \underline{G}_2)\frac{C_2}{1-C_1^2}\left(q_{n+1,22} - C_1 q_{n+1,33}\right) \\ +(K\underline{1} + \underline{G}_3)\frac{C_2}{1-C_1^2}\left(q_{n+1,33} - C_1 q_{n+1,22}\right) \\ +2G\underline{I}_4\left(q_{n+1,12}\right) + 2G\underline{I}_5\left(q_{n+1,13}\right) + 2G\underline{I}_6\left(q_{n+1,23}\right)\end{bmatrix} \quad \text{..... (A-46)}$$

$$\underline{y} = \frac{3}{2J\left(q_{n+1}\right)}\begin{bmatrix}\underline{G}_2\frac{C_2}{1-C_1^2}\left(q_{n+1,22} - C_1 q_{n+1,33}\right) \\ \underline{G}_3\frac{C_2}{1-C_1^2}\left(q_{n+1,33} - C_1 q_{n+1,22}\right) \\ +2G\underline{I}_4\left(q_{n+1,12}\right) + 2G\underline{I}_5\left(q_{n+1,13}\right) + 2G\underline{I}_6\left(q_{n+1,23}\right)\end{bmatrix} \quad \text{..... (A-47)}$$

Conference paper given at ASME 2014 Pressure Vessels & Piping Conference (PVP2014) July 20-24, 2014, Anaheim, California, USA

Paper NOT provided in full due to ASME Copyright

The doi for the paper is: http://dx.doi.org/ 10.1115/PVP2014-28789

Paper PVP2014-28789, 8 Pages

Title:

A UNIFIED CONSTITUTIVE MODEL FOR HIGH TEMPERATURE MULTIAXIAL CREEPFATIGUE AND RATCHETING RESPONSE SIMULATION OF ALLOY 617

Authors

Nazrul Islam North Carolina State University Raleigh, NC, USA Email: nislam3@ncsu.edu

Shahriar Quayyum North Carolina State University Raleigh, NC, USA Email: squayyu@ncsu.edu

Tasnim Hassan North Carolina State University Raleigh, NC, USA Email: thassan@ncsu.edu

Abstract

The study is developing a unified constitutive model for Alloy 617 which is the prime candidate material considered for intermediate heat exchanger (IHX) of next generation nuclear power plant. Alloy 617 can experience long term exposure to elevated temperatures as high as 950ºC, however, the ASME design code (Subsection NH) does not include design provisions for this temperature range. In addition, the Draft Alloy 617 Code Case specifies that the inelastic design analysis for temperatures above 649ºC must be based on unified constitutive model. Therefore, this study focuses on developing a unified constitutive model to simulate high temperature uniaxial and multiaxial creep-fatigue and creep-ratcheting responses of Alloy 617. As multiaxial response simulation is a key factor for designby-analysis of IHX, a set of biaxial tests with varying degrees of loading non-proportionality has been performed at different steady temperatures within 25ºC-950ºC, and with different strain rates and strain ranges. From the tests, it has been observed that temperature, strain rate, strain ranges and non-proportionality of loading path greatly influences the creep-fatigue and creep-ratcheting responses of Alloy 617. Thus, development of a unified constitutive model considering dependence of these parameters is required. The current Chaboche viscoplasticity model with static recovery term can simulate uniaxial responses very well but it overpredicts biaxial ratcheting responses. Hence, a modified Chaboche model has been developed to improve biaxial ratcheting simulations. Multiaxial modeling features of non-proportionality and ratcheting are investigated. These modeling features and improved response simulations are presented in the paper.